Modélisation des états dynamiques de vortex dans des ondes de densité de charge

Tianyou Yi

▶ **To cite this version:**

Tianyou Yi. Modélisation des états dynamiques de vortex dans des ondes de densité de charge. Autre [cond-mat.other]. Université Paris Sud - Paris XI, 2012. Français. NNT : 2012PA112200 . tel-00768237

HAL Id: tel-00768237

https://theses.hal.science/tel-00768237

Submitted on 21 Dec 2012

HAL is a multi-disciplinary open access archive for the deposit and dissemination of scientific research documents, whether they are published or not. The documents may come from teaching and research institutions in France or abroad, or from public or private research centers.

L'archive ouverte pluridisciplinaire **HAL**, est destinée au dépôt et à la diffusion de documents scientifiques de niveau recherche, publiés ou non, émanant des établissements d'enseignement et de recherche français ou étrangers, des laboratoires publics ou privés.

THÈSE de DOCTORAT de l'UNIVERSITÉ PARIS-SUD XI

ÉCOLE DOCTORALE: Physique de la région parisienne
Laboratoire de Physique Théorie et Modèle Statistique

DISCIPLINE : Physics

by

Tianyou YI

Modeling of dynamical vortex states in charge density waves

September 2012

Composition of the jury:

Serguei Brazovskii	Directeur de thèse
Alexandre Bouzdine	Rapporteur
Denis Feinberg	Rapporteur
Michel Héritier	Examinateur
Pierre Monceau	Examinateur
Nicolas Pavloff	Examinateur

Orsay France

Acknowledgments

I would like to thank Serguei Brazovskii, who gives me an opportunity to do my thesis. As an incompetent PhD student, I got the chance to have a brilliant supervisor. He gave me untiring support and intelligent guidance of my theses.

I would like to thank Natasha Kirova. I thank her for giving me many useful advices during the preparation of my thesis, and also for her collaborative work during my thesis.

I would like to thank Alvaro Rojo Bravo, who gave me much help when I began my PhD work.

I would like to thank all the members of Laboratory of Theoretical Physics and Statistical Models. I will never forget the marvelous human relations and the great atmosphere that surrounded during my stay in the laboratory.

My gratitude also goes toward my parents and my sister for their moral support during my thesis. Their constant encouragement and great understanding gave me the strength to withstand and finally to accomplish this work.

Abstract

Formation of charge density waves (CDW) is a symmetry breaking phenomenon found in electronic systems, which is particularly common in quasi-one-dimensional conductors. It is widely observed from highly anisotropic materials to isotropic ones like the superconducting pnictides. The CDW is seen as a sinusoidal deformation of coupled electronic density and lattice modulation; it can be also viewed as a crystal of singlet electronic pairs. In the CDW state, the elementary units can be readjusted by absorbing or rejecting pairs of electrons. Such a process should go via topologically nontrivial configurations: solitons and dislocations - the CDW vortices. An experimental access to these inhomogeneous CDW states came from studies of nano-fabricated mesa-junctions, from the STM and from the X-ray micro-diffraction.

Following these requests, we have performed a program of modeling stationary states and of their transient dynamic for the CDW in restricted geometries under applied voltage or at passing normal currents. The models takes into account multiple fields in mutual nonlinear interactions: the two components of the CDW complex order parameter $A\exp(i\varphi)$, and distributions of the electric field, the density and the current of normal carriers. We used the Ginzburg-Landau type approach and also we have derived its extension based on the property of the chiral invariance.

We observed the incremental creation of static dislocations within the junctions. The transient dynamics is very rich showing creation, annihilation and sweeping of multiple vortices. The dislocations cores concentrate the voltage drops thus providing self-tuned microscopic junctions where the tunneling creation of electron-hole pairs can take place.

The results obtained from this model agree with experiment observations. The method can be extended to other types of charge organization known under the general name of the Electronic Crystal. It takes forms of Wigner crystals at hetero-junctions and in nano-wires, CDWs in chain compounds, spin density waves in organic conductors, and stripes in doped oxides. The studied reconstruction in junctions of the CDW may be relevant also to modern efforts of the field-effect transformations in strongly correlated materials with a spontaneous symmetry breaking.

Résumé

La formation des ondes de densité de charge (ODC) est un phénomène de brisure de symétrie qui apparaît dans systèmes électroniques, et particulièrement dans les conducteurs quasi-unidimensionnels. Elle est observée aussi bien dans les matériaux très anisotropes que les isotropes comme par exemple les supraconducteurs pnictures. L'ODC peut être vue comme une déformation sinusoïdale de la densité électronique et de la modulation du réseau, ou également comme un cristal de singulets électroniques. Dans un état d'ODC, les cellules élémentaires peuvent être modifiées en absorbant ou en rejetant des paires d'électrons. Un tel processus passe par des configurations topologiquement non triviales: des solitons et des dislocations, ou plus généralement des vortex d'ODC. Ces états inhomogènes peuvent être obtenus expérimentalement dans des nano-produits appelés "mésa-jonctions", et observés à l'aide d'un microscope à effet tunnel ou d'une radiographie par microdiffraction.

Afin de simuler ces expériences, nous avons réalisé un programme modélisant les états stationnaires d'ODC ainsi que leur dynamique transitoire à travers des géométries restreintes auxquelles sont appliquées une tension ou un courant. Le modèle prend en compte plusieurs champs en interaction non linéaire: le paramètre d'ordre complexe d'ODC, la distribution de champ électrique, ainsi que la densité et le courant des autres porteurs de charge. Nous avons utilisé une approche de type Ginzburg-Landau ainsi qu'une extension basée sur une propriété d'invariance chirale.

A l'aide de ce programme, nous avons observé la création progressive de dislocations statiques dans les jonctions. La dynamique transitoire est alors très riche avec notamment des créations, des annihilations et des balayages de vortex multiples. Des chutes de tension apparaissent au centre des dislocations, créant ainsi des jonctions tunnel microscopiques à travers lesquelles transitent des paires électron-trou.

Les résultats qualitatifs obtenus sont en très bon accord avec les observations expérimentales. Ce model peut aussi être étendu à tout type de cristaux électronique comme les cristaux de Wigner dans les hétéro-jonctions et les nano-fils, les ODC dans les composés de chaîne, les ondes de densité de spin dans les conducteurs organiques, ou encore les structures de bandes

dans les oxydes dopés. La reconstruction des ODC dans les jonctions tunnel peut aussi trouver son importance dans l'étude des effets de champs sur les matériaux fortement corrélés induisant des brisures spontanées de symétries.

Contents

List of Figures

List of symbols

Symbol	Description
$\Psi = A\exp(i\varphi)$	CDW complex order parameter
A	CDW complex order parameter amplitude
φ	CDW complex order parameter phase
λ	CDW wave number
Δ	Half-gap in CDW
n_c	CDW charge density
n_{in}	Intrinsic carrier density
n_{ex}	Extrinsic carrier density
ρ_c	Dimensionless condensate carrier density
ρ_n	Dimensionless normal carrier density
N_i	Density of states of intrinsic carriers at Fermi level
v_F	Fermi velocity
ε_F	Fermi energy
r_0	Debye screening length
ξ or ξ_x	Coherence length along chain axis
$\xi_\perp$	Coherence length perpendicular to chain axis
ϵ	Dielectric response
γ_φ	Damping coefficient for the phase φ
s	Area per chain
σ_{CDW}	CDW conductivity
$\hat{\sigma} = (\sigma_x, \sigma_y)$	Anisotropy normal conductivity
β	CDW anisotropy parameter
T	Elastic stress
Φ	Electric potential
e	The charge of an electron $e > 0$

Symbol	Description
$f_{x,y}$	Partial differentiation with respect to x or y of function f
f_t	Partial differentiation with respect to time t of function f
$\hat{\nabla} = \partial_x + \beta^2 \partial_y$	Anisotropy gradient

Chapter 1

Introduction

Studies of electronic crystals is a very active subject in condensed matter physics [1, 2]. These physical systems distinguish themselves by spontaneous phase transitions, at low temperature, to states where the electrons form a well-organized superstructures. These fascinating states give a way to understand the quantum properties, which show up directly already at macroscopic scale. The electronic crystals is a common organization in conducting solids. They take forms of Wigner crystals at hetero-junctions and nano-wires, charge density waves (CDWs) in chain compounds, spin density waves (SDWs) in organic conductors, stripes in doped oxides and high-Tc superconductors. Sister systems are the charged colloidal crystals and vortex lattices in type II superconductors. A unique property of electronic crystals is related to the possibility of the collective current conduction by sliding. This property is ultimately related to appearance of inhomogeneous superstructures under stresses.

CDW is a particular kind of electronic crystal: most accessible experimentally and best treatable theoretically. It is a crystal of singlet electronic pairs, which is typically formed in quasi one-dimensional conductors.

In the CDW ground state, the elementary units can be readjusted by absorbing or rejecting pairs of electron. Such a process should go via topologically nontrivial configurations: solitons and dislocations - the CDW vortices. The CDW can be strained by applied voltage or by charge transfer at junctions, or by an electric field which can also put the CDW into sliding.

Such strains can give rise to local or long range modulational instabilities. An experimental access to those states came from studies of nano-fabricated mesa-junctions, from the scanning tunneling microscopy (STM) and from the coherent X-ray micro-diffraction. These experiments raise fundamental questions related to ground state in these systems.

The thesis is devoted to studying of CDWs in junctions and at a restrained geometry and to elucidating the role of dislocations in the local reconstruction of the electronic ground state. The dynamics of these topological defects should play an important role in the sliding process of the CDW. The theoretical models have been proposed or derived, and the numerical modeling for various cases was performed. The essence of the work was a numeric dynamical modeling of strongly nonlinear, nonstationary multi-component system embracing the order parameter, the electric field and various normal carriers.

Conceptually, and sometimes even in details, the theoretical results are in a good agreement with experiments on the interlayer tunnelling in quasi one-dimensional compounds with CDWs.

The thesis is organized as follows.

In chapter 2, we recall the base notion and general characteristics of CDWs, which will be necessary in the following chapters. The chapter begins with description of the Peierls instability, which explains the origin of the CDW formation in the quasi-one-dimensional system. It introduces main ideas related to the stationary states and to the dynamics of CDW system, such as fluctuations in 1D, Fröhlich conduction, phason, the CDW charge density, the CDW current, pinning mechanism and types of normal carriers.

In chapter 3, we discuss the existing theories and experimental observations of the dislocations in CDW. We briefly introduce the reasons for the vortex creation in CDW, which we develop in the later chapters.

In chapter 4, we describe the tunneling experiment in CDW, which gives motivations for our modeling. We also give necessary details on CDW dislocations.

In chapter 5, we describe studies of the CDW ground state by the energy minimization method and the minimal Ginzburg-Landau model. CDW vortices appear in both of these methods. The first one gives only the static

results, while the second one reveals the static and dynamic features of the system. These results have given some hints for the experimental observations, and provide a firm base for the theory in chapter 6.

In chapter 6, we present the most detailed studies of the CDW in a restricted geometry within the Ginzburg-Landau approach. The simplified rectangle geometry is under study at first, followed by the exploration of the restricted geometry in actual experiments. We discuss the results and present a comparison between the vortex state of the CDW and that of the type II superconductor. Calculations of some parameters are given at the end.

In chapter 7, we derive an extended Ginzburg-Landau theory, which takes into account the direct interaction between the "intrinsic electrons" and the CDW deformations. The resulting equations are non-analytical in the order parameter, unlike in the previous the Ginzburg-Landau approach. That makes the numerical calculations much more challenging, facing unavoidable instabilities. The results are less detailed, but all show the nucleation of vortices at surface boundaries. A new phenomenon is a suppression of the CDW state provided by normal currents.

In chapter 8, we derive general equations to take into account the conversion - exchange of electrons - between the collective and the normal reservoirs. We obtained limited results for the 1D system, for the rectangular and the actual geometries. One new effect is the canalization of the normal current and its ability to destroy the CDW when hitting the obstacle.

Chapter 9 is devoted to conclusion and perspective.

Details on numeric implementations and on computing are given in the Appendix A.

Chapter 2

Charge density waves - general concepts

In this chapter, we describe principal concepts and theories concerning the charge density waves, which are relevant to the work presented in the thesis. Details can be found in several books, review articles and conference proceedings (see e.g. [3, 4, 5, 6, 7, 8]). After a short historical summary, we present the theories of the Peierls transition, followed by the Fröhlich conductivity, then collective excitations for the CDW system, and finally the principal mechanisms of pinning of the CDW.

2.1 Brief history

Complex studies of quasi-one-dimensional (quasi-1D) systems began and developed in 1970s inspired by the article by W.A. Little [9] in 1964. This article proposed the theoretical arguments that certain quasi-1D conductors could have a superconducting state extending up to the ambient temperature. The starting collaboration between physicists and chemists results in a great progress in the synthesis of several families of quasi-1D materials. While the goal of reaching the high temperature superconductor was not achieved on this way, the work has led to discovery of many phase transitions and the first one was the transition to a CDW phase. This CDW phase shows a great richness of physical properties. Particularly, the nonlinear behavior in

the I-V curves have been observed with some similarities to the vortex phase in type II superconductors. These nonlinear effects were first discovered in 1976 in $NbSe_3$ by P. Monceau et al [10], and then interpreted as a collective sliding state of the charge density waves by J. Bardeen [11, 12, 13] and in [14].

The CDWs show up first of all as the metal-insulator transition at low temperature. By X-rays scattering, this was found to be associated with appearance of the lattice superstructure. But the most spectacular effect is the collective sliding. The CDWs are intensively studied up to nowadays, and experimental results and theories are still in progress.

2.2 Charge density wave materials

CDW materials generally contain weakly coupled atomic chains or molecular stacks along which electrons are strongly delocalized. There exist organic and inorganic CDW materials. 1D organic conductors usually are formed by stacks of flat organic molecules with the highest conductivity along the stacks (conducting "chains"). These stacks may be separated by columns of ions. The metallic state is due to the overlap of partly filled molecular orbitals. In inorganic compounds, the conduction chains are realized in various ways. The earliest example is the platinum-chain compound KCP ($K_2Pt(CN)_4Br_{0.30} \cdot 3H_2O$), see figure 2.1 (A). In $NbSe_3$, the conduction chains are formed by prisms of Nb atoms joint to Se atoms, see figure 2.1 (B).

Today, the CDW can be beautifully visualized by the STM technique as shown in figures 2.2 and 2.3. There analysis recovered a purely sinusoidal modulation of the charge density as in equation (2.1).

2.3 Peierls instability

It was in 1955 when Peierls predicted a phenomenon giving an origin of what we call now the CDW. He was the first to describe the spontaneous metal-insulator phase transition in 1D system.

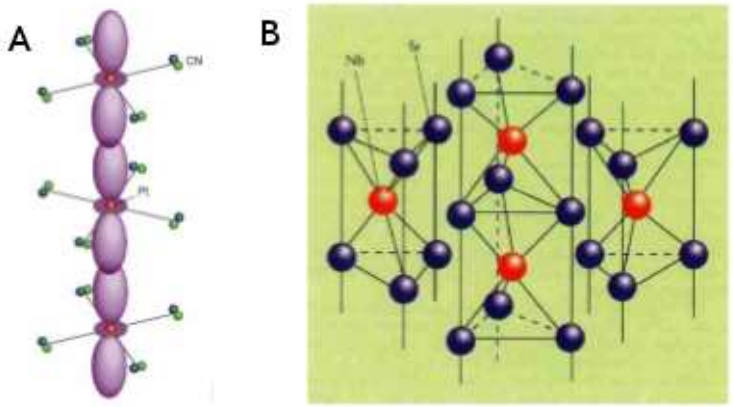

Figure 2.1: The crystal structure of KCP (A) and $NbSe_3$ (B). [15]

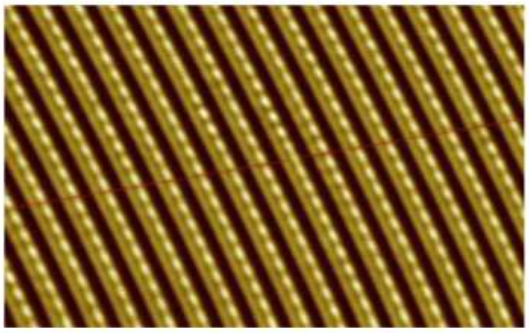

Figure 2.2: Periodic white spots are the CDW maxima. [16]

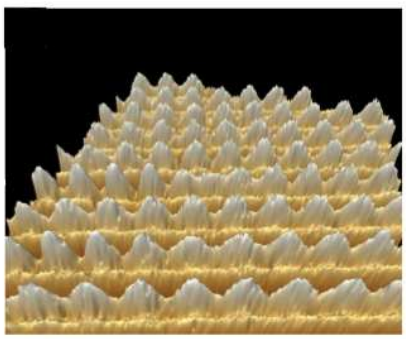

Figure 2.3: STM image of $NbSe_3$, viewed in 3D with perspective, rotated by 90° with respect to figure 2.2. [17]

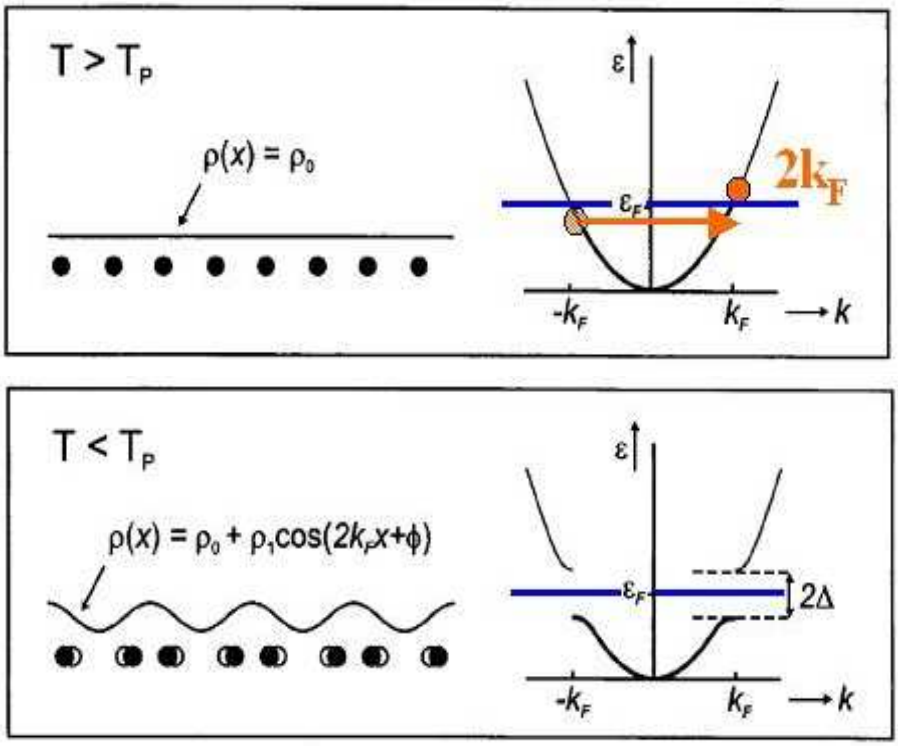

Figure 2.4: Comparison between the metallic state (above) and the CDW state (below) of an deformable conducting filament. Upper panel: the electronic band structure of the metallic chain is described by the 1D free electron dispersion relation $\varepsilon(k) = \hbar^2 k^2/2m$. The total electronic density is uniform and the atoms stay in their equilibrium positions, which are regularly spaced along the chain. Lower panel: in the Peierls state, a gap is open at the Fermi level. The electronic density and the lattice are modulated in space by the period $\lambda = \frac{\pi}{k_F}$ corresponding to the nesting vector $2k_F$ represented by the red arrow in the upper panel. [16]

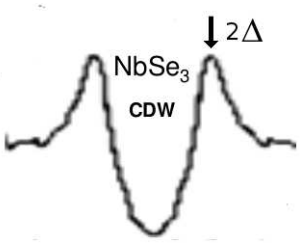

Figure 2.5: A gap of 2Δ is observed in the tunneling spectra of $NbSe_3$ at $T < T_p$. [18]

The idea of Peierls is the following: it is possible to decrease the total energy of the one-dimensional system by opening a gap at Fermi level if we can find a proper coupling with periodic distortions characterized by the wave vector $2k_F$, i.e, with a new period π/k_F. The new position of the n^{th} ion is then: $u_n = na + u_0 \sin(n2k_F a + \varphi)$, where u_0 is the amplitude of the distortion, and φ represents the phase of the modulation. This requires for an additional elastic energy $\sim u_0^2$. The Peierls transition results also in a charge density modulation

$$\rho(x) = \sum_k \Psi_k^*(x)\Psi_k(x) = \rho_0 + \rho_1 \cos(2k_F x + \varphi). \tag{2.1}$$

The deformation opens a gap 2Δ in the electronic spectrum, see figure 2.4. This gap can be observed in the tunneling experiments, as shown e.g. in figure 2.5. The gap 2Δ is proportional to u_0. For a 1D band, the increase of the elastic energy is less than the decrease of the electronic energy (proportional to $u_0^2 \ln(u_0/a)$). In this case any one-dimensional lattice is unstable to a modulation with wave number $2k_F$: this is a metal-insulator transition, usually called Peierls transition.

In general the new structure is incommensurable with the lattice (i.e. the period of the lattice and that of CDW are not in a rational proportion), because the CDW wave number is fixed by the number of electron below the Fermi level. The phase shift in the expression 2.1 corresponds to the rigid displacement of the CDW as whole.

In purely 1D system a true phase transition at a finite temperature is impossible, because of the thermal statistical fluctuations which destroy the or-

der at long distances. In reality, a quai-1D compound has a three-dimensional inter-chain coupling, which comes from transverse overlap of the electronic wave functions (inter-chain tunneling), or from Coulomb interaction between CDW modulations of neighboring chains. Eventually these interactions stabilize the long range order.

2.4 Charge density wave state

Although CDWs appear sometimes in the materials having band structures of bi- or tri- dimension, their formation is essentially 1D phenomena. That is why most of related discussions are based on one-dimensional models.

For 1D systems, electronic correlations effects can cause phase transitions to various collective states at low temperature. Depending on electron-electron and electron-phonon interactions, different ground states can appear, like a singlet or triplet superconductivity, SDWs and CDWs. All these states have been observed in quasi-1D conductors.

For compounds with CDW formation, it is usually sufficient to assume that the normal metallic state can be described by concepts coming from the Fermi liquid theory, such as in terms of the one electron quasi-particles. Still, in presence of interactions between electrons (attractive or repulsive), the Fermi liquid theory collapses and the quasi-particles are undefined even close to Fermi level (see e.g a review [19]). That will give place to non fermionic collective excitations, where spin and charge are separated, and they are described theoretically by the concept of Tomonaga-Luttinger (TL) liquid. In reality, for all of known quasi-1D inorganic materials, the experimental results for the metallic state do not show in favor for the TL liquid behavior. That seems to justify the description of these physical systems in terms of the Fermi liquid and of quasi-particles. But for known 1D organic compounds, there exist certain experimental indications in favor of the TL liquid kind behavior, attributed to the presence of the strong repulsive electronic interactions [20].

For inorganic compounds like the blue bronze or $NbSe_3$, in which we are interested in here, the properties of their normal state can in general be described by a fluctuating model [14] coming from an electron-phonon weak coupling theory, in the framework of the familiar Fermi liquid concept.

However, some features of $NbSe_3$, and also the results of photo-emission and of optical reflectivity on the blue bronze, suggested that the metallic state of these compounds is better described by a theory of a strong electron-phonon coupling (see [21]).

In the framework of the weak electron-phonon coupling theory, the principal characteristics of the Peierls state can be described by the mean field treatment of a 1D electron-phonon Hamiltonian H, named Fröhlich Hamiltonian. We introduce explicitly the modulation of the crystalline lattice by the vector $2k_F$, and we neglect the electron-electron interactions:

$$H = \sum_{k,\sigma} \varepsilon_k c^+_{k,\sigma} c_{k,\sigma} + \sum_q \hbar\omega_q b^+_q b_q + \sum_{k,q,\sigma} g(k) c^+_{k+q,\sigma} c_{k,\sigma} (b^+_{-q} + b_q), \qquad (2.2)$$

Here $c^+_{k,\sigma}(c_{k,\sigma})$ are the creation (annihilation) operators for the electrons in the states of vector k and a spin σ and $b^+_q(b_q)$ are the creation (annihilation) operators for the phonon with momentum q. ε_k and ω_q are the dispersion relations of electrons and phonon, and $g(k)$ is the electron-phonon coupling constant.

We define a complex order parameter,

$$\Delta e^{i\varphi} = g(2k_F) < b^+_{-2k_F} + b_{2k_F} > \qquad (2.3)$$

where $< ... >$ means the mean value of the operators in the ground state. The order parameter takes into account explicitly the fact that in the CDW state, a macroscopic number of phonons with wave numbers $\pm 2k_F$ are occupied. This comes from neglecting the fluctuations in the mean field approximation (however, these later ones are not macroscopically occupied). In fact, the lattice displacement field can be written as:

$$u(x) = \sum_q \frac{1}{\sqrt{2\omega_q}} \left(b^+_{-q} + b_q\right) e^{-iqx}, \qquad (2.4)$$

we see that precisely in the ground state we have introduced a static modulation of vector $2k_F$ for the lattice:

$$< u(x) >= \sqrt{\frac{2}{\omega_{2k_F}}} \frac{\Delta}{g(2k_F)} \cos(2k_F x + \varphi). \qquad (2.5)$$

We can diagonalize the electronic part of the Fröhlich Hamiltonian (2.2), taking the average over the ground state of the phonon states and using the linearized dispersion relation, when ε_k is close to ε_F:

$$\varepsilon_k = v_F(|k| - k_F). \tag{2.6}$$

The thermodynamic properties of the CDW state are similar to that of the superconductor state. In particular we have the BCS expression at $T = 0$

$$\Delta \sim De^{-\frac{1}{\lambda}}, \tag{2.7}$$

where λ is the dimensionless electron-phonon constant, $\lambda = g^2_{2k_F}/(\omega_{2k_F}\varepsilon_F)$. The dependence of $\Delta(T)$ has the characteristic BCS form, which goes to zero at temperature T_p such that

$$\Delta(T = 0) = 1.76 k_B T_p, \tag{2.8}$$

as it is shown in Figure 2.6.

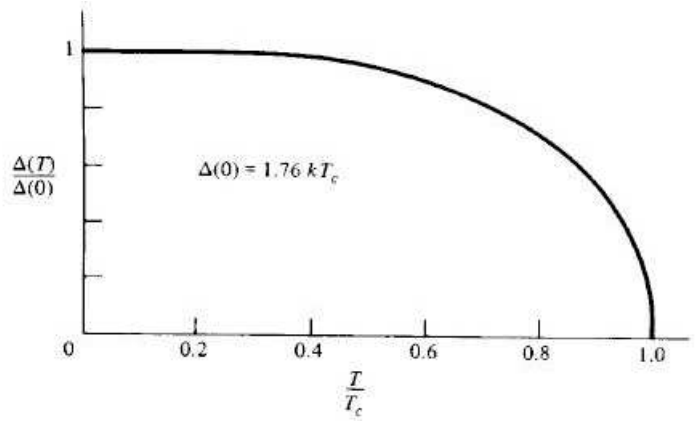

Figure 2.6: A plot of the CDW gap 2Δ as a function of the temperature in the mean field approximation. [5]

Notice that for a superconductor, D is of the order of $\omega_{ph} \ll \varepsilon_F$, hence the transition temperatures T_p are much higher in CDW than those in superconductor. The carriers density in the CDW condensate is also related to $\Delta(T)$, and near T_p we have [5]:

$$\frac{n_c(T)}{n_c(T = 0)} = \frac{\pi\Delta(T)}{4k_B T_p}, \tag{2.9}$$

When $T = 0$, n_c is equal to the number of electrons in the metallic state. The electronic density is then spatially modulated, and we obtain the result of 2.1.

CDWs are similar with superconductors in appearance of the gap in the single particle spectra. However CDWs distinguish from the later by definition of the complex order parameter, which is formed by the pairs of electron-hole located at the two different parts of the Fermi surface, involving then the wave vector $2k_F$.

In 1D at $T = 0$, the normal state is unstable no matter how small is the electron-phonon coupling constant λ. This is a consequence of the logarithmic divergence of the electronic response function to a perturbation by an electronic potential with the wave vector q and with the temporal frequency ω. This response function characterizes the polarization of electrons (Lindhard function),

$$F(q,\omega) = \sum_k \frac{f_{k+q} - fk}{\varepsilon_k - \varepsilon_{k+q} + \hbar\omega} \tag{2.10}$$

$$F(q,0) \sim \frac{1}{\pi v_F}\frac{2k_F}{q}\ln\left|\frac{1+q/2k_F}{1-q/2k_F}\right| \qquad at\,1D, \tag{2.11}$$

where f is the Fermi-Dirac distribution function. The dependence of the susceptibility (2.10) at different dimensions is shown in the figure 2.7. (There will be a power law divergence in case of the TL regime.)

2.5 One-dimensional fluctuations

The mean field approach presented above neglects the important role of the statistic and thermal fluctuations existing in 1D. However, for the quasi-1D compounds it is expected that for small interchain interactions more pronounced 1D properties are shown, such as the development of a CDW. On an other hand, a CDW with long-range order requires 3D interactions. The compromise between being 1D and correlated at the same time in 3D results in CDW transitions occurring at temperature T_{3D} well below the transition temperature T_{MF} calculated from the mean field theory. In the temperature region between T_{3D} and T_{MF}, 1D CDW fluctuations are present. In this

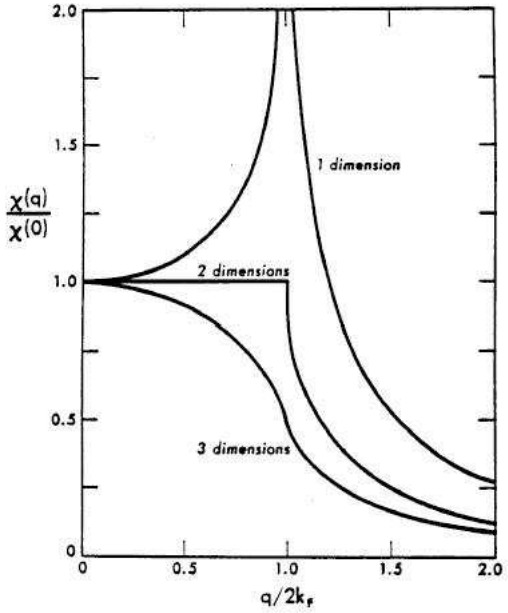

Figure 2.7: Susceptibility of free electron gas in one, two, and three dimensions.

temperature interval a pseudo-gap in the density of states at the Fermi level is observed experimentally. The origin of the pseudo-gap is traditionally attributed to these 1D CDW fluctuations. Evidences also come from X-ray diffraction [22], which shows planes of diffuse scattering oriented perpendicular to the 1D chains at positions $(0, 0, \pm k_F)$ off the main Bragg reflections. The width of these planes usually increases with increasing temperature, indicating a temperature-dependent finite correlation length of the fluctuations along the chains. On approaching T_{3D} from above, a crossover between a 1D and 3D fluctuating regimes is usually found, which transforms into 3D long-range order at T_{3D}.

2.6 Dynamic of the collective mode

2.6.1 Fröhlich superconductivity

In the strong coupling regime, Peierls transition can be considered as a Bose condensation of electron-hole pairs, like a Copper pair formation of elec-

trons in superconductors. But the conduction properties of CDW materials are different from those of superconductors. Three years before the BCS [23] theory, which gave the microscopic mechanism for the superconductivity theory, H.Fröhlich [24] showed in 1954 that despite the gap opening at the Fermi level, there exists a way to build the current carrying state in a 1D system without any activation, and seemingly without energy dissipation. This can be explained in the following way: if the CDW is incommensurate, all its positions with respect to the lattice are energetically equivalent. In a perfect crystal, an infinitesimal electric field would displace the CDW as a whole. The CDW position in space is given directly by its phase, and the time variation of the phase $\dot{\varphi} = v$ puts the CDW in motion. At first sight, it is equivalent to periodical variation of the displacements and the electronic density of the CDW:

$$\Delta u_n(t) = u_0 \sin(Q(na - vt) + \varphi_0), \Delta\rho(x,t) = \rho_0 \cos(Q(x - vt) + \varphi_0), \quad (2.12)$$

where $Q = 2k_F$ is the wave number of the CDW, and the velocity v of the CDW is proportional to the displacement current of the CDW j_{CDW}. The understanding that the periodic modulation is not important for the collective current follows from the fact that this current is observed and derived also for the spin density wave, where there is no charge modulation at all. But beyond this periodic current, there is still a continuous current from the ground state. We shall see that in the next section. The Fröhlich conductivity in CDW originates from the translational invariance, which is broken by the commensurability with the lattice, or by the interactions with the defects, or the impurities in the host lattice: the CDW can be pinned.

2.6.2 Collective mode of CDW: Amplitudon and Phason

Starting from the Fröhlich Hamiltonian, P.A. Lee, T.M. Rice and P.W. Anderson [25] have shown that the CDW state posesses two modes of collective excitations called the amplitudon (a gapful mode) and the phason (acoustic mode), which have the dispersion relations respectively:

$$\Omega_+ = \sqrt{\lambda\omega_a^2 + \frac{1}{3}\frac{m}{m^*}v_F^2 q^2}, \quad (2.13)$$

$$\Omega_- = \sqrt{\frac{m}{m^*}} v_F q = uq, \ \frac{m}{m^*} = 1 + 4\frac{\Delta^2}{\lambda \omega_{2k_F}^2}. \tag{2.14}$$

Here m is the effective band mass of electrons, and m^* is called the "effective mass" of the CDW. Typically for a Fermi energy $\varepsilon_F \sim 1eV$, a gap $2\Delta \sim 0.1eV$, phonon frequency $\omega_{2k_F} \sim 10^{-3}eV$, and the electron-phonon coupling constant $\lambda \sim 0.5$, we estimate $\Omega_+(q = 0) \sim 5.10^{-3}eV$ which is much smaller than Δ and gives a very high $m^*/m \sim 10^3$ as indeed observed experimentally in optics. Because of the gap in the dispersion relation for the amplitude mode, the low frequency collective dynamical phenomena involve only the phase mode. Notice that the relation (2.14) for $\Omega_-(q)$ shows in another way that the Fröhlich collective current can exist in a perfect crystal. However, for a real crystal with defects, it was shown [25] that the phason mode Ω_- possesses also a gap corresponding to a mean pinning energy of the CDW. Hence it becomes an optic mode, which can be determined for example by measuring the frequency dependence of the optical conductivity. As shown in figure 2.8, this pinning energy is generally weak for the quasi-1D components, typically being three orders of magnitude smaller than the gap 2Δ.

Physically, the amplitudons correspond to the oscillations of the amplitude Δ of the CDW, then the phasons correspond to the continuous translation of the electronic density accompanied by a harmonic movement of the atomic vibration (see Figure 2.9). This phason model which is coupled to the applied electric field, can give birth to a collective transport of the charge, which adds to the process of the non-condensed charges transport.

The phase-only approach [26, 27, 28] resides upon the 1D Lagrangian

$$\mathcal{L} = \int \hbar v_F \left(\frac{1}{u^2} \left(\frac{d\varphi}{dt} \right)^2 - \left(\frac{d\varphi}{dx} \right)^2 \right) dx. \tag{2.15}$$

where n is the carrier density along the chain direction.

This looks perfectly justified phenomenologically and it is supposed that the elimination of the electronic degrees of freedom from the Hamiltonian (2.2) [26] gives this form of Lagrangian. Actually, we shall see that there are important complications and reservations.

The first term on the right-hand side represents the kinetic energy. The

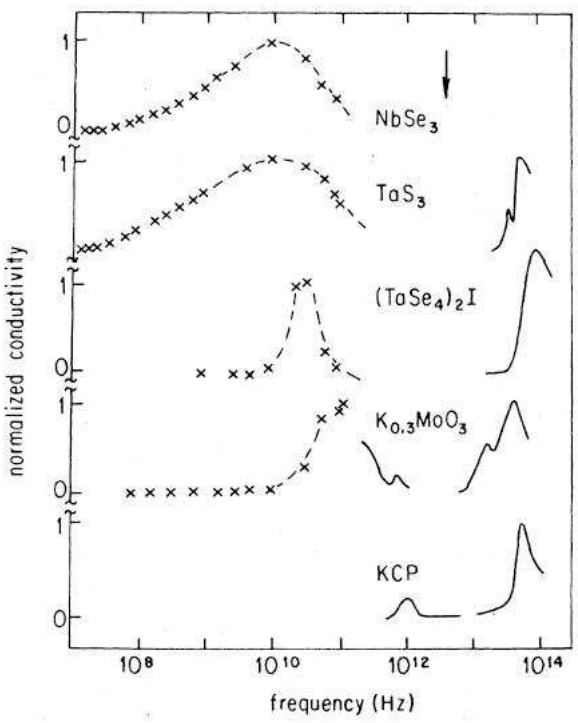

Figure 2.8: The frequency-dependent conductivity of $NbSe_3$, o $- TaS_3$, $(TaSe_4)I$ and $K_{0.3}MoO_3$. The solid lines in the high frequency region indicate the suppression of the single particle spectrum because of the CDW formation. The strong peaks in the millimeter wave spectral range are due to the response of the pinned collective mode. (after [5])

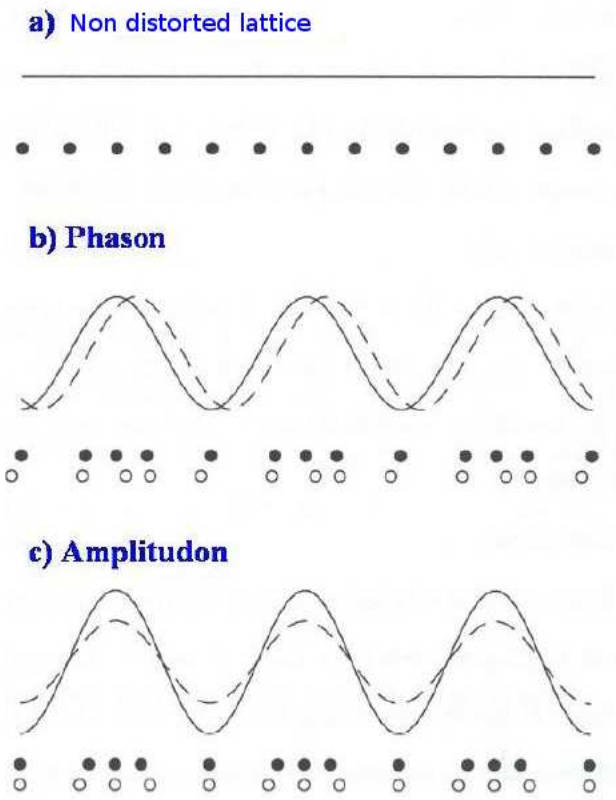

Figure 2.9: Illustration of a phason and an amplitudon for $q \to 0$ of a linear atomic chain. a.) the line represents the uniform density of the electron gas in the metallic state, the atoms are represented by the full circles. b.) the phason mode is represented by the position of the electronic density and the atoms in two successive moments (continuous line and full circles, dash line and empty circles) c.) the amplitudon mode is illustrated in the same way (after [7]).

second term corresponds to the potential energy associated with the distortion of the collective mode.

The plane-wave solution represents the periodic compression and expansion of the CDW; these excitations are called phasons, they are seen in experiments on inelastic neutron scattering.Their properties are given by the equation (2.16)

(The v_F estimation move to 2.16) For $v_F \sim 3\times10^7 cm/sec$ and for $m^*/m \sim 10^3$, u is approximately $10^6 cm/sec$.

This theory is not sufficient when when the Coulomb interactions should be taken into account, unless they are effectively screened by normal carriers. More details on the theory will be presented in the later chapters.

In summary, the electronic spectrum of the CDW can look similar to semiconductors, but the electric properties of the CDW state are completely different because of the collective phase mode.

2.7 Charge and current of charge density wave

As in a superconductor, the phase $\varphi(x,t)$ plays an important role in the dynamics of the collective mode. At zero temperature $T = 0$ we can write

$$n_c = \frac{e}{\pi}\frac{d\varphi}{dx}. \tag{2.16}$$

A rigid displacement of the CDW leads to the electric current, and the current density per chain j_{cdw} is given as

$$j_{cdw} = -\frac{e}{\pi}\frac{d\varphi}{dt}. \tag{2.17}$$

The cross derivatives of n_c and j_{cdw} lead to the charge conservation equation

$$\frac{dj_{cdw}}{dx} + \frac{dn_c}{dt} = 0. \tag{2.18}$$

At finite temperature, equations (2.17, 2.16) should be generalized to take into account changes of the amplitude (normalized) $A = \Delta/\Delta_0$ of the order parameter. The suggested forms read,

$$n_c = \frac{e}{\pi}A^2\frac{d\varphi}{dx}, \tag{2.19}$$

$$j_{cdw} = -\frac{e}{\pi} A^2 \frac{d\varphi}{dt}, \tag{2.20}$$

Indeed, these expressions are correct for homogeneous states, when A is constant. However, this generalization brings us a new problem of non-conservation of charge. If A is not constant as this will be in our work, equation (2.18) becomes

$$\frac{dj_{CDW}}{dx} + \frac{dn_c}{dt} = \frac{e}{\pi} 2A \left(\frac{dA}{dt}\frac{d\varphi}{dx} - \frac{dA}{dx}\frac{d\varphi}{dt} \right) \neq 0. \tag{2.21}$$

- the collective charge is not conserved! A resolution of this difficulty will be proposed in the later chapters by going beyond the Ginzburg-Landau theory by taking into account the electronic excitations explicitly together with the order parameter.

2.8 Two types of normal carriers

In a CDW system there may be two types of normal carriers, and each of them has its own properties. There are intrinsic carriers n_{in} and extrinsic ones n_{ex}. They play different roles with respect to the CDW, and they experience different electronic potentials. Extrinsic carriers are coupled with the CDW only via the Coulomb potential; the intrinsic carriers are coupled with the CDW also by the CDW deformation. For the intrinsic carriers, the electronic spectrum is formed by the CDW gap and their energies move up and down, when the Fermi level breathes as $\delta\varepsilon_F = \hbar v_F/2\, \partial\varphi/\partial x$. Their density is affected by the changes of the Fermi level. While they need to be activated across the gap, n_{in} exist in all CDW materials, see figure (2.10). Extrinsic carriers belong to other bands or to other well-decoupled CDWs. Among known quasi-1D CDW compounds, this is the case of $NbSe_3$ between two CDW transitions. Many quasi-2D CDW compounds, e.g. $TbTe_2$, and TaS_2 keep non-gaped parts of the Fermi surface because of the uncompleted nesting of their Fermi surface. Hence, the extrinsic carriers are present.

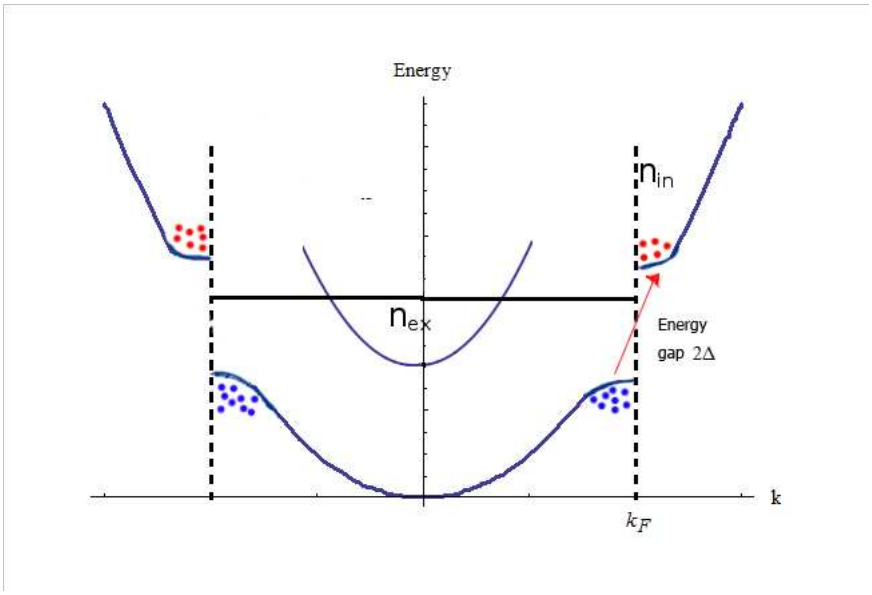

Figure 2.10: Electrons and holes are excited from the CDW by the thermal energy k_BT and become intrinsic carriers.

2.9 Pinning of the charge density wave

The interaction between impurities and the CDW has fundamental consequence for both static and dynamic properties. The first important consequence is the huge dielectric response ϵ, see figure (2.11 A). The pinning limits the growth of the electric response $\epsilon(q) = r_0^{-2}/q^2$ at $\epsilon \sim L_{pin}^2/r_0^2$ where L_{pin} is the pinning length, so the observed huge value of $\epsilon \gtrsim 10^6$ indicates to large L_{pin}. The second important consequence of pinning is an appearance of a critical voltage E_t corresponding to CDW depinning when the collective current can slide [29, 30], see figure (2.11 B).

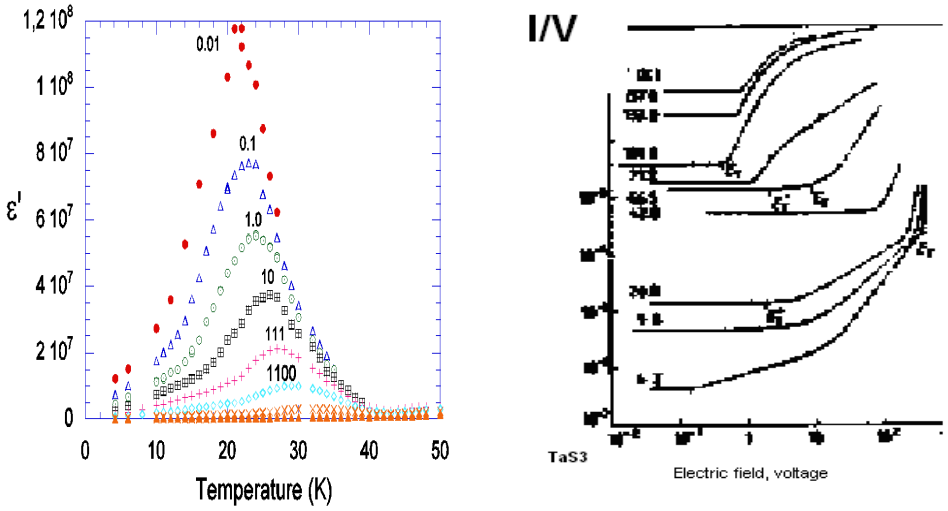

A B

Figure 2.11: A: Measurement of the real part ϵ of the dielectric permittivity as a function of T at different ω in Blue Bronzes. Large $\epsilon \sim 10^6$ is found [31]. B: Measurement of the nonlinear conductivity in TaS_3 at low temperatures. A sudden increase of the current after passing the threshold voltage E_T is observed. [32]

At first argued by A. Larkin [33] and later in [34, 35, 36], the long-range order is destroyed by randomly positioned impurities, and, in less than four dimensions, the phase-phase correlation function decreases exponentially with distance. However, more recently it became clear that the decay is actually a power law [37, 38, 39], also see [40] for a most recent review .

The Hamiltonian for the phase coupled to impurities is [28]

$$H = \frac{\hbar v_F}{4\pi s}\int (\nabla\varphi)^2 d\vec{r} + \int \rho V(\vec{r}) \cos\left(2\vec{k}\cdot\vec{r} + \varphi(\vec{r})\right) d\vec{r}. \tag{2.22}$$

The first term on the right-hand side represents the rescaled elastic energy associated with the long-wave length phase deformation; the second represents the interaction of the CDW with the pinning potential. It is assumed that the CDW amplitude is not perturbed by the interaction with the impurities. Consequently, the equation (2.22) is expected to be appropriate for relatively weak potentials, which are substantially smaller than the CDW gap 2Δ. The interaction between the incommensurate CDW and defects in the host crystal originates the pinning force.

We can distinguish two types of pinning, the collective pinning and the local ones. The collective pinning forces come from elastic interference of many impurities. They have large correlation volumes, huge relaxation times and small magnitude. The collective pinning determines the threshold F_t of the driving force to initial the CDW sliding and it is quite similar to conventional rest friction. The local pinning concerns the local properties of individual pinning center which relaxation rates are short. The local pinning force may depend on the sliding velocity of the CDW. The local pinning gives the frequency-dependence of the CDW response and the strongly nonlinear I-V curve.

At low temperature, the CDW becomes more rigid and the effects of local pinning dominate. The local pinning force can be calculated by building up several models, such as, an elastic model, or a short-range model. Here we summarize the main results from these calculations [40]. By considering the stationary process, when the CDW moves with a constant phase velocity $v = \partial_t\varphi/2\pi = const$, the local pinning force F_{pin} is shown to follow different v-dependent laws according to the value of v, see figure 2.12. The important parameters are the single-impurity force F_1 and its maximal value F_1^{max}, the

activational relaxation rate τ, and the temperature T. At small velocities,

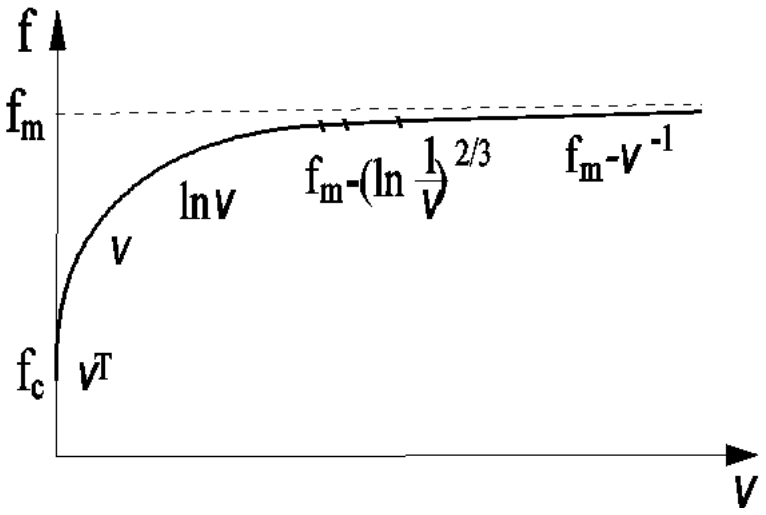

Figure 2.12: Schematic plot of the pinning force F_{pin} in function of CDW phase velocity v showing several regimes of v-dependent laws. [40]

F_{pin} is linearly proportional to v:

$$F_{pin} = n_i F_1 \tau v \quad v < v^* \sim (T/(F_1\tau) \tag{2.23}$$

At moderately small velocities, F_{pin} increases logarithmically with v. At high velocities, F_{pin} follows the law of $F_{pin} - F_1^{max} \sim -\left(\ln \frac{1}{v}\right)^{2/3}$. For even higher velocity, F_{pin} varies according to $F_{pin} - F_1^{max} \sim -v^{-1}$. Interestingly for our goals, the last regime corresponds to depinning by creation of pairs of dislocation loops. (For the collective pinning, the role of dislocations was discussed in [41] and [42].)

The most important information from the above $F_{pin} - v$ diagram is appearance of the linear $F_{pin} - v$ law valid below a critical velocity $v^* \sim (T/(F_1\tau).)$. The tangent of this linear segment will give the phase damping parameter γ_φ. This simple viscosity law will be used in our work as well as in most existing studies.

Chapter 3

Dislocations in charge density waves.

In this chapter, we outline definitions and main concepts for dislocations in applications to CDWs. We describe the types of dislocations and of their motion. Finally we describe experiments indicating an important role of deformations and dislocations in CDWs.

3.1 General concepts in dislocations.

3.1.1 Definitions

A dislocation is a kind of a topologically nontrivial line defect within a crystal structure [43, 44, 45, 42]. Its existence manifests the crystal periodicity: following any path around the dislocation line, a nonzero displacement $\vec{B}$ is acquired which must coincide with one of the crystal's periods. This displacement is called a Burgers vector, and only primitive periods give stable dislocations. Mathematically, the Burgers vector $\vec{B}$ is defined by integration around a Burgers circuit C enclosing the dislocation line:

$$\vec{B_i} = \oint_C \nabla_j \vec{u_i} d\vec{r_j}, \tag{3.1}$$

where $\vec{u}$ is the displacement vector and $\nabla\vec{u}$ is its local gradient.

There are two main types of dislocations: the screw and the edge ones. The Burgers vector is parallel to the dislocation line for the screw dislocation, figure 3.1, and it is perpendicular for the edge dislocation, figure 3.2.

The CDW is a particular case of the crystal where displacements, hence the Burgers vector, are allowed only along the chain axis $\vec{x}$. So, in the CDW, $\vec{B} = B\vec{x}$ is defined as [45]

$$\vec{B} = \frac{\lambda}{2\pi}\vec{x}\oint_C \nabla\varphi d\vec{r}, \tag{3.2}$$

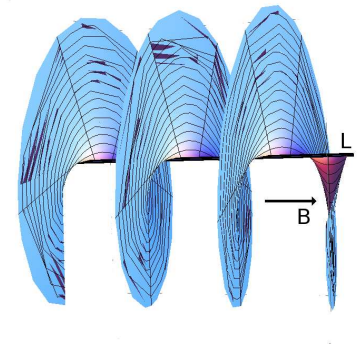

Figure 3.1: Screw dislocation. L is the dislocation line, and B the Burgers vector.

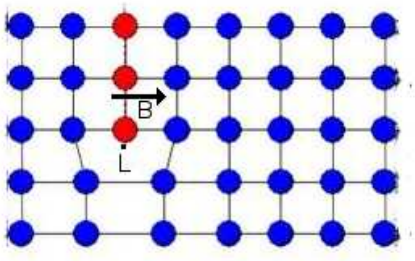

Figure 3.2: Edge dislocation. L perpendicular to the plan is the dislocation line, and B the Burgers vector.

Formation energies for these two types of dislocation are different. In general, a screw dislocation involving only the shear strain has a lower energy [43]. In CDWs this difference can be even more pronounced because of the structural anisotropy - the small share modulus (see section 3.1.1) $\alpha_{y,z}$. But in absence of screening by normal carriers, the edge dislocation is even more costly energetically: it activates the charge density $\sim \partial_x\varphi$, hence the Coulomb energy. Still, the emergence of dislocations appearance is ultimate in effects of reconstruction and conversion while the neutral screw dislocations may appear only accidentally. Figure 3.3 gives the scheme of dislocations in the CDW.

These illustrations, as well as most common treatments within the elastic theory, rely on low energy gapless perturbations: acoustic ones conventionally, reduced to the phase mode in CDWs. Actually, the elastic approach fails

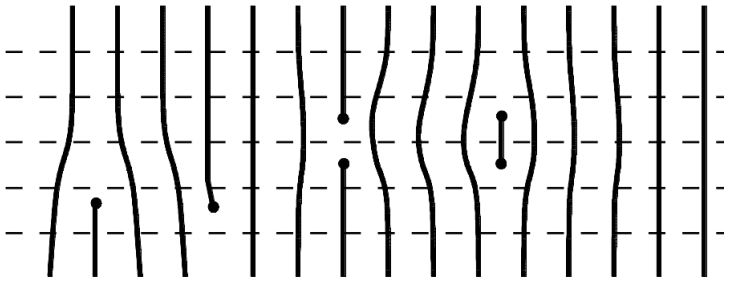

Figure 3.3: Dislocations in a CDW. The solid lines describe the maxima of the charge density. The dashed lines represent chains of the host crystal. From left to right: dislocations of opposite signs and their pairs of opposite polarities. Embracing only one chain of atoms, the pairs becomes a vacancy and an interstitial or $\mp 2\pi$ soliton. Bypassing each of these defects, the phase changes by 2π thus leaving the lattice far from the defect unperturbed. [40]

approaching the dislocation core. In terms of the CDW, there is a divergence of the elastic energy from the phase gradient $\nabla\varphi \sim 1/r$. By consequence, the amplitude of the CDW complex order parameter vanishes at the core as we shall see in our simulations.

3.1.2 Kinematics of dislocations

By definition, going around a dislocation line τ or crossing a dislocation loop, the CDW complex order parameter phase $\varphi(\vec{r})$ gains a $\pm 2\pi$ increment at some, largely arbitrary chosen, surface $\vec{P}$, see figures 3.4, and 3.5. It makes the phase a discontinuous not uniquely defined function - otherwise it would be a multiply defined function. More complicated situations happen when the dislocations are in motion, which makes these discontinuities time dependent. To clarify this situation, we must distinguish two types of dislocation motion: glide and climb [42, 45]. In the course of glide, the dislocation loop does not cross chains. The glide is allowed only in the direction of the Burgers vector of these edge dislocations that is along the chain axis for CDWs, see figure 3.6. In the course of the climb, the dislocation loop grows or shrinks changing the number of embraced chains, see figure 3.7. The climb provides the transfer of particles between the condensate and the normal liquid, and this will be

an important motive for the discussion in chapter 8. Sliding of dislocations gives the plastic flow, where many defects are involved in average.

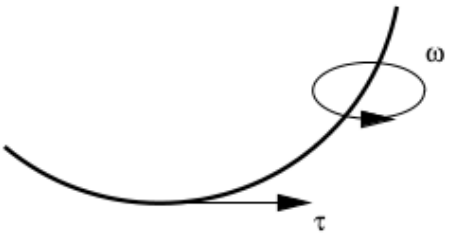

Figure 3.4: Dislocation line τ with circulations of the phase gradient ω. [46]

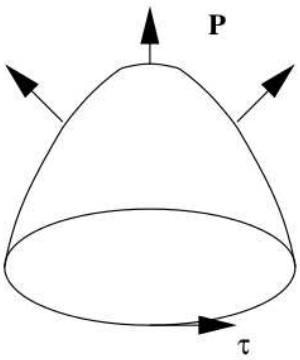

Figure 3.5: The surface $\vec{P}$ of the phase discontinuity based upon the dislocation loop τ. [46]

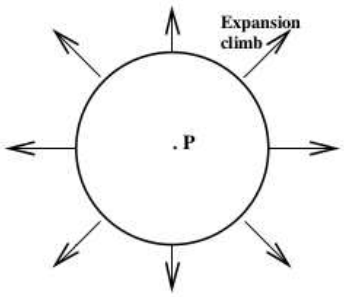

Figure 3.6: Expansion of the dislocation loop in the course of its climb. Arrows show the climb directions. The surface vector $\vec{P}$ is perpendicular to the plane. [46]

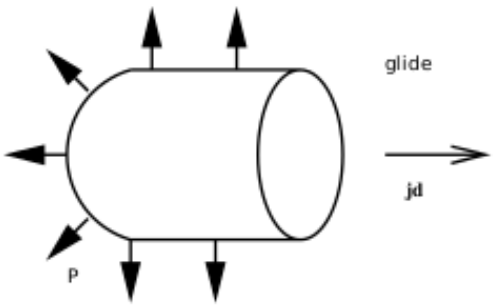

Figure 3.7: Propagation of the dislocation loop in the course of its glide. Vectors show the surface of the phase discontinuities. [46]

3.2 Elastic and plastic deformations of charge density waves

The early theory and the first concept for dislocations in CDWs was put forward in 1980s by D.Feinberg and J.Friedel, see [42] and [45] for a review with a number of new results. These authors put forward the idea of an "electronic solid", akin to the later term the "electronic crystal". They realized that the CDW is a crystal, even if of electrons, and as such described by strain and stress. They made a connection of the internal rigidities for CDW deformation and motion with those in a normal solid. In that view, an external electric field becomes equivalent to stresses exercised on a solid. A particularly important, and inspiring for us, was to notice the possibility of topological defects related to the periodic symmetric breaking: the dislocations.

D.Feinberg and J.Friedel described the nucleation of CDW defects as a thermal activation process in presence of a local elastic stress T. By balancing between the internal elastic energy of the CDW and the deformation loop energy, they finally found a critical strain

$$\tilde{e_c} = \frac{\lambda}{4\pi\tilde{\xi}} = \left(\frac{\lambda}{4\pi\xi_x}, \frac{\lambda}{4\pi\xi_\perp}\right), \tag{3.3}$$

where λ is the CDW wavelength and ξ_x and $\xi_\perp$ are the coherence lengths along and perpendicular to the chain axis. This critical strain can be used to calculate a critical voltage, when the strains are due to an external electric field. These studies underlined the combined effect of external electric field and pinning points. Under low stresses the globally pinned condensate retains phase continuity: the structure has no defects. Under strong stresses the dislocation loops are nucleated involving local amplitude variation of the CDW. Also the estimations have been given for effects of variations of the CDW amplitude A, which were interpreted as a modification of the elastic constant.

To justify such a picture, certain conditions must be satisfied. First a low temperature, far enough below the Peierls transition is necessary to solidify the CDW. Secondly, the long-range Coulomb interactions were neglected;

they were supposed to be screened by the normal carriers. The first condition is easily fulfilled, while the second one requires for a large concentration of normal carriers, e.g. in CDWs with incomplete closing of the Fermi surface. As we will see in the next section, the CDW with Coulomb interaction can be incorporated to the traditional picture of dislocations.

3.3 Dislocations in the CDW with Coulomb interaction

In 1990s, S.Brazovskii and S.Matveenko in a series of papers [47, 48, 49] studied the CDW dislocations by taking in full account the Coulomb interactions.

They worked with the following energy functional

$$H = \int \frac{1}{s} d\vec{r} \left(\frac{\hbar v_F}{4\pi} \left(\left(\frac{\partial \varphi}{\partial x} \right)^2 + \alpha \left(\frac{\partial \varphi}{\partial r_\perp} \right)^2 \right) + \frac{\Phi}{\pi} \frac{\partial \varphi}{\partial x} - \frac{\epsilon_\infty}{8\pi e^2} \left(\nabla \Phi \right)^2 s \right), \tag{3.4}$$

where the static electric potential Φ has to be determined self-consistently. From this free energy, they calculated distributions of phase deformations and the electric field, found the energy for the dislocation and the soliton and interactions between those objects and to impurities. The Coulomb potential had drastically increased the dislocation energy: from the weak logarithmic law $\sim \ln r$ to the linear confinement law $\sim r$ (In a later work [50] that was called the "Coulomb blockade"). The distributions changes from typical dipole laws to exponential $\sim \exp(-y^2/d|x|)$ laws, extremely concentrated along the chain direction.

The Coulomb interactions can be limited by screening from the normal carriers. The effect of screening by residual electrons on the inner structure of a dislocation becomes important when the screening length l_{scr} is smaller than the distance to the dislocation line Y, that's $l_{scr} \ll Y$. As a result, more conventional expressions for the phase and the electric field appear at

large distances

$$\varphi = \frac{s}{4\alpha^*}\frac{\partial}{\partial x}\frac{1}{\left(x^2 + r_\perp^2/\alpha^*\right)^{1/2}}, \tag{3.5}$$

$$\Phi = \frac{v_F}{2}\frac{\alpha}{\alpha^*}\frac{\partial}{\partial x}\varphi, \tag{3.6}$$

where

$$\alpha^* = \alpha\frac{l_{scr}^2}{r_0^2} \ll \alpha,\ r_0^2 = \frac{8e^2}{\hbar v_F \epsilon s}. \tag{3.7}$$

Thus, the phase distribution is determined by the effective problem for a dislocation without the Coulomb field, but with an enhanced anisotropy α^* which is the effect of the "Coulomb hardening".

3.3.1 Static studies of the electric potential in CDW

In this section, we give calculations for a static electric potential in presence of a single dislocation in the infinite media, well beyond the dislocation core when the amplitude is saturated. The Hamiltonian in study reads,

$$H = \frac{\Delta\xi}{4\pi s}\int dxdy\Big(\left(\partial_x\varphi\right)^2 + \beta^2\left(\partial_y\varphi + \pi\Theta(-x)\delta(y)\right)^2 + \frac{4}{\xi}\frac{\Phi}{\Delta}\frac{\partial\varphi}{\partial x} - 4\frac{r_0^2}{\xi^2}\left(\nabla\frac{\Phi}{\Delta}\right)^2 - \frac{1}{l^2}\left(\frac{\Phi}{\Delta}\right)^2\Big). \tag{3.8}$$

The first term in H is the elastic energy of the CDW compression. The second term is elastic energy of share deformation. Here the phase φ is a single valued function but not differentiable everywhere and a branch along the negative-x axis is introduced by the function $\Theta(-x)\delta(y)$ (Θ is the Heaviside step function.). The third term is the coupling between the CDW charge $e/\pi\ \partial_x\varphi$ and the electric potential Φ. (Here and later on, the electric charge e is absorbed by Φ, which becomes the electric energy.) The forth and fifth terms are the energy of the electric field and the screening by normal carriers.

The Fourier transform of equation (3.8) and variations with respect to Φ and φ gives two equations:

$$\frac{\delta w}{\delta\varphi(-\vec{k})} = \left(k_x^2 + \beta^2 k_y^2\right)\varphi(\vec{k}) + \pi\frac{ik_y}{ik_x} + \frac{i4k_x}{\Delta\xi}\Phi(\vec{k}) = 0, \tag{3.9}$$

$$\frac{\delta w}{\delta \Phi(-\vec{k})} = \frac{-4ik_x}{\Delta\xi}\varphi(\vec{k}) - \frac{4r_0^2}{\xi^2\Delta^2}\left(k_x^2 + k_y^2\right)\Phi(\vec{k}) - \frac{1}{l^2\Delta^2}\Phi(\vec{k}) = 0. \tag{3.10}$$

From equations (3.9 and 3.10), we have

$$\Phi(\vec{k}) = \frac{i\pi\Delta k_y\xi}{k_x^2 + r_0^2(k_x^2+k_y^2)(k_x^2+\beta^2k_y^2) + \frac{r_0^2}{l^2}(k_x^2+\beta^2k_y^2)} \tag{3.11}$$

We study the large distances limit, apparently at least in comparison with r_0, hence $k_{x,y}$ are small. l is large with respect to r_0, so the kl magnitude is not defined yet. With this approximation, the potential Φ in equation (3.11) becomes,

$$\Phi(\vec{k}) = \frac{i\pi v_F k_y}{k_x^2 + r_0^2\beta^2k_y^4 + \frac{\beta^2r_0^2}{l^2}k_y^2} \tag{3.12}$$

The inverse Fourier transform will give the electric potential value in real space,

$$\Phi(\vec{r}) = \frac{\Delta\xi}{\beta r_0}\int_{-\infty}^{\infty}\frac{dk_y}{2\pi}\frac{k_y\sin(k_y y)}{\sqrt{k_y^4 + k_y^2/l^2}}\exp\left(-|x|\beta r_0\sqrt{k_y^4 + k_y^2/l^2}\right) \tag{3.13}$$

Figure 3.8 gives the 3D plot of the potential, and figure 3.9 is the cross-section plot of the potential by passing transversely the vortex center, the line $x = 0$.

We can see a strong drop of the potential at the center of the vortex and

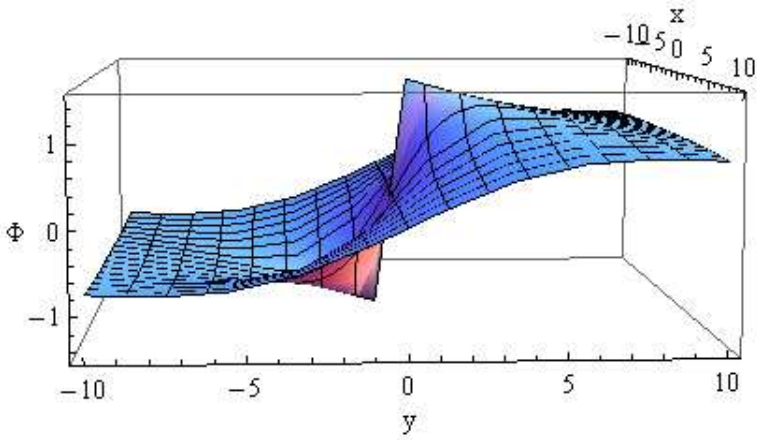

Figure 3.8: The calculated electric potential Φ.

the potential goes to zero far away form the center. In the limit of large

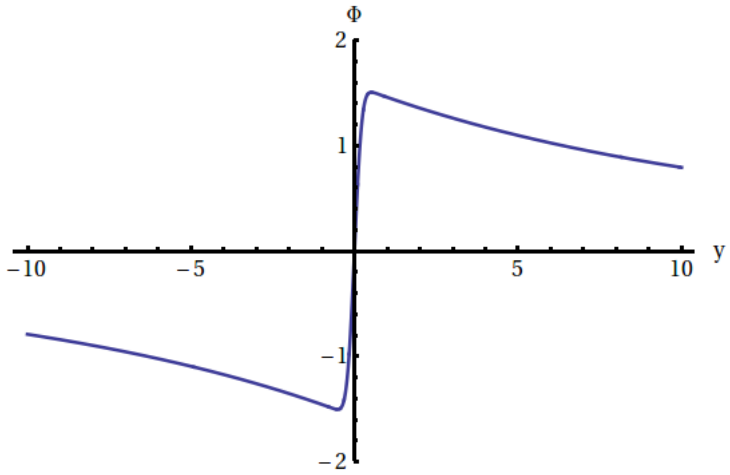

Figure 3.9: The cross-section plot of the electric potential Φ by passing the vortex center.

screening length $l \to \infty$, with the help of equation (3.13) the y component of electric field $E_y = -\partial_y \Phi$ can be evaluated as

$$E_y \sim \frac{\Delta\xi}{d} \int_{-\infty}^{\infty} \frac{dk_y}{2\pi} \cos(k_y * y) \exp\left(-k_y^2 |x| d\right) \sim \frac{\Delta\xi}{\sqrt{|x|d}} \exp\left(-y^2/|x|d\right), \tag{3.14}$$

where $d = \beta r_0$.

If we consider the full expression (3.11) of the potential Φ, the numerical 2D Fourier transform can be preformed to obtain Φ in the real space,

$$\Phi(\vec{r}) = \int_{-\infty}^{\infty} \int_{-\infty}^{\infty} \frac{dk_x dk_y}{4\pi^2} \frac{i\pi\Delta k_y \xi \sin(k_y y)\cos(k_x x)}{k_x^2 + r_0^2(k_x^2 + k_y^2)(k_x^2 + \beta^2 k_y^2) + \frac{r_0^2}{l^2}(k_x^2 + \beta^2 k_y^2)} \tag{3.15}$$

The cross-section plot of this function by passing through the vortex center is given by figure 3.10. In the figure, the potential presents a sharp drop at the vortex center, after a small increase (or decrease in the negative side) in the positive side, it goes to zero at infinity. At small y, the contribution to the integral comes from large k_y, which is the Fourier transform of $1/k_y$, that is the sign function in real space. But for $y >> l$, hence $k_y >> 1/l$, another approximation applies, giving vaguely the integral as $\sim k_y/(k_y^2(r_0/l)^2 + k_x^2)$. This is the Fourier transform of the dipole, so in real space we get $y/(y^2 + x^2(r_0/l)^2)$, which decays at large y. All together we find that the potential

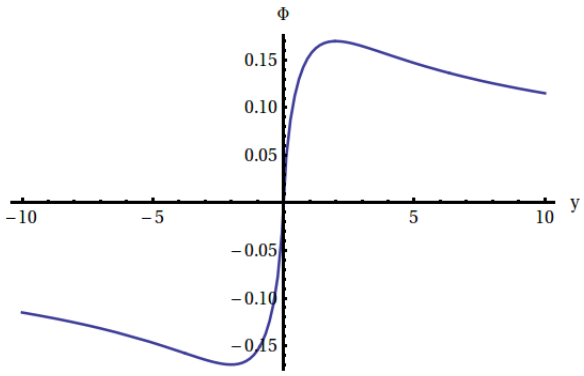

Figure 3.10: The cross-section plot of the electric potential Φ by passing transversely through the vortex center.

Φ has a sharp jump across the vortex core on the scale of r_0, from zero at $y = 0$ to nearly the plateaux at $|y| < l$, and then it decays at distance larger than l.

In this section, we have used the Fourier transform method to calculate the distribution of the electric potential around a vortex core, which gives a result comparable to those, which will be found in later sections for a nonlinear problem. However limited by the linear regime, these studies allow us to access only to the static state of the potential and also the calculation is based on the reduced Hamiltonian, which can give only a basic understanding of the problem. In the following sections, we shall develop a theory which permit to study not only the stationary vortex state in CDW, but also its dynamics in the full scope of the nonlinear problem.

3.4 Plastic flow evidenced from X-ray space-resolved diffraction

In this section, we summarize the space-resolved X-ray studies for local deformations measured in the sliding state of the CDW. They give clear evidences for the current conservation accompanying phase slippage, presumably provided by transverse flow off dislocations - by definition it is called the plastic regime of sliding, in contrast with the regular elastic one. A brief introduction of the microscopic model from [51], explaining this process will be given

at the end of this chapter.

We shall exploit the systematic studies performed in Grenoble ([52, 51, 53]), recall also the important work done in Cornell, see the above references for a review. Experiments were preformed on the $NbSe_3$, in the regime of the upper CDW1 that is between the two Peierls transitions at $145K$ and $59K$. The experimental setup is built on a two-contact configuration, meanwhile the X-ray beam with a space resolution of $30\mu m$ was focused on the sample, as shown in figure 3.11, from the references [53].

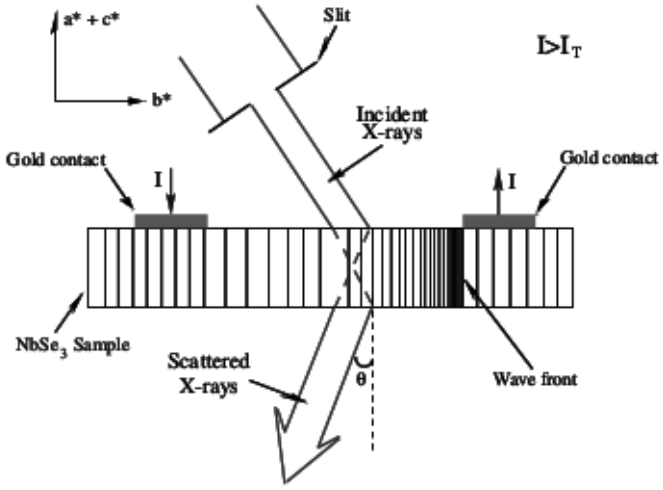

Figure 3.11: Sketch of the X-ray scattering geometry [53].

The shift $q(x)$ of the sliding CDW satellite peak position in the reciprocal space, $Q = Q_0 + q(x)$ was measured as a function of the beam position x along the sample. The longitudinal shift of the CDW wave vector is observed to have a systematic position dependence, with strong variations near the two electrodes.

3.4.1 Experimental results

Figure 3.12 A shows shifts (for two current polarities) $q_+ = Q(+I) - Q(0)$ and $q_- = Q(-I) - Q(0)$ as a function of the beam position x along half of the sample $(0 < x < 2mm)$ for an applied current $|I| = 7.5mA = 3.52I_T$

(I_T is the critical current) at $T = 90K$. For both polarities, the q shift reaches its maximum at the contact boundary, which indicates important CDW deformations in that region.

Figure (3.13 A) shows the shift $q(x)$ measured on a different sample, where there is a localized defect at the position $x_d \approx -0.15mm$. The sliding CDW satellite shift changes sign abruptly at this position, with maxima on either sides of the defect position. Comparison of two figures (3.12 A) and (3.13 A) tells that the hidden defect plays the role of the pseudo-contact, hence the imbalance of normal carriers is generated witnessing processes of (re)conversion by means of phase slips.

Figure (3.13 B) shows the shift of q in comparison between a defect-free sample and the same sample but after a damaged layer had been created on purpose by a long exposure to the focused beam. We see strong elastic deformations spread over approximately $200\mu m$ on either side of the irradiated position. The modeling with a good fitting shows that the current conversion is minimal in this case: just the elastic deformations are build-in which additional stress allows the CDW to slide through the layer of the enhanced pinning force. We can conclude that CDW deformations, elastic and plastic, are not uniquely the contact effects but also may take place in vicinity of structural defects - natural or hand-made.

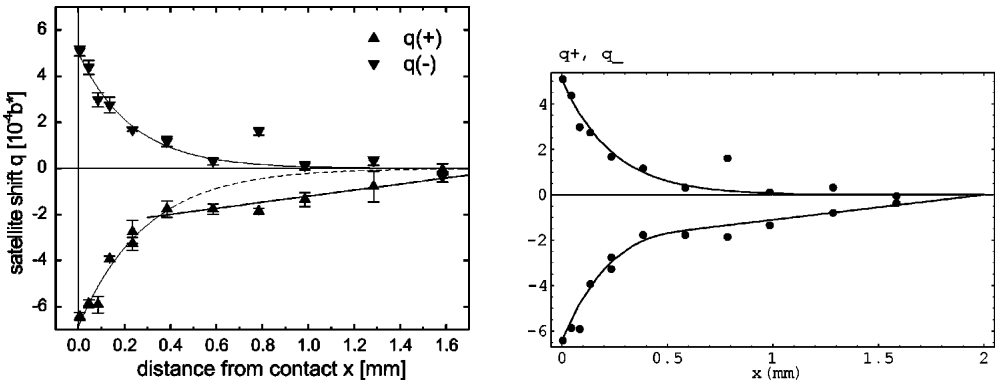

A B

Figure 3.12: A:q shift (in units of b^*) for positive (q_+)(negative q_-) applied direct current ($I = 3.52 I_T$), for one-half of the sample $0 < x < 2mm$. The contact boundary is at $x = 0$ (vertical grey line). The horizontal grey line is the line for $q = 0$. q_- is fitted with an exponentially decaying spatial profile, and q_+ has similar characteristic near the contact boundary. $NbSe_3$, $T = 90K$. B: Calculated $q(x)$ profile for the same experiment conditions. [51]

3.4.2 Model

The model explaining the observed q shifts vaguely takes into account the conversion between the normal and the condensed electrons. It assumes the phase slips, which are provided by nucleation and growth of multiple dislocation loop, but these elementary acts a beyond the scale of the course-grained model which operates with variables averaged over long time and rather long distances.

There are two types of normal carriers in the upper CDW state of $NbSe_3$: intrinsic carriers and extrinsic ones (see section 2.8). We define the stress U in the CDW,

$$U = \left(\frac{q}{\pi} + \delta n_i\right) \frac{1}{N^i} + \Phi, \; N_i = \frac{2}{\pi \hbar v_F}, \tag{3.16}$$

where δn_i is the variation of the intrinsic carriers density, N^i is the density of states of at the Fermi level of the parent metal, and Φ is the applied potential. U has three contributions: the elastic stress, the stress provided by the excess concentration of intrinsic carriers, and the electric field.

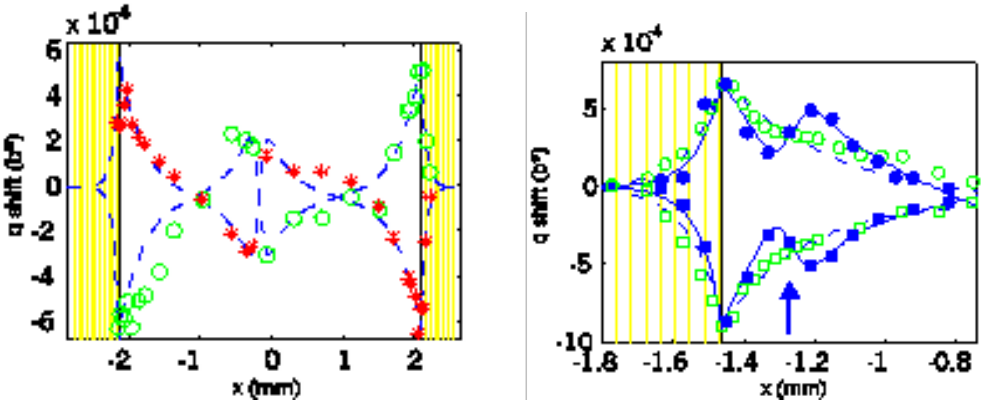

A B

Figure 3.13: A:Shift $q(x)$ of the CDW satellite peak position as a function of beam position x for positive ($*$) and negative ($\circ$) polarities. The vertical lines show the boundaries of contacts; dashed lines are the best fit solution to equation (3.19); $NbSe_3$, $T = 90K$. B: Shift $q(x)$ along the lhs part of the sample for positive ($\circ$) and negative ($\square$) polarities. Full symbols ($\bullet$ and $\blacksquare$) show the shift after a local irradiation at the arrow position. The vertical line shows the contact. Dashed and full lines give the best fit solution of the equation (3.19).

The CDW is deformed whenever the stress U - the energy of condensed electrons, cannot reach balance with the electrochemical potential of the normal carriers μ_n ($\mu_n = e\Phi + \partial_x\varphi/2$). The quantity $\eta \equiv \mu_n - U$ characterizes this mismatch. Hence the excess or lack of normal carriers (or condensed electrons) will distort the CDW, which is measured directly by q. The exchange between the normal carriers and the condensed electrons results finally in the equilibrium between μ_n and U, a process taking place via nucleation and growth of dislocations.

The conversion between different states of electrons modifies the carrier conservation law as

$$\frac{\partial(\delta n_c)}{\partial t} + \frac{\partial j_c}{\partial x} = \frac{d(\delta n_c)}{dt} = -\frac{dn}{dt} = \mathcal{R}(\eta, j_c), \tag{3.17}$$

by introducing a conversion rate $\mathcal{R}(\eta)$ between normal and condensed carriers. There are two extreme scenarios for $\mathcal{R}(\eta, j_c)$. The first refers to an ideal host crystal, both in the bulk and at the surface, where only homogeneous nucleation is present as a spontaneous thermal [54] or even quantum [55] supercritical fluctuation, so that $\mathcal{R} \propto \exp(-\eta_0/|\eta|)$, is valid at $|\eta| \ll \eta_0$. Another extreme refers to samples with a sufficiently large density of defects acting as nucleation centers for supercritical dislocations [45, 42], the simplest form for this case being $\mathcal{R} \propto \eta$, and this is what fits the experiment.

The above model, which includes the stress of the CDW U, the potentials of the normal and condensed electrons, the sliding current $-\partial U/\partial x \sim j/\sigma_{CDW}$, and enforces the local electro-neutrality, results in equation for the stationary distribution of the CDW deformation

$$\frac{\partial \eta}{\partial x} = F(j_c) - \frac{j_{tot} - j_c}{\sigma_n}, \tag{3.18}$$

where $F(j_c) = -\frac{\partial U}{\partial x}$ is the pinning force experienced by the CDW. j_{tot} is the total current. j_c is the collective current. σ_n is the normal conductivity.

Equation (3.18) can be specified to fit the experimental results, and we have [53]

$$\frac{\partial^2 \eta}{\partial x^2} = \frac{\eta}{h_0^2} + J_c \frac{\Delta\sigma_c}{(\sigma_c^0)^2}\left(\delta_{x_d - \xi/2} - \delta_{x_d + \xi/2}\right) + \frac{\nu_{inj}}{\sigma_c^0}, \tag{3.19}$$

with the boundary conditions $J_{tot} = 0$ at $|x| = a$. The first term in the r.h.s. is the phase slip rate (h_0 typically a few hundred μm.) The second

term provides a partial conversion of the CDW current at the defect position. This model was well verified by its application to calculate the q shift from the experimental data. Figure (3.12 B) presents the curve of the q shift form the model. The best fit solutions provided by the equation (3.19) are given by dashed lines and full lines in figure 3.13.

We give an illustration of what happens during the experiment by means of the figure 3.14. When the CDW is depined between the current contacts, the CDW wave fronts are created near one electrodes and destroyed near the other, leading to CDW compression at one end and stretching at the other. The order parameter is driven to zero, and vortices develop as dislocations climb between the crystal surfaces. Each sweep allows the CDW to progress by one wave length, thus the current is transported by the block movement of the CDW.

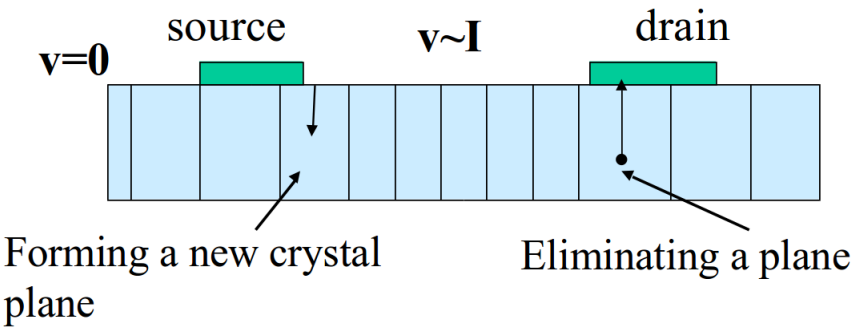

Figure 3.14: Schematic illustration of CDW dislocations at the electrodes. Edge dislocation line proliferates across the sample.

3.4.3 Phase slip

Phase slip is a common phenomenon in condensed matter system, and it happens when different phase-winding rates of the complex order parameter are imposed in different regions of a sample. Gor'kov, Ong, and Maki were among the first to introduce this concept in the CDW studies. They [56, 57] have proposed a mechanism of phase slip processes to explain the "narrow-band noise" observed in the electric transport experiments for CDW

compounds. Their idea of [56] was that under the strong electric field a train of vortices is created and proliferates perpendicular to the CDW current. These moving vortices become the centers to conversion between condensed electrons and normal carriers. The nucleation or annihilation of vortices near the contacts induces abrupt changes registered as voltage oscillations. This picture can be borrowed to explain the X-ray experiment. The "narrow-band noise" is the time-dependent observation of the phase slip processed, while the X-ray diffraction give a spacial observation of the same effect by average in time. Processes of defects' proliferation will be visualized in our simulations (reference chapter 6, 7).

Chapter 4

Reconstruction by dislocations of CDW junctions: experiment and motivation.

4.1 Introduction: Charge injection to the CDW

Tunneling experiments give an access to properties of electrons in solids by measuring the transition rates (the current I(V)) between adjacent parts of the sample under the applied voltage V. Usually the tunneling occurs between two different conductors across their hetero-junction or through a break of the same material. The more recent method is the tunneling within the same noninterrupted sample which is particularly effective in studies of strongly anisotropic (quasi two-dimensional or quasi one-dimensional) materials.

Usually it is supposed, being reasonably justified, that the junction formation and/or applying voltage do not modify electronic states which are measured then as virgin ones. At most, as it happens in e.g. tunneling transistor, one has to take into account the field effect of the charge penetration across the junction which accumulates some surface charge, accompanied by a built-in potential difference, so that to equilibrate Fermi energies (chemical potentials) of electrons on both side of the junction. But the situation may change drastically in correlated systems showing spontaneous symmetry breaking. There, the electronic spectra are formed self-consistently via in-

teractions of electrons, or among them and the underlying lattice of the host crystal. Then the spectra and the very nature of states readjust to changes of a local concentration of electrons and even to individual particles. Next and equally important is the appearance of collective modes which substitute normal electrons in the role of the charge transfer. The most known example comes from superconductors which collective response to the applied electric field originates the intrinsic Josephson effect. These oscillations were efficiently studied just by the experimental setup addressed below. But what will happen in electronic crystals, particularly in CDWs?

A natural temptation is always to treat them as semiconductors (sometimes semi-metals). But here we immediately realize the presence of the collective mode, which is the overall translation of the electronic crystal, leading to a sliding conductivity or to a corresponding gigantic dielectric response as we have reviewed above. One of main features of electronic crystals is that the number of unit cells is not fixed and can be readjusted to absorb transferred electrons to the new extended ground state. Particularly intriguing expectation is that locally the addition of electrons to the condensates of the crystalline order goes on via topologically nontrivial deformations: discommensurations, dislocations, solitons. We shall recall that most, and potentially all of these effects are present and show up in the intrinsic tunneling experiments.

In real CDWs, the crystalline order of singlet electronic pairs is weak, such that the electronic density and the associated lattice deformation are nearly sinusoidal $\sim \Delta\cos(Qx+\varphi)$. The arbitrary chosen phase φ characterizes the ground state degeneracy while its distortions form the collective mode. This mode is charged since the increment $\delta\varphi = \pm 2\pi$ adds/ subtracts one CDW period, hence the charge is $\pm 2e$. Then the charge density (per unit length) is $n_c = e\varphi'/\pi$ where $\varphi' = \partial_x\varphi$ is the phase gradient along the chain. We should expect that the charge penetration profile $n_c(x,y)$ in the transverse direction y, which needs to be built-in to adjust to the applied voltage, will result in a pattern formation for the phase. which is a way to preview appearance of topological defects.

Remind that for the superconductivity, with the order parameter $\sim \Delta_{sc}\exp(i\theta)$, the voltage difference enforce the phase θ to rotate in time

$\partial_t\theta = 2eV$, hence the spacio-temporal picture $\chi(t,z)$ of the intrinsic Josephson effect would correspond to the static two dimensional pattern $\rho(x,z)$ for CDWs.

4.2 Experiments with overlap mesa-junctions.

During the last decade, the method of interlayer tunneling (see [58], [18] and references therein) was developed for studies of condensed states of electrons in layered materials like high temperature superconductors (cuprates) and layered magnetic materials (manganites). This method is based on the fact that in a layered crystalline lattice the neighboring elementary conducting planes are well separated, at least with respect to electronic hybridization. It provides a possibility to study electronic condensed states that occur at metallic elementary layers at low temperature by means of the intrinsic interlayer tunneling. Experimentally a transport across the layers is studied at mesa-type structures with small lateral sizes of micron scale; they are often referred also as the stacked structures or overlap junctions. Their depth includes typically only a few tens of elementary tunneling junctions.

Later this method was extended to the study of CDW state in CDW materials [58, 18]. The junction used in the experiment was fabricated by a focused ion beam technique, which permitted to keep all elements of the device as parts of the same single crystal. [1] The experimental setup is shown in figure 4.1. Here and below we use the following notations: x is the chain direction along the junction, its total length is $L = L_x$; y is the transverse direction across the junction of the width L_y, here the voltage $2V$ is applied; z is the silent direction along the junction but perpendicular to chains, and the dislocation lines are lined in this direction, with its length L_z.

The are two important observations:

- Apart from the expected peak at the CDW gap $V_g(T) = 2\Delta$, a much lower sharp threshold voltage $V_t \approx 0.2\Delta$ for the tunneling onset.
- The ratio $V_t(T)/\Delta(T) \approx 0.2$ is temperature independent for all measured CDW states, see Figure 4.2. Hence, V_t is originally related to the

[1] Below we call this type of junctions "the internal junction".

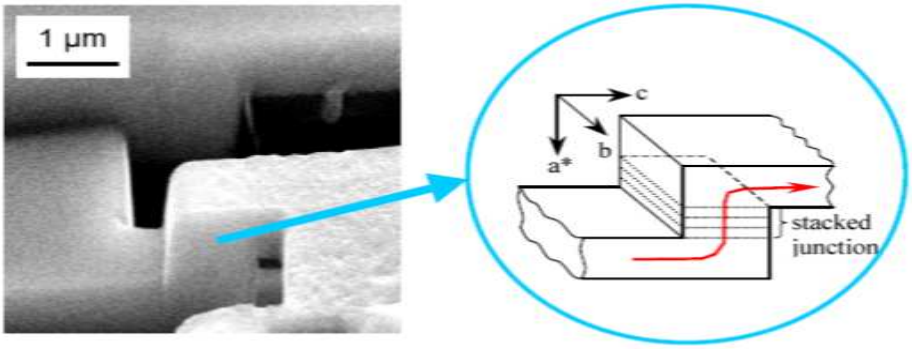

Figure 4.1: Scanning electron microscopy picture of the transverse device (left) and its scheme (right). The stepwise arrowed line shows the currents in the junction area. a^*, b,c are the crystallographic axes of $NbSe_3$; (b,c) is the conducting plane, b is the chain direction. [18]

CDW gap.

- The comparison of the lower threshold voltages V_t's with the 3D ordering scale $k_B T_{CDW}$ of the CDW states indicates a clear linear relation between the two, namely $V_t(0) \approx 1.3 k_B T_{CDW}$. These relations imply that the appearance of the threshold voltage may be accompanied with the phase decoupling of CDWs in adjacent layers which energy might determine the T_{CDW}.

Figure 4.3 shows the fine structure near the treshold in $NbSe_3$ at $T = 130K$. The steps in dI/dV and corresponding sharp peaks in d^2I/dV^2 are distinct. In figures 4.4, a similar structure is reproduced at both positive and negative polarities for the two CDW states in $NbSe_3$. Moreover, figures 4.4 shows that for the normalized V/Δ the peak positions coincide with a remarkable accuracy for both CDW states at different temperatures. The voltages corresponding to these regular peaks in d^2I/dV^2 can be interpreted as the threshold voltage to create successive dislocations in the junction which gives an appealing motivation for the presented theoretical studies.

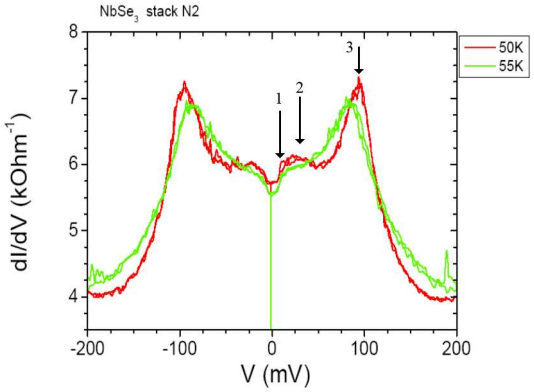

Figure 4.2: Tunneling spectra for $NbSe_3$ at $59K$. Peak 1: absolute threshold at low $V_t = 0.2\Delta$. Peak 2: amplitude soliton at expected $E_{as} = 2/3\Delta$. Peak 3: 2Δ inter-gap $e - h$ pair. [18]

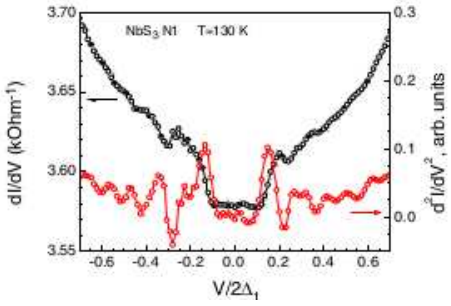

Figure 4.3: dI/dV and its derivative d^2I/dV^2 as a function of the voltage V normalized to the CDW gap, at $T = 130K$. [18]

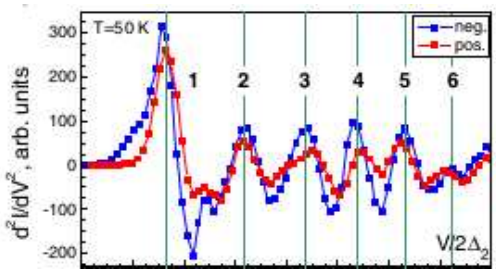

Figure 4.4: Comparison of d^2I/dV^2 for the two voltage polarities for $NbSe_3$ CDW2. [18]

4.3 Floating picture of CDWs' junction

Contrary to semiconductors, in the CDW the excess charge providing the screening of the electric field does not need to come from normal carriers. The screening charge can come directly from the condensate density δn if it is allowed to change from one layer m to another $m+1$: $\delta n \Rightarrow \delta n_m$. (The possibility of local variations along the chain is well known from space resolved X-ray studies [51, 52].) But the difference of δn_m between neighboring layers $m, m\pm 1$ means a difference of their periodicities corresponding to wave numbers $2p_{Fm}$. Hence for the onset of the collective screening the interplane structural correlation must be broken while normally the phases $\varphi(x, r_\perp) = \varphi_m(x)$ on different chains m are correlated. It requires for a critical threshold voltage difference δV_{cr} which depends on the interlayer coupling energy J (per unit length) . By now the degree of the structural anisotropy could be guessed from observations of diffusion sheets or rods in X-ray or neutron scattering. The tunneling experiments allow for the direct determination of J_z as we shall see below.

4.3.1 Fully decoupled regime

To get an idea of major scales, consider first the limit of vanishing interplane coupling J which strictly is realized either above the 3D ordering temperature at $T > T_{3D}$, or practically at high voltage $V \gg V_{cr}$. When neighboring CDWs are well decoupled, they react to the electric potential in the same way as the parent metal - the effect of the sliding mode. Then the screening is instantaneous, practically within one spacing, and $V \approx const$ beyond it. Let d_x, d_y, d_z are the distances between the nearest neighbors along the chain, between planes, and between the chains in the plane, correspondingly; $s = d_y d_z$ is the area per one chain. The concentration n is defined per unit length of one chain, hence the surface and the bulk densities will be n/d_z and $n/(d_y d_z)$.

The full distribution of potentials V_m across the layers is described by the discrete Poisson equation

$$V_{m+1} + V_{m-1} - 2V_m = -4\pi \frac{e^2}{\epsilon_\perp} \frac{\delta n_m}{d_y d_z} d_z^2 = \frac{8}{\epsilon_\perp} \frac{e^2}{\hbar v_F} \frac{d_z}{d_y} V_m. \qquad (4.1)$$

The penetration law is $V_m \sim e^{-\alpha m}$ with α given by

$$\sinh(\frac{\alpha}{2}) = \frac{d_z}{2r_0} = K = \sqrt{\frac{2}{\epsilon_\perp}\frac{e^2}{\hbar v_F}\frac{d_z}{d_y}} \gg 1, \tag{4.2}$$

$$\alpha \approx 2\ln(2K), v_m \sim (2K)^{-2m}. \tag{4.3}$$

the inequality $K > 1$ is natural, with $e^2/(\hbar v_F) \approx 10$ and $d_z \sim d_y$, unless a specially big interlayer permittivity $\epsilon_\perp \gg 1$. Finally it tells us that the layer spacing d_y is bigger than the screening length r_0 of the parent metal. Even for marginal $K \approx 2$, the decrement V_m/V_{m-1} is $\approx 1/20$ which shows that the voltage would drop across only one spacing.

4.3.2 Decoupling threshold: arrays of solitons or dislocations

Discommensurations in a two layers model

The minimal model treats the interlayer decoupling as a kind of the incommensurability effect. It takes into account only two layers 1,2 kept at potentials $\pm V/2$ as described by the following energy functional

$$\int dx \left(\frac{\hbar v_F}{4\pi} \left(\varphi_1'^2 + \varphi_2'^2 \right) + \frac{eV}{2\pi}(\varphi_1' - \varphi_2') - J_y \cos(\varphi_1 - \varphi_2) \right) \tag{4.4}$$

Its minimization allows for the lattice of discommensurations (the solitions in phase difference $\delta\varphi = \varphi_1 - \varphi_2$) which develops starting from the isolated discommensuration. It is the 2π soliton in $\delta\varphi$ with the energy per chain $E_{dc} \sim (\hbar v_F J_y)^{1/2}$. The critical voltage is identified as the energy necessary to create the first discommensuration: $eV_{cr} = E_{dc}$.

At higher $V > V_{cr}$ the solitons form an array and finally they overlap at very high $V \gg V_{cr}$ - the phase difference changes nearly linearly $\varphi_1 - \varphi_2 = 2eVx/(\hbar v_F)$ which means the complete decoupling. This linear increase in space returns us to the Josephson analogy which would show the linear increase in time. The charge redistribution between planes forms the double layer which provides the potential drop.

Consider in details the vicinity of critical voltage for formation of solitonic lattices of interplane discommensurations. For the lattice of discommensu-

rations each element is a straight row in the silent z direction. Discommensurations can be viewed as isolated entities when their width

$$l_{dc} \sim \hbar v_F / E_{dc} \sim (\hbar v_F / J_y)^{1/2}$$

is small in compare to the mean distance $X = 2\pi/\delta\varphi' = 2/\delta n$, that is $l_{dc} \ll X$ hence $(V - V_{cr}) \ll V_{cr}$. In this regime of screening by rare charged strips, the field cannot be confined yet within one spacing: oppositely it will penetrate over the scale of Y (see below) which is large near the critical voltage V_{cr}. Also with charges being concentrated in stripes, local Coulomb interaction becomes very important. Then we find an increase of the discommensuration energy which will redefine the critical energy:$E_{dc} \sim K(\hbar v_F J_y)^{1/2}$, with the same K as in (4.3) coming from Coulomb interactions. All that complicates the tunneling properties and requires for separate studies: e.g. the solitons' cores may be preferable for tunneling because of high local voltages and/or appearance of split-off mid-gap states. The complete insight is possible within the final picture which generalizes the sequence of discommensurations to an array of dislocations.

4.3.3 CDW junction as an array of dislocations

In reality, there is a bulk of many planes with a voltage difference monitored at its sides, while the decoupling will happen somewhere in-between. The former lattice of discommensurations must be generalized to a sequence of dislocation lines. The critical voltage is identified as the DL entry energy, in some analogy to the H_{c1} field in superconductors. If one's sight moves closely above the spacing of decoupled planes, the sequence of dislocation lines will look almost like the solitonic lattice with one charged increment of the phase after another. But when we go away and follow more distant planes, the discommensurations become more and more diffused, that is spread over larger distance, until they overlap to become ill noticed.

Coulomb interaction increases the energy cost to create the dislocation line, but the same time empowers their efficiency in building the potential increases. When the screening carriers vanish at low T, only a few of unscreened dislocation lines over the junction length of $1\mu m$ will be sufficient.

The decoupled spacing is grated, inhomogeneous, the effective thickness of the voltage drop changes along the plane. Near the dislocation line's core, V drops over just the elementary spacing, but between the dislocation lines it takes many planes M, see figure 4.5. Since the tunneling probability falls

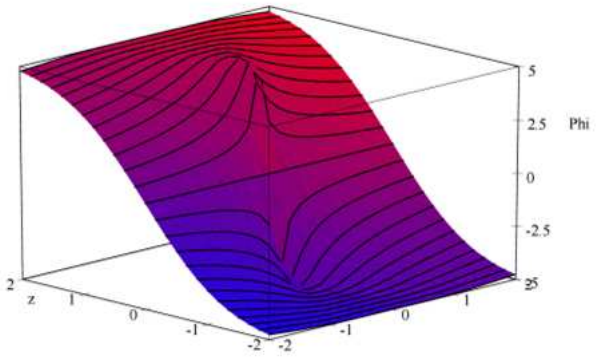

Figure 4.5: Illustration of the voltage drop at the vortex core based upon the analitic solution for a single dislocation. Inside the vortex core, a voltage drop concentrates in one layer, while outside the vortex core the same voltage drop goes smoothly over many layers.

exponentially with the number of planes M, then all tunneling will be concentrated near the dislocation line's core. The voltage drop, and even much more the tunneling, are concentrated near lines within this plane. Then this is the grid of dislocation lines which determines the tunneling. Their growing number will affect the growth of $I(V)$ above the threshold. In ideal case, there may be jumps observed when a new dislocation line is added to the row. (It should be mentioned that hysteresis loop quantization in whiskers of TaS_3 at low T was interpreted as entering of new CDW periods. [59])

There may be more peculiarities related to mid-gap states produced by the dislocation line's cores. Indeed, the phase-only descriptions of dislocation lines resembles the Josephson vortices in layered superconductors, which do not need a normal core. The proliferation of the phase along the dislocation line from an interplane spacing to the next one requires for capturing pairs of electrons or holes. But capturing only one particle advances the DL by half of the period, that is to the conduction plan where the normal core

is necessary. This requirement meets perfectly the CDW property that its state with one unpaired electron is the amplitude soliton where the CDW amplitude passes through zero. The energy of the amplitude soliton, (theoretically $E_{AS} = \frac{2}{\pi}\Delta$) must be paid for proliferating of an elementary segment of the dislocation line which can be one of observed tunneling features [58] (the second peak in figure 4.2). Next, the amplitude deformation creates the mid-gap state, accommodating the unpaired electron, which can add a new spectroscopic feature (E_{AS} instead of $2E_{AS}$) to the tunneling characteristics (STM experiment has observed this AS image [17]).

From the discrete to the continous models: discommensurations versus dislocations

The above model of two planes was only a transparent illustration of decoupling under the applied voltage. Actually, the decoupled planes are the boundaries for two semi-volumes $y \lessgtr 0$ with the voltage $\pm\frac{V}{2}$ applied at distant outer boundaries staying which sometimes can be considered as $y \to \pm\infty$. Perturbations from discommensurations at $y = 0$ will penetrate deeply in the volume creating shear strains, proliferating charges, changing the threshold voltage, etc. Fortunately we have a possibility to keep track of most of that: it it the notion of dislocations and their arrays. Remind that the dislocation line in the CDW is a topological defect such that going around it we acquire or lose one period - for the CDW it is the phase difference $\delta\varphi = \pm 2\pi$ [45]. In our case, it is a dislocation line lying along the z direction in the bridge plan (x, y) at a certain depth which we will usually put at $y = 0$. Comparing some two paths along x, one above: $y > 0$ and another below: $y < 0$ by passing the dislocation line, we should recover this phase increment. More specifically, far from the boundaries the phase will be antisymmetric that is $\pm\pi$ will be acquired independent on the distance from the dislocation line in a similarity to the simple soliton of the two planes model. Instead of the two planes interaction, we shall have the distributed shear energy

$$-\int dx J_y \cos(\varphi_1 - \varphi_2) \Rightarrow \frac{\hbar v_F}{4\pi}\beta^2 \int dxdy(\partial_y\varphi)^2,\ \beta^2 \sim \frac{J_y d_y^2}{\hbar v_F} \ll 1, \quad (4.5)$$

Here β is the dimensionless anisotropy parameter.

With no screening from normal carriers, all variations in x direction of chains, being charged, become particularly costly in the Coulomb energy. These variations must be very slow in compare to variations in the interchain direction y. Hence, the deformations and electric field are concentrated over characteristic lengths Y and X thus forming a long (over the whole length L_z in z direction) thin ($Y \ll X$) stripe. Since, by definition of the dislocation line, the phase changes by π, going along x axis at any level y, then the charge of the stripe is $Q = eYL_y/s$; - its capacitance is the one of a plane condenser: L_zX/Y. Then the Coulomb energy is

$$W_{coul} \sim \frac{(eYL_z/s)^2}{L_zX/Y} \sim \frac{\hbar v_F}{r_0^2}\frac{L_zY^3}{Xs} \tag{4.6}$$

which must be augmented by the shear energy

$$W_{shear} = L_z\frac{\hbar v_F}{d_yd_z}\frac{\beta^2}{4\pi}\int dxdy(\partial_y\varphi)^2 \sim \hbar v_F\beta^2 L_zX/Ys \tag{4.7}$$

Notice that the usual compression energy

$$\frac{L_z\hbar v_F}{4\pi d_yd_z}\int dxdy(\partial_x\varphi)^2 \sim \frac{L_zY\hbar v_F}{X}$$

is negligibly small in comparison with the Coulomb one. From the minimization of the total energy

$$W_{tot} = W_{coul} + W_{shear}$$

over the scale X at a given scale Y.

We obtain

$$X = \frac{Y^2}{d},\ W_{tot} = \mu_0 M,\ \mu_0 = 2\beta\hbar v_F = \frac{\pi}{2}\beta\omega_p\,\omega_p = v_F/r_0,\ d = \beta r_0. \tag{4.8}$$

Here $M = YL_z/s$ is the number of chains crossing the path of the DL while it was submerging to the depth Y ($M = 10$ to 15 in our case.)

These simple estimations recover the scales μ_0, d and the parabolic shape $X \sim Y^2/d$. More precisely the last property is expressed by the factor $\exp(-y^2/(2d|x|))$ (similar expression is obtained in section 3.3.1) which governs distributions for gradients of the phase and the potential. The appearing new length scale is very small $d \sim 1$Å.

Naturally we recover the dislocation line definition, namely, that the total phase increments along x at any depth y and vice versa are

$$\varphi(+\infty, y) - \varphi(-\infty, y) = \pi sign(y) \tag{4.9}$$

$$\varphi(x, +\infty) - \varphi(x, -\infty) = \pi sign(x). \tag{4.10}$$

Next important feature is that the potential follows the phase (up to the sign) as $\Phi = \pm\varphi\beta\omega_p/2$. It gives us asymptotic values $\pm\mu_0$ of the potential Φ at large distances:

$$\Phi(x, \pm\infty) = \mp\mu_0,\ \Phi(\pm\infty, y) = 0,\ \Phi(0, y) = -\mu_0 sign(y). \tag{4.11}$$

We see that the single dislocation provides a finite increment $2\mu_0$ of the potential. This voltage is gained instantaneously, over the single spacing, at the dislocation core, which actually can be quite large. But away from the core the same increment requires for progressively larger width $y \sim \sqrt{dx}$ where Φ changes almost linearly. We can also fix the depth y to see that Φ changes from 0 at $x \to \pm\infty$ to $\pm\mu_0$ at $x = 0$ for any $y \lesseqgtr 0$; this bump at the line $x = 0$ is distributed over $x \sim y^2/d$.

Notice that the enhanced anisotropy changes our view of the device geometry: what could be drawn as a thin junction with $D/L \sim 10^{-2}$, effectively becomes quite thick, $D \gg \sqrt{dL}$. This condition is satisfied as 5 to 1, for the typical geometry with $D = 500$Å and $L = 10^4$Å at $d = 1$Å.

The introduction of the very first dislocation line compensates for the finite voltage across the bridge which we can identify with the critical voltage $V_{cr} = 2\mu_0$. In ideal case, adding any new dislocation increases the voltage by the same amount which would originate a step-wise dependence $I(V)$. The actual dependence will be smooth if we take into account the progressive proliferation of the DL from the outer boundary. Indeed, while the proliferation of a new DL is still shallow, $Y \ll \sqrt{dL}$, its potential reaches the nominal value μ_0 only within the interval $x \ll Y^2/d \ll L$ beyond which, at $x \gg Y^2/d$, the potential falls off, but very slowly, as $\Phi \sim \mu_0 Y/\sqrt{dx}$. The mean value is accumulated mostly over this tail: $< \Phi > \sim \mu_0 Y/\sqrt{dL}$ which increases with Y until the saturation. We see that even a weakly submerged dislocation line exhorts its influence over the whole length L, supposing all distances are below the screening length.

Give some more information, most important for tunneling, on the potential distribution for the array of N dislocation lines. When we are not particularly close to any of the dislocation lines, their potentials are well averaged and give us almost the linear variation of the Coulomb potential $\Phi(y)$ within the layer $Y = \sqrt{dL} \ll D$ where the increment $\Delta\Phi = 2\mu_0 N$ is gained. Φ stays constant beyond this layer. But coming closer to one of the dislocation lines we recover an elementary jump $\Delta\Phi_0 = 2\mu_0$ which is concentrated in a very narrow region, within the single spacing $y_{core} \sim d_y$ if we come as close as $|x| \sim x_{core} \sim d_y^2/d$ which is still a rather wide spot. Only near the dislocation line core the potential changes between planes fast enough to provide an efficient tunneling. Just here the most efficient tunneling takes place (away, the tunneling must proceed through the number $y/d_y \sim \sqrt{x/x_{core}}$ of stacks). The nearest layers become completely decoupled, and open for tunneling along the whole area, when the dislocation line spacing falls below the core size, $X \ll x_{core}$, that is at the decoupling voltage $V >> \mu_0$. This is an analogy of the H_{c2} field in superconductors.

In the following chapters we shall see to which extend our modeling confirms or complicates the outlined above anticipated picture.

Chapter 5

Simplified model for CDW vortex state reconstruction.

5.1 Model description

The motivation of studies presented below comes from the tunneling experiments (see chapter 4). In this chapter we consider a simplified model to study the CDW vortex states in the internal junction under applied static electric fields. The model takes into account the complex order parameter of the CDW and the electric potential. We consider the CDW on a weakly correlated chain material, in a a simple rectangle 2D geometry with the coordinate x in the chain direction and y in the perpendicular one. The CDW is described by the complex order parameter $\Psi = A\exp(i\varphi)$. The voltage is applied across the CDW chain in y direction see figure 5.1. The applied

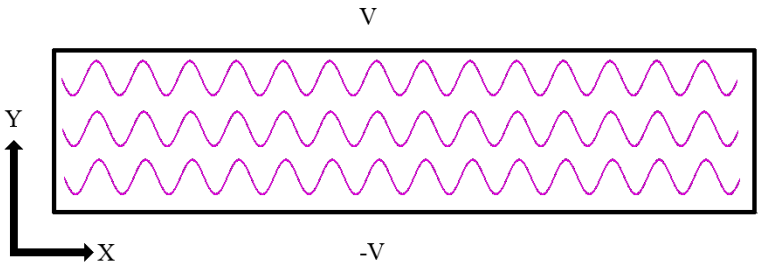

Figure 5.1: The geometry for the modeling. x, y are the axes along or across the CDW chains.

voltage gives rise to a profile of the electric potential Φ and the electric filed $E = -\nabla\Phi$. For simplicity it is the open circuit model, when no normal currents are allowed. With minimal but essential ingredients in the theory, we are able to show the important features predicted in the theory, such as the appearance of the threshold voltages for the creation of vortices, the tendency of vortex number increasing with the applied voltage.

There are two possible approaches to treat the model. The first one is the method of the minimization of the total energy. This method allows to obtain only the static configurations in the final stationary states without the information of the intermediate steps. The second approach is based on the solving the extremal equations rather than energy minimization. In addition to the static final configurations, this approach reveals also dynamic features of the vortex formation.

5.2 Method of minimization of the total energy

In this section, we will show how the vortex state in the CDW is achieved by applying the minimization method on the Landau free energy functional of the system [1].

The deformation of the complex order parameter originate the variation of the CDW charge density in the bulk $\rho_{CDW} = \frac{e}{\pi}A^2\frac{\partial\varphi}{\partial x}$. The surface charge density is $E_n/4\pi$, where E_n is the normal component of the electric field at the surface of the sample. The circuit is open - no normal current allowed. Then the problem is static, so the energy minimization can be applied. The stationary state of the system is determined by the minimum of the total energy functional W

$$W = \int_\Omega L(\Psi,\Phi)dxdy + \frac{1}{4\pi}\int_S E_n\Phi ds, \tag{5.1}$$

where the integrations go over the bulk Ω or the surface S of the stack. The CDW energy density L coming from a Landau expansion of the free energy

[1] These studies originate from the PhD work of Alvaro Rojo Bravo.

functional in terms of the complex order parameter has the form:

$$L(\Psi,\Phi) = -a_1|\Psi|^2 + a_2|\Psi|^4 + a_3\left((\partial_x\Psi)^2 + \beta\,(\partial_y\Psi)^2\right) + a_4\rho\Phi - a_5|\nabla\Phi|^2. \quad (5.2)$$

The coefficient $\beta < 1$ indicates the strength of the interchain coupling, and it characterizes the elastic anisotropy of the CDW. a_1 and a_2 are the phenomenological coefficients, depending on the temperature T. $a_3 = \hbar v_F/4\pi s$, where v_F is the Fermi velocity of the electrons, and s is the area per chain. $a_4 = 1/s$. $a_5 = \epsilon/4\pi$, with ϵ being the dielectric constant of the host crystal. In the following, we discuss the results obtained from the simulation.

5.2.1 Summary of results

At voltage V below the threshold, the CDW stays homogeneous in space; the complex order parameter is constant; the electric potential is constant in x direction and interpolates linearly between $V/2$ and $-V/2$ in y direction. When V passes a critical value, a grid of dislocation is created, see figure 5.2. With a further increase of V, the number of dislocations increases sequentially and the dislocations enter the sample by pairs. The presence of dislocation lines can be seen by plotting the phase of complex order parameter. The 2π jumps of the phase are artifact of its definition as a single value function. They are not the physical singularities. Figures 5.3 and 5.4 show that the amplitude A of the complex order parameter is zero at the dislocation core as it should be for a vortex, as we have already anticipated in chapter 3.

Under the applied electric field, the electric potential becomes inhomogeneous in both x and y directions, figures 5.5, 5.6. The voltage drop concentrates near the dislocation cores, which serve as tunneling junctions.

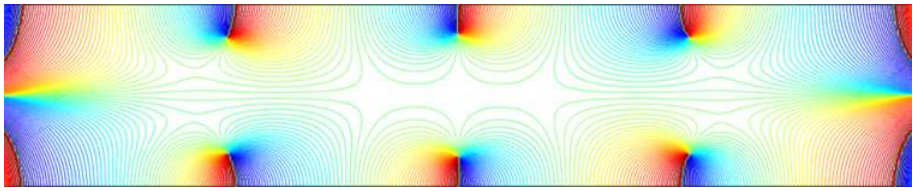

Figure 5.2: Phase of the complex order parameter at V slightly below the threshold voltage. [60]

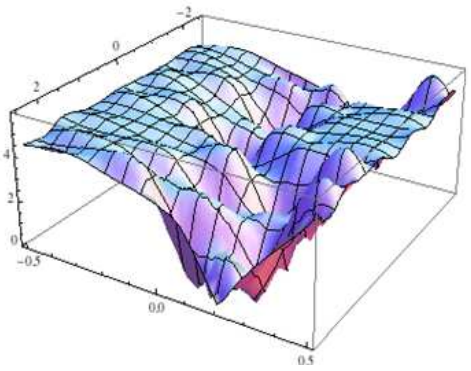

Figure 5.3: Amplitude of complex order parameter at V slightly below the threshold voltage. [60]

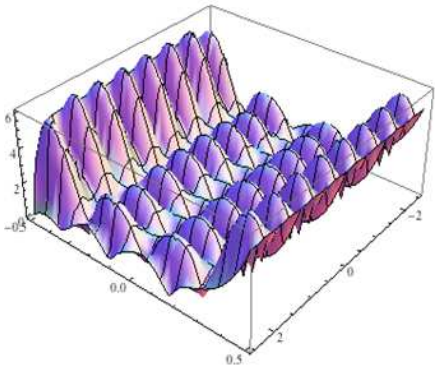

Figure 5.4: Amplitude of the complex order parameter at V well below the threshold voltage. [60]

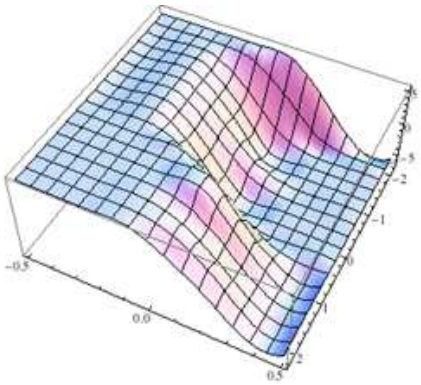

Figure 5.5: Distribution of the electric potential at V slightly below the threshold voltage. [60]

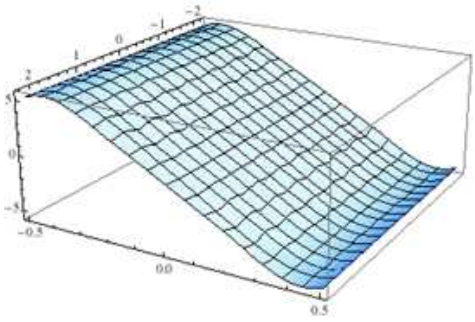

Figure 5.6: Distribution of the electric potential at V well below the threshold voltage. [60]

This modeling confirms qualitatively and illustrates the conjectures derived from tunneling experiments performed upon the overlap junctions [18]. But it does not allow the access to the dynamic processes. In the next chapter, we will present variational method taking into account the multifield interaction, and this method also allows the exploration of the dynamics of the system.

5.3 Variational approach to the charge density wave vortex state

The problem studied here is similar to the one in section 5.2, but we adopt a minimal Ginzburg-Landau approach to resolve it. .

The total Hamiltonian of the system H_{tot} can be written in two parts, the CDW part H_{CDW} and the electric part H_{el}. H_{CDW} is written as a Ginsburg-Landau form with the BCS-improved potential energy, and it is given as

$$H_{CDW} = \frac{\hbar v_F}{4\pi s}\int dr^3\Big((\partial_x A)^2 + A^2(\partial_x\varphi)^2 + \beta^2(\partial_y A)^2 + A^2\beta^2(\partial_y\varphi)^2 + \frac{2\pi}{\xi^2}A^2\left(\log\frac{A^2}{\mathbf{e}}\right)\Big). \tag{5.3}$$

In H_{CDW}, the phase φ is considered simply as an elastic field with $\partial_x\varphi$ associated with the compression or dilatation energy and $\partial_y\varphi$ the shear energy. The variation of the amplitude A taken into the Hamiltonian is a crucial point for the creation of vortices. The last term is the ground state energy of CDW, and with it minimum at $A = 1$, it measures the energy payed for the system to get out of its ground state. ξ is the coherence length, with the relation $\Delta\xi = \hbar v_F$, and β is the anisotropic parameter. H_{el} deals with the electric field and its reaction with the CDW, and it is given as

$$H_{el} = \frac{1}{s}\int dr^3\left(\frac{1}{\pi}\Phi A^2\partial_x\varphi - \frac{4r_0^2}{\xi\Delta}(\nabla\Phi)^2\right). \tag{5.4}$$

In H_{el}, the first term describes the interaction of the condensed charge density with the electric field Φ. The second term is the electric potential energy. Here and after the electron charge e is absorbed into the electric field Φ. r_0 is Debye screening length.

We make variations of the total Hamiltonian H_{tot} with respect to the three independent field variables A, φ, and Φ, and obtain a three-equation system,

$$-\partial_x^2 A + A\left(\partial_x \varphi\right)^2 - \beta^2 \partial_y^2 A + \beta^2 A\left(\partial_y \varphi\right)^2 + \frac{2\pi}{\xi^2} A \log A^2 + \frac{4}{\xi}\frac{\Phi}{\Delta} A \partial_x \varphi = 0, \quad (5.5)$$

$$-\partial_x\left(A^2 \partial_x \varphi\right) - \beta^2 \partial_y\left(A^2 \partial_y \varphi\right) - \frac{2}{\Delta\xi}\partial_x\left(A^2 \Phi\right) = -\gamma_\varphi A^2 \partial_t \varphi, \quad (5.6)$$

$$\frac{1}{\pi} A^2 \partial_x \varphi + \frac{8 r_0^2}{\Delta\xi} \nabla^2 \Phi = 0, \quad (5.7)$$

γ_φ is the damping coefficient for the phase, and it is related to the experimental value as

$$\gamma_\varphi = \frac{\Delta\xi}{4\pi s r_0^2}\frac{1}{\sigma_{CDW}}. \quad (5.8)$$

The value of the parameters is listed below To accelerate the convergence

$\varepsilon_F = 6meV$	$\Delta = 25meV$
$\xi = 8nm$	$r_0 = 0.6nm$
$\varepsilon \sim 10$	$\sigma_{CDW} = 1000\Omega^{-1}m^{-1}$ or$10^{13}s^{-1}$

Table 5.1: Parameters used in the simulation.

of the calculation, an exponential time scale is adopted. The real time $t = 10^\tau/\sigma_{CDW}$, where τ is the display time above the images.

5.3.1 Results of simulations

The threshold voltage found in the simulation is 0.2Δ. At this voltage a pair of vortices is created in the sample, see figure 5.7.

More pairs of vortices appear at the applied voltage takes the increasing values, 0.4Δ, 0.76Δ, and 0.8Δ, see figure 5.8.

The results for the electric potential Φ are showed below.

At the beginning of the evolution, the vortices serve to screen the electric potential. In figure 5.9, the electric potential is screened out at the two sides of the sample, where two pairs of vortex are well formed. The electric potential decreases almost linearly in the middle of the sample, for no vortex is created there.

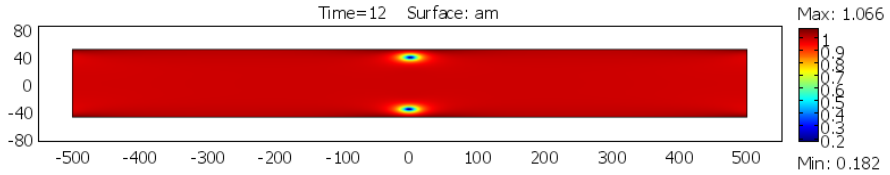

Figure 5.7: Formation of vortex pair. A pair of vortices is created with at $V = 0.2\Delta$.

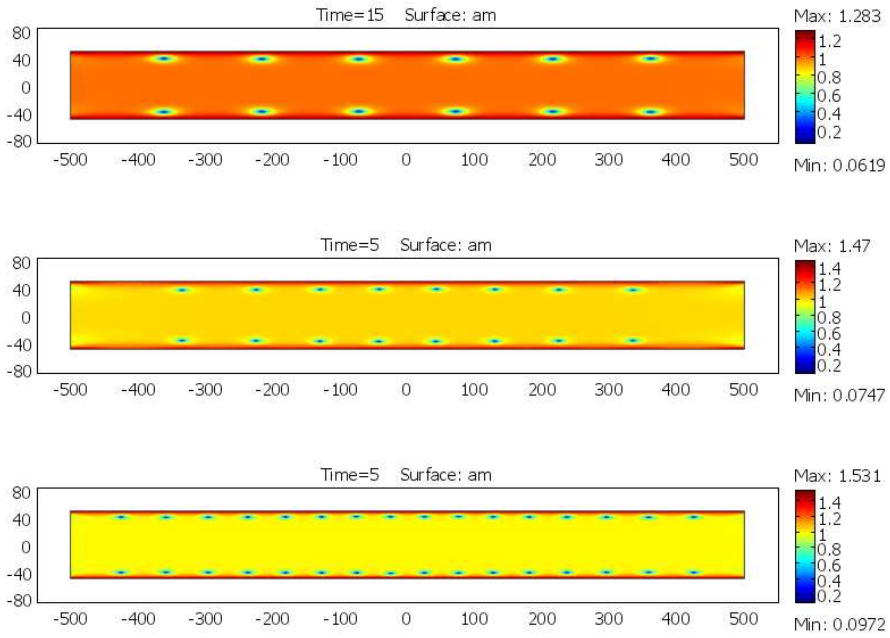

Figure 5.8: Formation of vortex pair at different voltages. The number of vortex pairs increases with the potential V. $V = 0.4\Delta$, $V = 0.76\Delta$, $V = 0.8\Delta$ (from top to below).

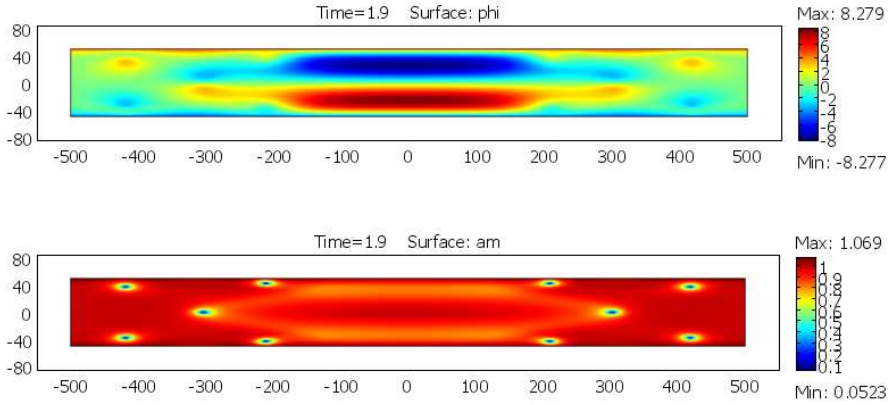

Figure 5.9: The distribution of the electric potential (phi) and the corresponding CDW amplitude configuration (am) during the evolution. The real time $t \sim 7.10^{-13}s$.

At the stable stage, the vortices work as the tunneling junctions, where the voltage drop is concentrated. In figure 5.10, the voltage drop happen mainly at the core of each vortex .

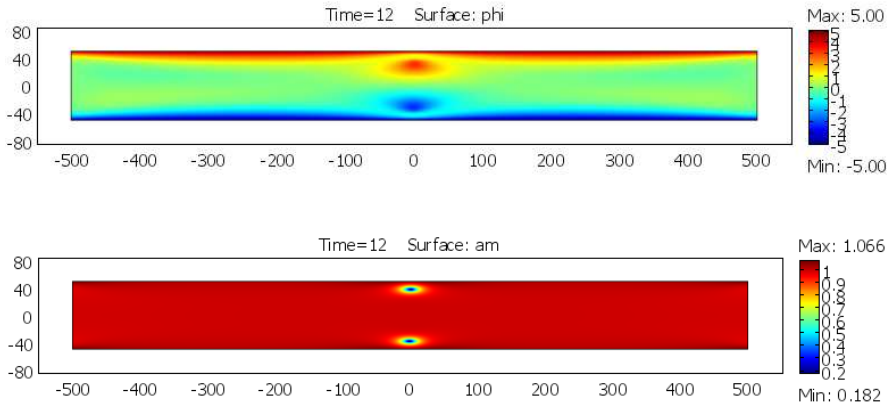

Figure 5.10: The distribution of the electric potential (phi) and the corresponding CDW amplitude configuration (am) at the final stable state. The real time $t \sim 2.10^{-8}s$.

Triangular lattice versus rectangular one

A triangular lattice of vortices is created during the evolution as an intermediate state (figure 5.11 top) at $t = 2.10^{-12}s$. However, at the final stable state at $t = 3.10^{-7}s$ a rectangular lattice is formed (figure 5.11 bottom) . From this simulation, we may say that the formation of a rectangular lattice is energetically favorable with respect to the formation of a triangular one.

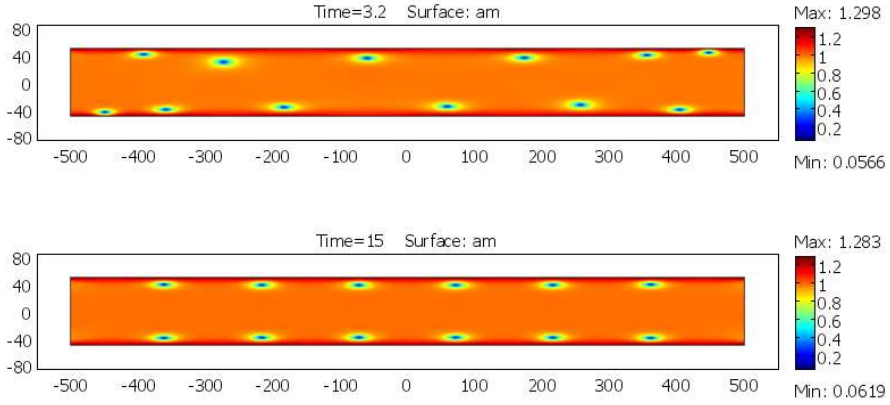

Figure 5.11: Triangular lattice versus rectangular one

Total energy

A variation procedure upon the free energy is equivalent to finding the minimum of the total free energy and we can see in figure 5.12 that the total free energy of the system, expressed as the integration of the local energy density, decreases with the time steps in the simulation. This decrease signifies that the system is driven to its stable state at it lowest energy by the dissipative force.

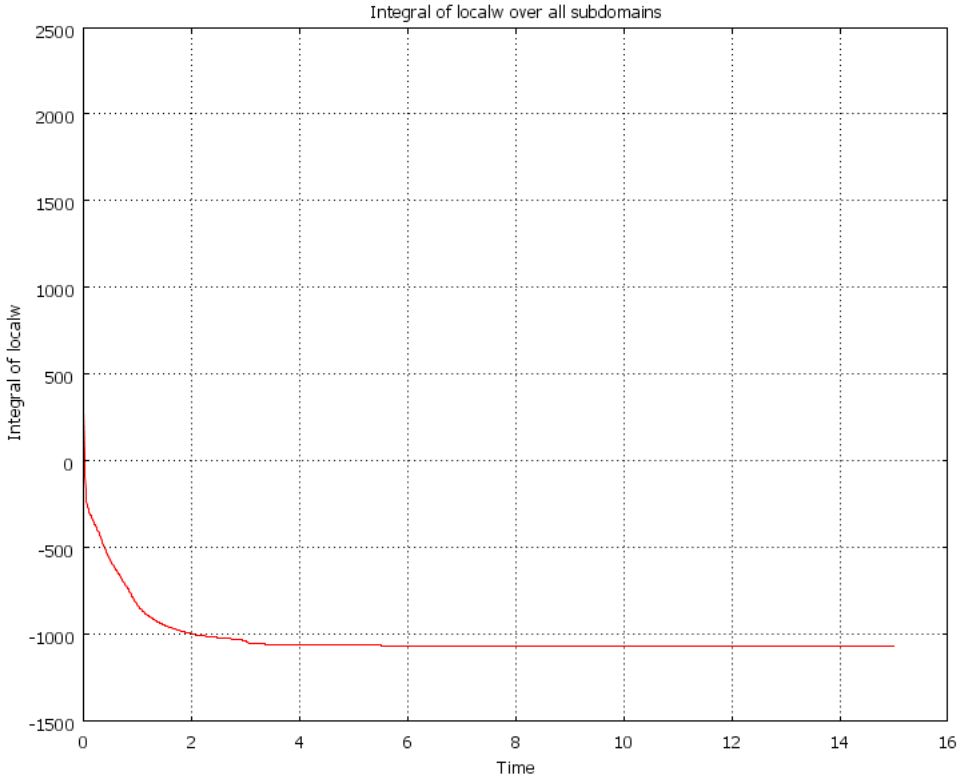

Figure 5.12: Total free energy in time steps of calculation.

Chapter 6

Charge density wave vortex state reconstruction

6.1 Introduction

In this chapter, we present our main detailed results on the numerical modeling. We study the reconstruction of the CDW state under the applied transverse voltage or in the internal (mesa) junction as defined in Ch. 4 which also reviewed the experimental motivation. [1]

We take into account multiple fields in mutual nonlinear interactions: the phase φ and the amplitude A of the CDW order parameter, distributions of the electric field, of the density and the current of various normal carriers. The time-evolution equations were solved numerically for a restricted geometry in two spatial dimensions. The numerical work was performed for parameters close to experiments on $NbSe_3$ [18]. The simulations were performed by the finite element method implemented via the program COMSOL Multiphysics.

The simulations give access to the dynamical behavior of the vortices penetrating into the CDW and illustrate their final pattern formation. The vortices are created in the junction when the voltage across, or the current

[1] Recall, we use the name "internal junction" underlying that the whole device - leads to the source and the drain, and the tunneling bridge are curved from one peace of a single crystal, see the Figure 4.1 in chapter 4.

through, exceed a threshold. The final number of vortices in the reconstructed ground state increases stepwise - in agreement with experiments. The vortex core concentrates the voltage drop across the junction which can give rise to observed peaks of the inter-layer tunneling. Remarkably, the number of vortices created in the transient process is much bigger than the remnant one in the equilibrium.

6.2 Model

We use the time-dependent dissipative Ginzburg-Landau approach to describe the dynamics of the CDW system. The static state is determined by a minimum of the total energy functional $H_{total} = H_{CDW}(\Psi) + H_{el}(\Phi, \Psi, n)$. The CDW free energy H_{CDW} can be written as (see equation 5.3)

$$H_{CDW} = \int dr^3 \left\{ \frac{\Delta\xi}{4\pi s} \left(|\partial_x \Psi|^2 + \beta^2 |\partial_y \Psi|^2 \right) + \frac{\Delta}{2\xi s} |\Psi|^2 \ln\left(\frac{|\Psi|^2}{e} \right) \right\}. \quad (6.1)$$

Here $\Psi = A\exp(i\varphi)$ is the CDW complex order parameter, and its amplitude A is normalized to 1 at equilibrium, i.e. $A = \Delta/\Delta_{eq}(T)$. The first two terms give the energy of elastic deformations: compression and the shear; the parameter of the structural anisotropy $\beta^2 \sim 0.1 - 0.01$ characterizes the elastic anisotropy of the CDW. The third term is the CDW ground state energy, with a minimum at $|\Psi| = 1$ see figure 6.1.

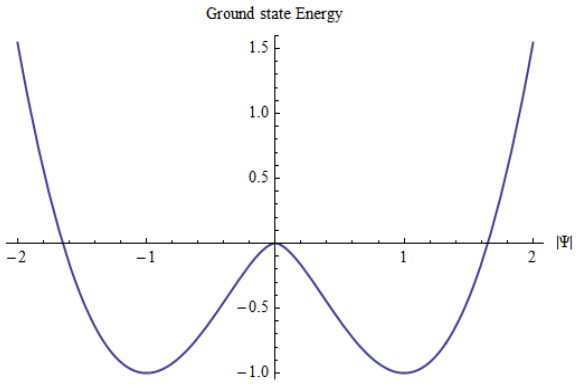

Figure 6.1: The ground state energy of the CDW as a function of A, with the minimum at $A = 1$, which stabilizes the CDW ground state.

The model also takes into account the Coulomb interactions, which become very important since CDW deformations are charged and charges are particularly concentrated near the vortices cores. H_{el} describes the effect of the local electric field, and of free carriers:

$$H_{el} = \int dr^3 \left(\frac{1}{s\pi} \Phi A^2 \partial_x \varphi + \Phi \frac{n(\zeta) - \bar{n}}{d_z} - \frac{\varepsilon}{8\pi} |\nabla \Phi|^2 + F(n) \right) \tag{6.2}$$

Here the potential Φ is assumed to incorporate the one-electron charge value $e > 0$, d_z is the inter-plane distance and $\varepsilon \sim 10$ is the host dielectric constant. $n(\zeta, T)$ is the local normal carrier density per area in the single x, y plane, $\bar{n}(T) = n(0, T)$ is the mean one, and $n_0 = \bar{n}(0)$ is the value at $T = 0$. The first and the second terms in (6.2) give the interaction of the collective and the normal charges with the electric field, and the third term is the electric field energy. The last term $F(n)$ is the free energy density of the normal carriers giving the definition of the local chemical potential $\zeta = \partial F / \partial n$. We shall assume, for the specificity and in realities of the $NbSe_3$, that normal carriers come from a small electron pocket with a 2D elliptic dispersion in the x, y plane; then

$$n(\zeta) = n_0 \frac{T}{\varepsilon_F} \ln(1 + \exp(\frac{\varepsilon_F + \zeta}{T})), \tag{6.3}$$

where ε_F is the pocket Fermi energy.

The system evolution is governed by dissipative equations:

$$-\gamma_A \frac{\partial A}{\partial t} = \frac{\delta H_{total}}{\delta A}, \tag{6.4a}$$

$$-\gamma_\varphi A^2 \frac{\partial \varphi}{\partial t} = \frac{\delta H_{total}}{\delta \varphi}, \tag{6.4b}$$

$$\frac{\delta H_{total}}{\delta \Phi} = 0. \tag{6.4c}$$

Here $\gamma_{A,\varphi}$ are the damping coefficients. γ_φ can be related to the experimentally observed value of the collective conductivity σ_{CDW}:

$$\gamma_\varphi = \frac{\Delta \xi}{4\pi s r_0^2} \frac{1}{\sigma_{CDW}}, \tag{6.5}$$

and $\sigma_{CDW} \sim 1000 \Omega^{-1} m^{-1}$ (or $10^{13} s^{-1}$ as used in our equations) from experimental results. From equations (6.4a, 6.4b), also see the section 6.5, the

relaxation time for the amplitude A is $t_A = \left(\frac{\xi}{r_0}\right)^2 \frac{1}{\sigma_{CDW}} \sim 2.10^{-11} s$ - a time scale, which is at the margin of the credibility of the dissipative Ginzburg-Landau theory. The relaxation time for the phase is always longer than that for the amplitude, such that $t_\varphi = \left(\frac{L_x, L_y/\beta}{r_0}\right)^2 t_A \sim 10^1 t_A$ to $10^6 t_A$ which gives $\sim 10^{-10}$ to $\sim 10^{-5} s$, depending on the length scale under consideration, (L_x and L_y are the characteristic lengths for the processes, varying from the vortex size to the sample size). For this reason, we can approximately put $\gamma_A \approx 0$, so that the energy is locally and instantaneously minimal with respect to A. The arguments above can also justify our choice of the final time $t_f = 10^8 \times 1/\sigma_{CDW} = 10^{-5} s$ as the stationary time for all the variables.

Equations (6.4) can be developed in the following form,

$$-\gamma_A \frac{\partial A}{\partial t} = \frac{\Delta\xi}{2\pi s}\left(-\hat{\nabla}^2 A + A\left(\hat{\nabla}\varphi\right)^2\right) + \frac{\Delta}{\xi s} A \ln\left(A^2\right) + \frac{2\Phi A}{s\pi}\frac{\partial\varphi}{\partial x}, \quad (6.6a)$$

$$-\gamma_\varphi A^2 \frac{\partial\varphi}{\partial t} = \frac{\Delta\xi}{2\pi s}\hat{\nabla}\cdot\left(A^2\hat{\nabla}\varphi\right) + \frac{1}{s\pi}\frac{\partial}{\partial x}\left(A^2\Phi\right), \quad (6.6b)$$

and the Poisson equation for Φ,

$$\frac{\varepsilon}{4\pi}\nabla^2\Phi = -\frac{A^2}{\pi s}\frac{\partial\varphi}{\partial x} - \frac{1}{d_z}\left(n(\zeta) - \bar{n}\right). \quad (6.6c)$$

The equations (6.6) are completed by the diffusion equation for normal carriers:

$$\frac{\partial n}{\partial t} + \nabla j = \frac{\partial n}{\partial t} - \nabla(\hat{\sigma}\nabla(\zeta + \Phi)) = 0, \quad (6.7)$$

Here $\hat{\nabla} = \partial_x + \beta^2\partial_y$ is the anisotropic partial differential operator, and $\hat{\sigma} = (\sigma_x, \sigma_y)$ is the anisotropic conductivity; it will be taken to be proportional to the carriers' concentration, that is given by mobilities in each direction.

The boundary conditions reflect the following properties:

1. The normal stress vanishes at all boundaries

$$\left(\frac{\Delta\xi}{2}A^2\hat{\nabla}\varphi - A^2\Phi\vec{x}\right)\cdot\vec{\nu} = 0; \hat{\nabla}A\cdot\vec{\nu} = 0. \quad (6.8)$$

2. Normal electric field is zero at all boundaries providing the total electroneutrality and the confinement of the electric field within the sample:

$$\nabla\Phi\cdot\vec{\nu} = 0. \quad (6.9)$$

3. No normal current flow through the boundaries: $-\hat{\sigma}\frac{n}{n_0}\nabla(\zeta+\Phi)=0$, except for the two source/drain boundaries left for the applied voltage $\pm V$, where the electro-chemical potentials are fixed: $\mu=\zeta+\Phi=\pm V$.

In the above equations $\vec{x}$ is the unit vector along the chain axis, $\vec{\nu}$ is the outward unit normal vector on the domain.

We use experimentally determined parameters of the material and of its CDW state. When they are not well known, the BCS-kind relations of the Peierls-Fröhlich theory are employed. The following table lists the parameters used in the simulations.

$\varepsilon_F = 6meV$	$\Delta = 25meV$	$k_BT = 5meV$
$\xi = 8nm$	$r_0 = 0.6nm$	$d_z = 1.5nm$
$l_{scr} = 1.62nm$	$n_0 = 3.4 \cdot 10^{-3}nm^{-2}$	$\varepsilon \sim 10$
$\sigma_{CDW} = 1000\Omega^{-1}m^{-1}$ or$10^{13}s^{-1}$	$\sigma_x = 100\sigma_{CDW}$	$\sigma_y = 0.01\sigma_{CDW}$

Table 6.1: Parameters used in the simulation.

In the following, the time unit will be in $1/\sigma_{CDW} = 10^{-13}s$ and sizes will be given in nm.

6.3 Results and discussion

6.3.1 Geometry description of the problem

The real geometry of the junction used in experiment [18] is given in figure 6.2, which is characterized by two overlapping slits across the sample (experimentally they are the cuts made by the focused ion beam technique). The left and the right boundaries are the terminals where the voltage is applied. The junction was made with a CDW material possessing a highly anisotropic conductivity, so that normally the current goes along the high conductivity direction X. However, the two slits enforce the current to deviate to the transverse direction Y of high resistivity originating the strong voltage drop at the central rectangular region. The results will be presented here for two different geometries. First results for the oversimplified rectangular geometry, representing the active region of the real geometry are given, which

provides a necessary intuition and also can be applied to other experiments with a simple minded field effect geometry. In the next section we will give the results for the real geometry.

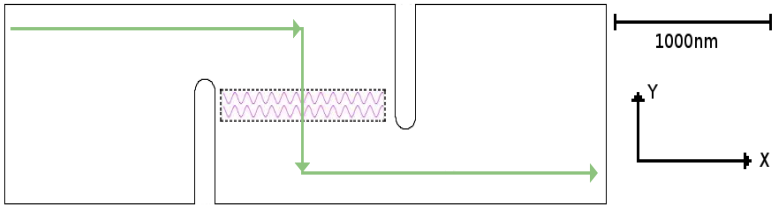

Figure 6.2: The real geometry of the junction, and its active rectangular central part, where stationary vortices will stay. The green arrows indicate the trajectory of current flows.

6.3.2 Results for the rectangular geometry

We present here first the results for the rectangular geometry. This plays an important role to tune the method and to understand the real geometry model. A descriptive introduction of the rectangular case will be given, while more detailed discussions are reserved for the real geometry.

Two regimes of the CDW vortex formation have been observed during the simulation. The transient regime begins at 10^{-11} second to 10^{-8} second, and the quasi-stationary regime from 10^{-8} to 10^{-7} second, when the system relaxes into equilibrium and a true CDW stationary state is achieved.

Two types of dislocations have been revealed by the simulation: the dynamic vortex and the stationary one. The dynamic vortices appear in large numbers at the upper and lower boundaries of the sample in the beginning, see figure 6.3, and during the transient regime they create turbulence in the CDW background. Most of them annihilate with partners of opposite signs or they disappear at the boundaries.

The quasi-stationary vortices are those left after the transient dynamic regime, they move slowly to find their equilibrium position. For the rectangular geometry model and for realistically chosen parameters, we have obtained that the first stationary vortex appears at $V = 0.308\Delta(7.7meV)$. The second stationary vortex appears at $V = 0.328\Delta(8.2meV)$, the third

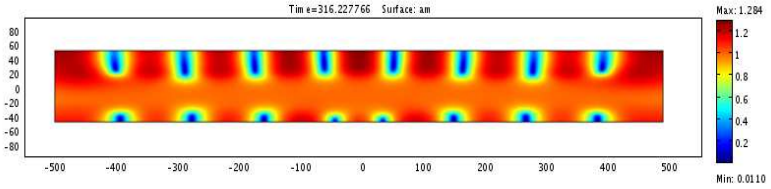

Figure 6.3: Amplitude snapshot at $t = 3*10^{-11}s$. Illustration for appearance of dynamic vortices. They will give rise to turbulence in the transient regime and then evolve into a small number of stationary vortices at final stage. The variation of the color from red to blue corresponds to the range of amplitude from 1 to 0.

one at $V = 0.376\Delta$, and the forth one at $V = 0.568\Delta$ see figure 6.4. The number of the stationary vortices increases with increasing applied voltage.

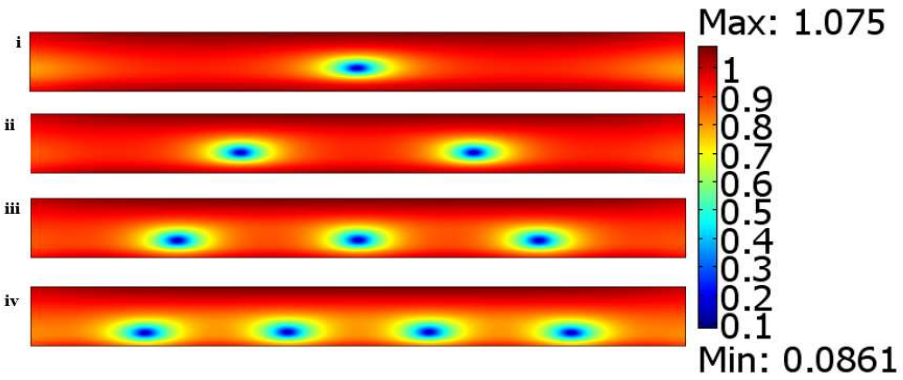

Figure 6.4: Formation of stationary vortices in the rectangular geometry. The number of vortices increases with the applied voltage: $V = 0.308\Delta$(i), 0.328Δ(ii), 0.376Δ(iii), 0.568Δ(iv), respectively.

The CDW amplitude goes to zero at the vortex center as shown by the blue color in figure 6.4. The figure 6.5 shows that the phase rotates by 2π rotation around the point of the zero amplitude thus proving that this is the vortex center.

Distribution of the electric potential Φ at presence of one vortex is shown in figure 6.6. A sharp drop of the potential Φ is observed at the vortex core in accordance with analytic and numeric results for a dislocation in linear approximation for the infinite media see chapter 4. This should increase the

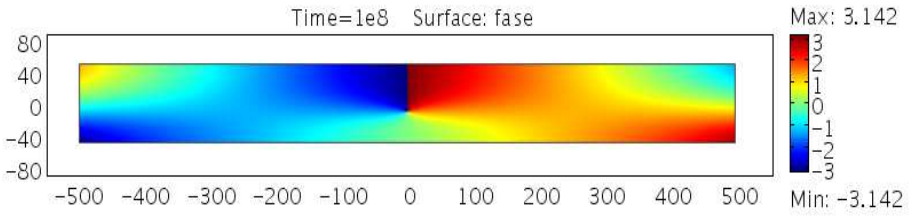

Figure 6.5: Phase of the complex order parameter at the vortex center. The 2π circulation of the phase going around the vortex center. The color map passes from π in red to $-\pi$ in blue.

electrons' tunneling probability near the core, which can explain the peaks in experimental tunneling spectra. Even beyond the tunneling, the presence

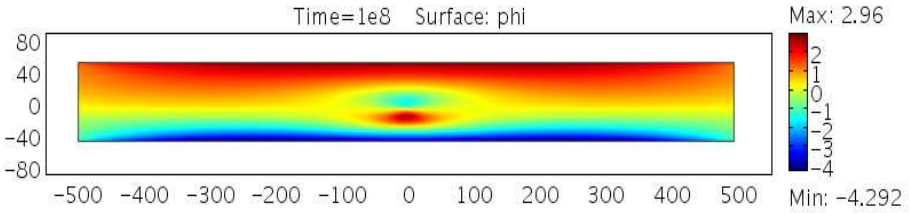

Figure 6.6: Electric potential Φ for the one-vortex state.

of vortices affects the normal current. The corresponding I-V characteristics of the junction are shown in figure 6.7.

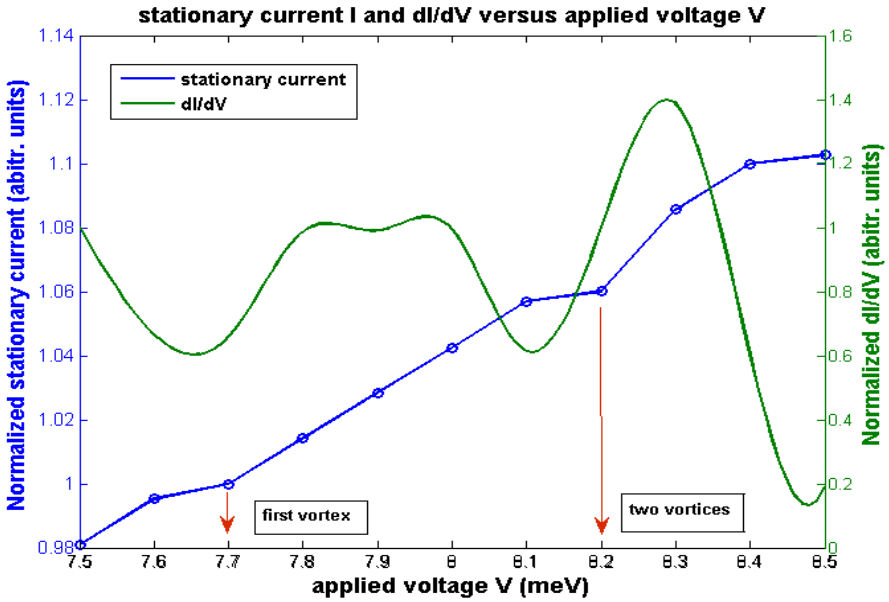

Figure 6.7: Current I and differential conductivity dI/dV versus the applied voltage.

We can obtain different vortex configurations (figures 6.8, and 6.9) by varying the value of the anisotropy parameter β from 0.1 to 0.01. The thresholds found in these situations are of the same order $\sim 10meV$, but the final configurations are different, which signifies a different interaction between the vortices.

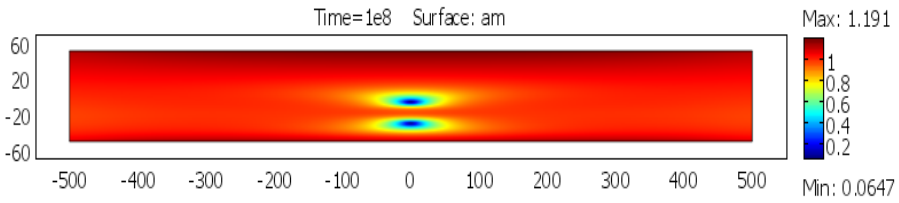

Figure 6.8: Vortex pair is created with $\beta = 0.01$ at $V = 10meV$.

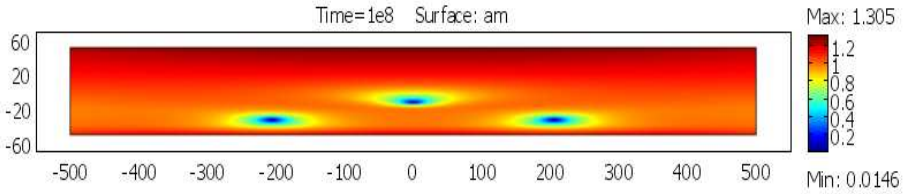

Figure 6.9: Formation of triangular vortex lattice with $\beta = 0.01$ at $V = 15meV$.

6.3.3 Results for real geometry

Now we are armed to go to much more challenging studies in the real geometry. In the bulk of the CDW material we use the same set of equation. Within the slits, only the electric field is present which obeys the Laplace equation. The former no-stress and the new potential matching boundary conditions need to be carefully defined all over the complicated sample boundary.

Figure 6.10 shows the distribution of Φ which would take place if there is no CDW deformation, i.e. the material is a simple conductor with the given conductivities of normal electrons.

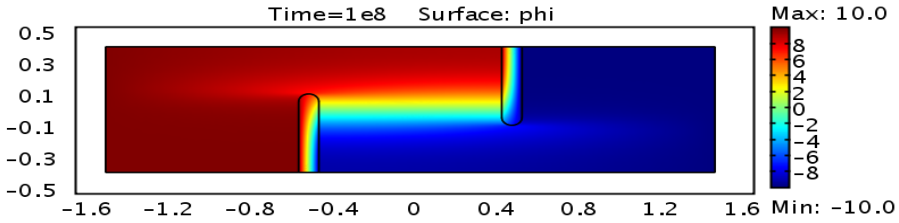

Figure 6.10: Distribution of the electric potential if there is no CDW deformation. The chemical potential is nearly identically $\zeta = 0$, hence there is no charge variations in the bulk. The profile of Φ is created by charges accumulated at the boundaries.

Two regimes of the CDW vortex formation have been observed in the simulations. The initial regime with the characteristic time $10^{-11}s$, (which is at the boundary of our dissipative approximation) is the transient, turbulent one. During this time, the flashes of zero CDW amplitude appear at the boundaries all over the samples and at the slits' tips, evolving into well-structured vortex cores as shown in figures 6.11. Following events of an-

nihilation between two vortices of opposite signs and of destruction of vortices near boundaries are observed. The number of vortices participating in the transient process is much larger than that (one or two) left in the stationary state. In the second, quasi-stationary regime, the remnant vortex or vortices move more slowly to find the equilibrium positions. Finally at $t \sim 10^{-6}$ to $10^{-5}s$ the system relaxes to stationary equilibrium. The evolution time is two order longer in the real geometry model than in the rectangular geometry model, which can be caused by the size effect and the complexity of the geometry. The whole evolution of the system can be seen in movies available at the site [61].

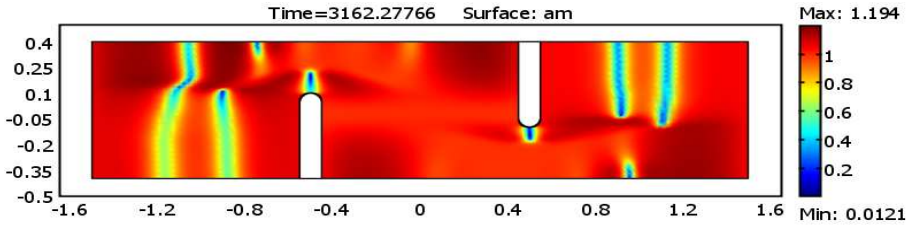

Figure 6.11: Snake traces of suppressed amplitude show a transient state of vortex formation in the junction. The variation of the color from red to blue corresponds to the range of amplitude from 1 to 0.

For the real geometry, we have obtained that the first stationary vortex appears at $V = 0.27\Delta(6.7meV)$, the second one enters at $V = 0.32\Delta(8meV)$, see figure 6.12. In this figure, the CDW amplitude vanishes continuously at the vortex cores (shown in the blue color), while it remains nearly unperturbed and close to its normalized value 1 (in red) for the major part of the junction. The theoretical discussions about the vortex formation in junction have been given in chapter 4.

If the overall sliding of the CDW was allowed, then the conversion between the CDW condensate and the normal electrons could happen at these vortices cores, where the CDW state is destroyed [45]. However, in our simulations, we used the boundary conditions, which do not allow the overall sliding. This is the experimental demand, [58, 18]: the longitudinal normal current was kept below the threshold of depinning, also a lateral injection was used in more sophisticated experiments.

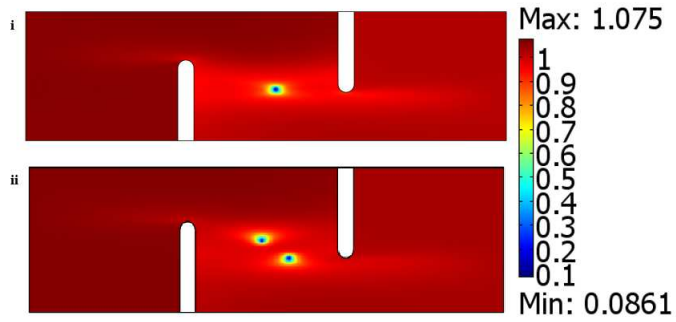

Figure 6.12: Final stationary vortices state. Formation of stationary vortices in the real geometry. The number of vortices increases with the applied voltage: $V = 0.27\Delta$ (i), 0.32Δ (ii), respectively.

The phase winds by 2π around the vortex core as it is seen in figure 6.13. Additionally, there are 2π rotations of the phase around the edges of the slits showing that there are also virtual vortex cores hidden in the vacuum of the slits. The elastic deformation of the phase gives the phase gradient at the left and right parts of the junction, and the lines where the phase passes from π to $-\pi$ are related to the traces of the phase slip processes (see figures 6.11), which have been provided by the passages of vortices across the junction.

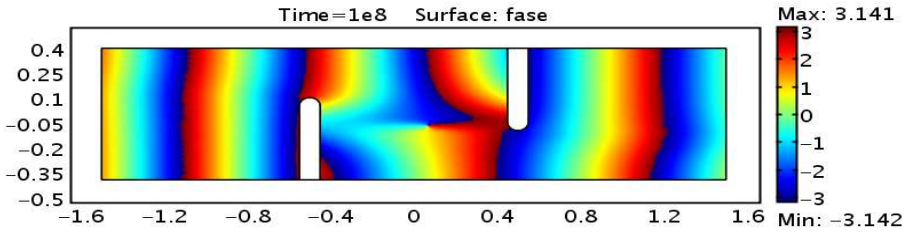

Figure 6.13: The phase of the complex order parameter in the final vortex state. The phase rotates by 2π going around the vortex cores and also around some virtual vortex centers hidden in the slits. In the color map, the phase passes from π in red to $-\pi$ in blue.

Distributions of the electric potential for the one-vortex stationary state is given in figure 6.14a. The total electric charge over the vortex core is zero, but the strong electric dipole moment is built-in, thus inducing the electric field which gives a sharp drop of the potential Φ around the vortex core. This should increase the tunneling probability of electron-hole pairs near the

core which can explain the peaks observed in experimental tunneling spectra. Figure 6.14 shows the distributions of the electric potential Φ (a), and even stronger variation is observed for the chemical potential ζ (b), hence for the normal concentration $n(\zeta)$. But for the electro-chemical potential μ, the sum of Φ and ζ, the variations almost compensate each other, so μ, hence the current, are insensitive to the presence of vortex which was not easy to predict. The cross-section plots of μ, ζ, and Φ passing through the vortex center is given in figure 6.15. It shows that both Φ and ζ have strong drops across the core and that both are non-monotonous. Moreover, the potential Φ has its sign inverted at the vortex center - that was not anticipated by analytic theories and in the static regime. The effect appear only if normal currents are allowed.

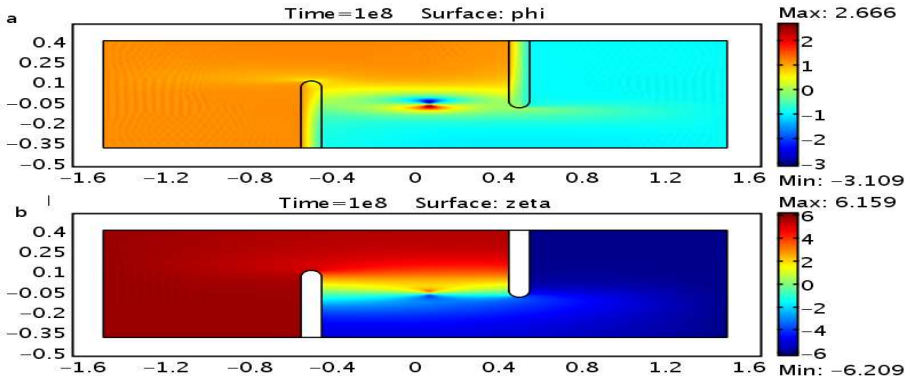

Figure 6.14: Distributions of the electric potential Φ (a) and of the chemical potential ζ (b) for the stationary one-vortex state. The sharp variations are confined around the vortex core. Notice the sign inversion of Φ across the core.

Even beyond the effects of vortices, it is instructive to compare the general pattern of the electric potential Φ in the reconstructed CDW state (figure 6.14 (a)) with the one prohibiting the CDW deformations (figure 6.10). For the second case we found that the density of normal carriers is unperturbed, $\zeta \equiv 0$ in the bulk, except for a charge variations $\sim 10\%$ concentrated along the boundaries in an invisibly narrow stripe, apparently of the order of the screening length $l_{scr} \approx 1.62nm$. The role of that boundary charge is to create the potential pattern of the figure 6.10 which drives the normal current. This

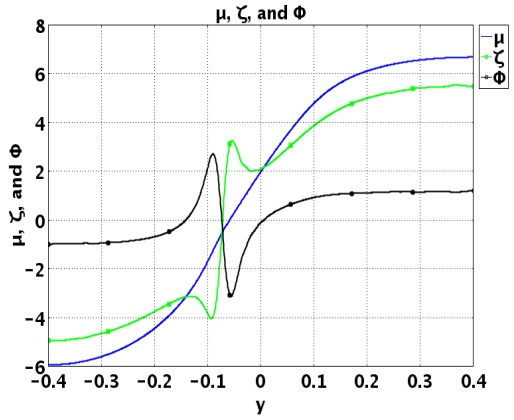

Figure 6.15: Cross-section plot of μ, ζ, Φ passing vertically through the vortex core. Notice the non-monotonous behavior of ζ and even inversion of Φ

is a regime totally dominated by the electric field. In the actual case of the allowed CDW deformations, the collective charge appears, which neutralizes, locally and almost exactly, the normal charges, thus allowing for variations of their concentration in the bulk. Figure 6.14 and figure 6.15 show that now both Φ and ζ contribute to μ, and moreover ζ dominates over Φ thus reversing a naive picture of a passive conductor. In this actual regime, the current is dominated by the diffusion driven by the chemical potential gradient. We can interpret creation of larger number of vortices and the phase slip processes taking place beyond the inner junction as the passage among the two regimes of normal currents dominated by either electric field or the diffusion.

The I-V characteristics of the junction in the range of V for appearance of the first vortex are shown in figure 6.16. The nonlinear conductivity is observed when the stationary vortex settles in the junction, and the peak in the differential conductivity dI/dV corresponds qualitatively to that in the experiment [18]. The current increase is rather small, and we are inclined to think that a much strong contribution comes from the tunneling in the vortex cores.

We have extended the range of studied V to values as high as Δ to cover the whole experimentally accessible interval. For the rectangular geometry the number of vortices does not increase above 5. For the real geometry with slits, the number of stationary vortices reaches 2, then at higher V new

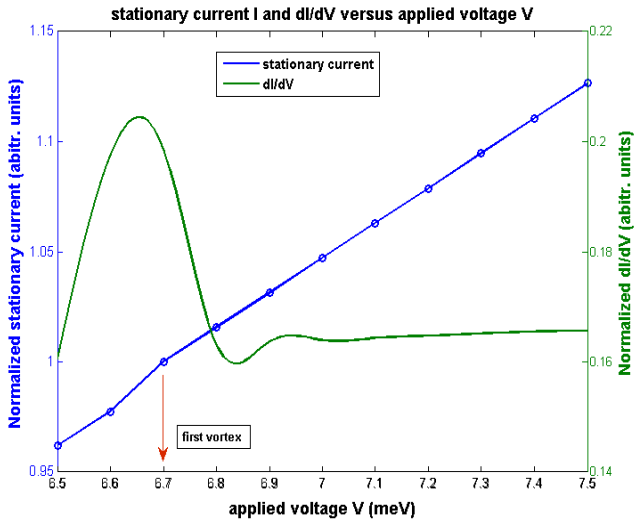

Figure 6.16: The current and the differential conductivity versus the applied voltage.

stationary vortices appear, but beyond the central junction area. We can guess that the experimental strong peak at $2V = 2\Delta$ does correspond to the tunneling creation of e-h pairs taking place within just a few vortex cores forming self-tuned atomic-size junctions.

6.4 Comparison of vortex states and the screening in CDWs and superconductors

There is a close historical relation between CDWs and superconductors (SC) in the development of the theories explaining their mechanisms and in the search of these materials. Here we discuss analogies and differences between vortices in the CDW and those in the SC.

For the SC, the vector potential $\vec{A}$ interacts with the complex order parameter $\Psi_{SC} = C\exp(i\theta)$, which phase deformations give the current $\vec{j} \propto C^2\nabla\theta$. For the CDW, the interaction is between the scalar potential Φ and the complex order parameter $\Psi_{CDW} = A\exp(i\varphi)$, which gives the charge density $\sim A^2\partial_x\varphi$. The energy functionals for these two cases can be

written schematically as

$$W_{SC} \propto \frac{C^2}{\lambda_{SC}^2}\left(\nabla\theta\right)^2 - \frac{2C^2}{\lambda_{SC}^2}\nabla\theta\vec{A} + \frac{C^2}{\lambda_{SC}^2}\vec{A}^2 + (\nabla \wedge \vec{A})^2, \tag{6.10}$$

$$W_{CDW} \propto A^2\left(\nabla\varphi\right)^2 + A^2\Phi\partial_x\varphi - \frac{1}{\lambda_{scr}^2}\Phi^2 - (\nabla\Phi)^2. \tag{6.11}$$

Here λ_{SC} is the penetration depth for the magnetic field $\vec{B}$ into the superconductor, and λ_{scr} - the screening length by normal carries, is the penetration depth for the electric field $\vec{E}$ when the CDW were not allowed to be deformed.

We see that the electric potential Φ in the CDW plays a role similar to the x-component A_x of the vector potential $\vec{A}$ in SCs. Hence the normal in-plain electric field $E_y = -\partial_y\Phi$ finds its counterpart in the normal magnetic filed $B_z = -\partial_y A_x$. So when these fields are given externally (thin films of the CDW in the condense or of the SC in the coil) then the two vortex states appear similarly.

But the reverse effects of the condensate and normal particles upon the fields are opposite. The diamagnetic term $\propto \vec{A}^2/\lambda_{SC}^2$ responsible for the screening of the magnetic field is the properties of the SC condensate, while the similar term $\propto \Phi^2/\lambda_{scr}^2$ in the ICDW has only an external origin, coming from the normal carries. The ICDW condensate screens the electric field only in the chain X direction while the transverse effect requires for the interchain decoupling. Moreover, these two terms enter with different signs to their energy functionals. Consequently, the normal electrons in the CDW versus the condensed electrons in the SC have inverse effects upon the applied field. In the SC, the applied magnetic field penetrates via the vortex cores being screened otherwise. In the ICDW without normal carriers, the applied transverse electric field is screened only within the vortex cores, otherwise the long range order of the CDW condensate prevents the bulk screening.

The ordered CDW state cannot screen the electric field while the superconductivity state cannot allow the magnetic field to pass through; the appearance of vortices breaks these two condensates respectively and gives back to the material their electronic and magnetic properties of metals, which are due to the free electrons.

6.5 Characteristic time scale for two processes

In this section, t_φ the characteristic time for φ to reach the stable state, is estimated from characteristic time t_A in the Ginsburg-Landau theory framework. From equation (6.6a), we have

$$\gamma \frac{1}{t_A} \frac{\partial A}{\partial \tau} \sim \frac{\Delta b}{\xi} \frac{A^2}{2} \ln\left(\frac{A^2}{e}\right). \tag{6.12}$$

We find that

$$t_A = \frac{\gamma \xi}{b\Delta}. \tag{6.13}$$

From equation (6.6b)

$$\gamma \frac{1}{t_\varphi} \frac{\partial \varphi}{\partial \tau} \sim \frac{\Delta \xi b}{4\pi L_{chara}^2} \frac{\partial^2 \varphi}{\partial^2 \tilde{x}}. \tag{6.14}$$

We find that

$$t_\varphi = \frac{4\pi L_{chara}^2 \gamma}{\Delta \xi b}, \tag{6.15}$$

L_{chara} is the characteristic length. Then we have

$$\frac{t_A}{t_\varphi} = \frac{\xi^2}{4\pi L_{chara}^2}. \tag{6.16}$$

$\xi = 8nm$ and Ł$_{chara}$ (characteristic length of phase variation) varies from several nm in the vortex core from $600nm$ outside the vortex core, and

$$\frac{t_A}{t_\varphi} \sim 10^{-5}. \tag{6.17}$$

From equation (6.13), the characteristic time $t_A \sim \left(\frac{\xi}{r_0}\right)^2 \frac{1}{\sigma_{CDW}} \sim 10^{-11}s$, and the characteristic time for φ, $t_\varphi \sim 10^{-5}s$.

6.6 Calculation of the screening length l_{scr}

In this section we calculate the screening length for parameter used in our computations.

By definition

$$\frac{1}{l^2} = \frac{4\pi e^2}{\varepsilon} \frac{dn_3}{d\zeta}|_{\zeta=0} = \frac{4\pi e^2}{\varepsilon} \frac{dn_2}{d\zeta} \frac{1}{d_z}|_{\zeta=0}, \tag{6.18}$$

where ζ is the chemical potential, n_3 is the 3D normal carrier density, n_2 the 2D normal carrier density, and d_z is the interplane distance. n_2 is calculated as the density of a 2D electron gas by summing the Fermi distribution. We have

$$\begin{aligned} n_2 &= \frac{2}{s}\sum_k \frac{1}{\exp(\frac{\varepsilon_k-\mu}{T})+1} = 2\int \frac{d^2k}{(2\pi)^2}\frac{1}{\exp(\frac{\epsilon_k-\mu}{T})+1} \\ &= \frac{m}{\pi\hbar^2}\int_0^{+\infty}\frac{d\varepsilon}{\exp(\frac{\varepsilon-\mu}{T})+1} \sim \frac{T}{\varepsilon_F}\log(1+\exp(\frac{\mu}{T})) \end{aligned} \tag{6.19}$$

In computation, we define $n_2 = n_0\frac{T}{\varepsilon_F}\ln\left(1+e^{\frac{\varepsilon_F+\zeta}{T}}\right)$, where n_0 is the 2D normal carrier density with $T\to 0$ and $\zeta = 0$, and it can be obtained from experimental data.

$$\frac{dn_2}{d\zeta} = \frac{n_0}{\varepsilon_F}\frac{1}{1+e^{-\frac{\varepsilon_F+\zeta}{T}}} \longrightarrow_{\zeta=0} \frac{n_0}{\varepsilon_F}\frac{1}{1+e^{-\frac{\varepsilon_F}{T}}}. \tag{6.20}$$

$$\frac{1}{l^2} = \frac{4\pi e^2}{\varepsilon}\frac{1}{d_z}\frac{n_0}{\varepsilon_F}\frac{1}{1+e^{-\frac{\varepsilon_F}{T}}}. \tag{6.21}$$

Then we have

$$\left(\frac{l_{scr}}{r_0}\right)^2 = \frac{2}{\pi}\frac{\varepsilon_F}{\hbar v_F d_y n_0}\left(1+e^{-\frac{\varepsilon_F}{T}}\right) = \frac{2}{\pi}\frac{\varepsilon_F}{\Delta\xi d_y n_0}\left(1+e^{-\frac{\varepsilon_F}{T}}\right). \tag{6.22}$$

With the numerical values in table 6.1 and $d_y = 1$, we find that $l_{scr}/r_0 = 2.7$, that's $l_{scr} \approx 1.62nm$. Here we recover an important feature of a 2D system that a small density of free carrier is able to induce a strong screening effect independent of concentration, resulting in a small screening length.

A strong screening of the Coulomb interactions will bring our theory, in a linear regime at least, more close to the classical elastic theory of [45].

6.7 Computational challenges

A proper choice of the initial condition is very important at the beginning of the simulation. In the calculations, we started with a linear interpolation of the voltage between the two boundaries, where the electric tensions are applied. For the rectangular geometry, this choice corresponds to the electric field distribution when there are no vortices formed in the sample.

Another difficulty in the simulation is related to the creation of the mesh. A typical size of the vortex is $50nm$, so the size of the mesh must be much smaller than this typical length. However, an increase of the density of the mesh will consume more memory in the computer (we worked with 8Gbites), and require a longer computation time when the program could crash. In the complicated slit geometry, an extremely fine mesh will be inefficient in the calculation, so we increase partially the mesh density to about $10nm$ at the center part in the slit geometry, for the stationary vortices will stay only at this region. The results obtain by this modification are satisfactory both in resolution and efficiency.

At the beginning of the work, we adopted a Ginzburg-Landan stationary approach in our studies, that is solving for the order parameter the extremal equation $\frac{\delta w}{\delta \varphi} = 0$. However, in this approach, we encounter the stability problem when the CDW vortex state appears. The results found by this method gives the extremal, but not necessary the minimum energy. The system gets confused among extremals corresponding to local minima, maxima, and saddle points in the configurational space. After many efforts, we moved to the dissipative Ginzburg-Landau approach to resolve the problem, with $\frac{\delta w}{\delta \varphi} = -\gamma_\varphi A^2 \frac{\partial \varphi}{\partial t}$. This method permits the dissipation of the total energy, and the solution is expected to relax to the minimum point of the energy configurations; that eliminates the primary instabilities in simulations.

Chapter 7

Extended Ginsburg-Landau theory for charge density waves

In this chapter we present the extended Ginsburg-Landau like theory for CDW which allows to incorporate the intrinsic carriers with their direct impacts upon the CDW. We first derive the equation of motion for the phase φ from the Lagrangian, which is obtained from the chiral transformation. Then we add the Poisson equation and adjust the diffusion equation for the normal carriers. Finally after we derive the equation for the amplitude A which now will be coupled with the one for the normal carriers. We shall clarify how this extended theory corresponds to the Ginsburg Landau theory in the linear regime. We shall present some results from the numerical studies of this system which are much more challenging to obtain.

7.1 Introduction

In previous chapters we introduced and worked within the Ginzburg-Landau like approach. This model is well established and works well for stationary states. But it allows to take into account explicitly only extrinsic ('ex') carriers which do not interact with CDW directly, only via the common electric potential. [1] The intrinsic carriers were supposed to be integrated out and inter to the model only via equilibrium value of the order parameter

[1] The nomenclature of extrinsic and intrinsic carries has been introduced in Ch.2

amplitude to which the relative amplitude A has been normalized. So, the CDW, together with its intrinsic carriers, was described by a single field $\Psi = A\exp(i\varphi)$. This way limits us quantitatively from considering the gapful charge density wave where the intrinsic carriers dominate while the extrinsic ones can be even absent. But more importantly, we are facing the qualitative problem of violating the conservation of the condensate charge - even in absence of the conversion(see section 2.7). In other words, having collective charge and current to be given by the phase derivatives with time-space dependent prefactor $A(t,x)^2$ violates the gauge invariance. At best, we could say that the definitions a perfect for constant A, stack to definition of n_c as in the previous study, and admit that we do not know what is the collective current, which we did not used before anyhow. But beyond the danger of leaving this knowledge gap, we will not be able to address the current conversion problem when the particles balance must be carefully monitored.

Now we shall build an extended scheme free from these problems and limitations. The derivation can be done without going to the heavy microscopics, thanks to exploiting the chiral invariance. Within this new model the intrinsic carriers are taken explicitly into account, while with some limitations:

- Intrinsic carriers are 1D

- Allowed for them: scattering by dominating CDW phonons - amplitudons and phasons, see Ch. 2, as well as by collisions among electrons trhemselves

- Forbidden: scattering in the frame of the host lattice (the Umklapp processes) and by impurities.

.

7.2 Lagrangian and phase equation

In order to obtain a detailed and theoretical description of the CDW system, we give a general microscopic derivation of the Lagrangian for the phase of the complex order parameter φ, following the concepts of [62, 63] traced back to [26].

Gauge and chiral invariance permit us to obtain the effective scalar potential V and the total longitudinal force F experienced by electrons under the CDW phase deformation and under an applied electric field $E_x = -\partial\Phi/\partial x$. Then, this potential is returned to the CDW thus affecting its properties.

First we show the transformation of the electron wave function and its components $\psi = (\psi_+, \psi_-)$ with respect to an arbitrary distortion of the phase $\varphi(x,t)$:

$$\begin{aligned} \psi &= \psi_+ \exp(ik_F x) + \psi_- \exp(-ik_F x) \\ \Rightarrow \tilde{\psi} &= \tilde{\psi}_+ \exp(ik_F x + i\frac{\varphi}{2}) + \tilde{\psi}_- \exp(-ik_F x - i\frac{\varphi}{2}). \end{aligned} \tag{7.1}$$

This is a chiral transformation [26] related to opposite changes in space and time of the phase of the wave function components (ψ_+, ψ_-). The Schrödinger equation operator transforms as follows:

$$H\psi \Rightarrow \tilde{H}\tilde{\psi}, \tag{7.2}$$

where

$$H = \begin{pmatrix} -i\hbar v_F \frac{\partial}{\partial x} + \Phi & \Delta e^{i\varphi} \\ \Delta e^{-i\varphi} & i\hbar v_F \frac{\partial}{\partial x} + \Phi \end{pmatrix}, \tag{7.3}$$

and

$$\tilde{H} = \begin{pmatrix} -i\hbar v_F \frac{\partial}{\partial x} + V & \Delta \\ \Delta & i\hbar v_F \frac{\partial}{\partial x} + V \end{pmatrix}. \tag{7.4}$$

From $\tilde{H}$ (7.4), it can be found that the chiral transformation gives the corresponding effective scale potential V and force experienced by the electrons F

$$V = \frac{\hbar v_F}{2}\frac{\partial\varphi}{\partial x} + \Phi, \tag{7.5}$$

$$F = -\frac{\partial V}{\partial x} = E_x - \frac{\hbar v_F}{2}\frac{\partial^2\varphi}{\partial x^2}. \tag{7.6}$$

The transformation (7.1) provides a quasi-classical solution of the Schrödinger equation at given external fields, if the phase φ is chosen from the equilibrium condition $F = 0$. In this respect, a convenience of the linearized spectrum creates an important physical paradox, which can be related to problems of so-called chiral anomalies (see [64] for discussion and references related to CDWs). Shortly, we see that only the phase of the wave function (7.1) is perturbed, while the amplitude can be considered to stay intact. This property contradicts to the requirement that at $\Delta = 0$ the total density of electrons deviates as $\delta\rho \sim \Phi$ while at $\Delta \neq 0$ we miss the Fröhlich effect $\delta\rho \sim \partial\varphi/\partial x$. It should be pointed out that for an arbitrary spectrum at $\Delta = 0$ the density distortion emerges from the next order quasi-classical correction as a factor ρ_E:

$$\varepsilon(p_\parallel) : vk \Rightarrow \varepsilon(p_F + k) - \varepsilon(p_F), \rho_E = |\Psi_E|^2 \sim \frac{\partial p}{\partial \varepsilon}|_{\varepsilon=\varepsilon(p)+\Phi}. \tag{7.7}$$

This factor is identically unity for the linearized spectrum approximation. Generally it provides a correction $\delta\rho_E \sim -\Phi/\varepsilon_F$ for any given state but gives a finite contribution to the integral density

$$\delta\rho = -N_F\Phi, N_F = 1/\pi\ \partial\varepsilon(p_F)/\partial p_F.$$

This finite contribution comes as an integral effect of all states far below the Fermi energy which makes it insensitive to the presence of the gap and/or the temperature. This feature is an important facility for our subsequent analysis.

The transformed Hamiltonian (7.4) corresponds to a 1D semiconductor with perturbations from phase derivatives akin to external electromagnetic field. Then the most traditional information can be used to describe the particles in the local frame. In this respect it is of special importance for our goals to distinguish between extrinsic and intrinsic carriers. The first ones are subjected to the field E solely while the later experience the combined force F. The electric responses of extrinsic ϵ_{ex} and intrinsic ϵ_{in} carriers with respect to E and F correspondingly are characterized completely by their partial dielectric functions ϵ_a where $a = ex, in$.

Now we are able to write down the Lagrangian $\mathcal{L} = \mathcal{L}(\varphi, \Phi)$. It can be done by combining arguments of the gauge and the chiral invariance which

have been expressed by (7.4) (7.5), (7.6).

$$-\mathcal{L}=\int d^3r\Bigg(-\frac{1+\epsilon_{ex}}{8\pi}(\nabla\Phi)^2-\frac{\epsilon_{in}}{8\pi}F^2+\frac{1}{\pi s}\left(\frac{\hbar v_F}{4}\left(\partial_x\varphi\right)^2+\Phi\partial_x\varphi\right)$$
$$+\frac{\hbar v_F A^2}{4\pi s}\left(\beta^2(\partial_y\varphi)^2-\frac{1}{u^2}\left(\partial_t\varphi\right)^2\right)\Bigg),\ A=A(T)=\frac{\Delta(T)}{\Delta(0)}. \quad (7.8)$$

The first term of the Lagrangian $\sim \epsilon_h = 1+\epsilon_{ex}$ is the host contribution for the electric field energy, which consists of a host part ~ 1 and of the extrinsic electrons contribution $\sim \epsilon_{ex}$.

The second term proportional to ϵ_i is the perturbative contribution from intrinsic electrons response to (7.6). It is calculated by the similar rules as the first term but the generalized force F from (7.6) is used instead of E_x. There are no other perturbation contributions from the Hamiltonian (7.4) in the lowest order.

The third term in 7.8 is a group of two sub-terms in brackets, which describes the missed contribution from the potentials (7.5). This energy comes from the states deeply below the Fermi surface, it is missed in the perturbation treatment with respect to F. Without perturbation with respect to (7.4), this term does not depend on temperature and even more it is not affected by the presence of the CDW [2]. For this reason it must coincide with the parent metal compressibility energy with respect to potentials of equation (7.5) where it is originated by (7.7). The physical meaning of this term is clear: the variation over the local distortion $1/\pi s\ \partial\varphi/\partial x$ gives the generalized force F of equation (7.6) and the equilibrium condition $F=0$ provides a correct metal response to external fields Φ.

Finally the fourth term is a group containing two sub-terms proportional to A^2 which appear due to an inter-chain CDW elasticity, and to the CDW lattice inertia.

The interference of the third non-perturbative term with the second perturbative one in (7.8) provides a correct renormalization $\propto (\partial\varphi/\partial x)^2$ of the CDW elastic energy at finite temperature so that it vanishes at $\Delta=0$ and in the normal state, as we shall see soon.

[2] A rigorous description of non-perturbation results for CDW in terms of so called "anomalies" is given in [64], but the perturbation part $\sim \epsilon_{in}$ was not treated properly.

The Lagrangian (7.8) should be interpreted as a function of two independent variables φ and Φ, and it is valid within the mean field approximation at all temperatures $T < T_{MF}$.

7.2.1 Equation of motion for the phase

The equation of motion for the phase should be derived by variation of the Lagrangian (7.8), i.e.

$$\frac{\delta \mathcal{L}}{\delta \varphi} = 0. \tag{7.9}$$

We find the following equation:

$$\left(1 - \epsilon_{in} r_0^2 \partial_x^2\right) \frac{\partial^2 \varphi}{\partial x^2} + \beta^2 \partial_y \left(A^2 \partial_y \varphi\right) + \frac{1}{\hbar v_F} \partial_x \Phi - \frac{\gamma_\varphi}{\pi \hbar v_F} A^2 \partial_t \varphi = 0, \tag{7.10}$$

where, in low frequency regime, the term $\sim (\partial^2\varphi/\partial t^2)$ gives place to the term $\sim \partial_t \varphi$ - the viscosity law, see section 2.9.

Following the common convention, we can define the coefficient $(1 - \epsilon_{in} r_0^2 q^2)$ before the term $\partial^2\varphi/\partial x^2$ as ρ_c - the CDW condensate density, similarly to the superfluid density in superfluids, also it is often referred to as a phase rigidity. Then

$$\rho_n = 1 - \rho_c = \epsilon_{in} r_0^2 q^2. \tag{7.11}$$

should be identified with the normal density ρ_n.

In the long wave, low frequency regime, ϵ_i is expected to be:

$$\epsilon_{in} = Re\epsilon_{in} + i4\pi \frac{\sigma_i}{\omega} \sim \epsilon_{in}^0 + min\left(\frac{1}{l_{in}^2 q^2}, -\frac{\omega_{in}^2}{\omega^2}, i\frac{4\pi\sigma_{in}}{\omega}\right), \tag{7.12}$$

where l_{in}, ω_{in}, and σ_{in} are the partial Debye screening length, the plasma frequency and the conductivity of intrinsic carrier. $l_{in}^{-2} = 4\pi e^2/s \ \partial n_{in}/\partial Z$, with n_{in} being the onchain concentration of intrinsic electrons and Z is their chemical potential. In the low frequency dissipative regime, equation (7.12) is given as

$$\epsilon_{in} = \epsilon_{in}^0 + \frac{1}{l_{in}^2 \left(q^2 - i\frac{\omega}{D}\right)}, \tag{7.13}$$

where D the diffusion coefficient is related to the conductivity as $D = 4\pi l_{in}^2 \sigma_{in}$.

At $T > T_{MF}$, in a total metallic state $\rho_n = 1$, $\rho_c = 0$. At very low temperature, the normal carriers freeze out, i.e. $\rho_n = 0$, $\rho_c = 1$. At vanishing frequency, the equation (7.13) is further simplified as $\epsilon_{in} = 1/(l_{in}^2 q^2)$, then with equation (7.11) we have the relation of ρ_n with the partial screening length

$$\rho_n = \frac{r_0^2}{l_{in}^2}. \tag{7.14}$$

7.3 Complete system of nonlinear equations

Now we shall use the outlined above principles to derive equations valid also in the necessary nonlinear (with respect to all variables) regime. We call that the extended Ginsburg-Landau theory.

We define the on-chain density of the energy $\sim (\partial_x \varphi)^2$ and of the charge $e\partial_x\varphi/\pi$ for the whole electronic system (i.e. preparing the locally deformed state of the parent metal before imposing the charge density wave). The intrinsic carriers, subjected to the field $\delta E_F = \partial_x \varphi v_F \hbar/2$, will effectively erase these density bringing them to level $\sim \rho_c \sim \Delta^2 \sim A^2$ in accordance with the Ginzburg-Landau approach, but in a well controlled and sometimes different way.

We start with the following form of the local energy functional justified in the section 7.2:

$$H = \int dr^3 \frac{1}{s} \Big\{ \frac{\hbar v_F}{4\pi} \left((\partial_x A)^2 + (\partial_x \varphi)^2 + \beta^2 (\partial_y A)^2 + \beta^2 A^2 (\partial_y \varphi)^2 \right) + \frac{e}{\pi} \Phi \partial_x \varphi$$
$$- \frac{\epsilon s}{8\pi} (\nabla \Phi)^2 + e\Phi(n_{ex} - n_{hst}) + (e\Phi + \frac{\hbar v_F}{2} \partial_x \varphi) n_{in} + \mathcal{F}(\Delta, n_{in}^e, n_{in}^h, n_{ex}) \Big\} \tag{7.15}$$

Here $\partial_i \varphi$, unlike $\partial\varphi/\partial i$ $(i = x, y)$, are the local derivatives, which are insensitive to 2π jumps in φ appearing in the presence of vortices. $\mathcal{F}(\Delta, n_{in}^e, n_{in}^h, n_{ex})$ is the free energy density of a homogeneous state. n_{in}^e and n_{in}^h are the concentrations per chain of intrinsic electron and hole respectively. $n_{in} = n_{in}^e - n_{in}^h$ is the imbalance of the normal intrinsic charge density.

The local balance of forces upon the phase reads

$$\vec{\nabla} \cdot \vec{T} = \mathcal{F}_{hst} \Rightarrow \frac{\gamma_\varphi}{\pi} \frac{\partial \varphi}{\partial t}, \tag{7.16}$$

where $\gamma_\varphi/\pi\ \partial\varphi/\partial t$ is the friction force $\mathcal{F}_{hst}$ from the host crystal, with

$$\gamma_\varphi = \frac{\Delta\xi}{4\pi s r_0^2}\frac{1}{\sigma_{CDW}}. \tag{7.17}$$

The local elastic force $\vec{\nabla}\cdot\vec{T}$ is the gradient of the stress $\vec{T} = 1/\pi\ \partial W/\partial\nabla\varphi$, which here is normalized to one electron, and W is energy density in equation (7.15):

$$T_x = \frac{\hbar v_F}{2}\frac{\partial\varphi}{\partial x} + \Phi + \frac{n_i\pi\hbar v_F}{2} = U \tag{7.18}$$

$$T_y = \beta^2\frac{\hbar v_F}{2}\frac{\partial\varphi}{\partial y} \tag{7.19}$$

Here as usual, the electron charge e is included to the electric potential Φ. The equation (7.16) is expanded as:

$$\frac{1}{2}\left(\frac{\partial^2\varphi}{\partial x^2} + \beta^2\frac{\partial}{\partial y}\left(A^2\frac{\partial\varphi}{\partial y}\right)\right) + \frac{1}{\hbar v_F}\frac{\partial\Phi}{\partial x} + \frac{\pi}{2}\frac{\partial n_{in}}{\partial x} = \frac{\gamma_\varphi A^2}{\pi\hbar v_F}\frac{\partial\varphi}{\partial t} \tag{7.20}$$

Next is the Poisson equation coming form $\delta W/\delta\Phi = 0$,

$$\frac{2}{\pi}\frac{r_0^2}{\hbar v_F}\triangle\Phi + \frac{1}{\pi}\frac{\partial\varphi}{\partial x} + (n_{in} + n_{ex}) = 0 \tag{7.21}$$

We shall concentrate only on intrinsic carriers n_{in}, $n = n_{in}^e - n_{in}^h$; the extrinsic ones n_{ex} can be easily added a posteriori just as they were considered in the earlier work (see chapter 6). Instead of n, we can use the local chemical potential Z related to n by the equation of state, which also defines dimensionless normal and collective particle densities ρ_n and ρ_c (see equations (7.11, 7.14)):

$$Z = \frac{dF}{dn}; \tag{7.22}$$

$$\rho_n = \frac{1}{N_F}\frac{dn}{dZ} = \left(N_F\frac{d^2F}{dn^2}\right)^{-1} = -N_F\frac{d^2\Omega}{dZ^2}; \tag{7.23}$$

$$\rho_c = 1 - \rho_n. \tag{7.24}$$

(We shall consider the material functions $\rho_{n,c}$, and later the conductivity σ to depend on either n or Z without changing the notations.) By definition, in the metallic phase $\rho_n = 1$ then $\rho_c = 0$, approaching from the CDW phase

as $\rho_c(\Delta, Z, T) \sim \Delta^2$. At a given temperature we define the non-perturbed ($Z = 0$) equilibrium values $\Delta_{eq}(T)$ and $\overline{\rho}_c(T) = \rho_c(\Delta_{eq}, Z = 0, T)$; then we can identify the amplitude A, normalized to 1 in equilibrium, as $A_\rho^2 = \rho_c/\overline{\rho}_c$. We shall better use another technically convenient $A = \Delta/\Delta_0$ which is not normalized to 1 in equilibrium if $T > 0$.

The diffusion equation for the normal carriers is

$$\nabla\hat{\sigma}\nabla(Z + \Phi + \frac{\hbar v_F}{2}\frac{\partial\varphi}{\partial x}) = \frac{\partial n}{\partial t} = \frac{2}{\pi\hbar v_F}\rho_n\frac{\partial Z}{\partial t} = \frac{1}{4\pi}\frac{\epsilon_{hst}}{r_0^2}\rho_n\frac{\partial Z}{\partial t}, \qquad (7.25)$$

where $\hat{\sigma} = (\sigma_x, \sigma_y)$ is the anisotropy conductivity. The conductivity σ will be measured in sec^{-1} according to the definition of the dielectric susceptibility $Im\epsilon = \frac{4\pi\sigma}{\omega}$. We can check that in the linear regime ($\rho_n = const$, and $\sigma_n = const$) the equation coincides with the one derived in chapter 6.

Equations (7.20, 7.21, 7.25) constitute the full system, beyond the eq. for the amplitude A which will be discussed below.

7.4 Possible simplifications of the nonlinear theory

Below we explore several particular limits of the above equation system. One aim is to give comparison with the theory in chapter 6, hence emphasizing the roles of ρ_c and ρ_n in relation to A. However, in computations, it is neither necessary nor convenient to work with ρ_n and ρ_c, a more natural choice is to use $n(Z)$ explicitly.

7.4.1 Infinite conductivity

Consider the limit of infinite conductivity $\hat{\sigma} \to \infty$ (for both components, which is not quite physical for the transverse one). Then roughly, characteristic length l and time t are such that $l^2/t \ll r_0^2\sigma$, hence $\partial_t n$ can be neglected and the equation (7.25) becomes:

$$\nabla\hat{\sigma}\nabla(Z + \Phi + \frac{\hbar v_F}{2}\frac{\partial\varphi}{\partial x}) \approx 0. \qquad (7.26)$$

This equation implies also that the electrochemical potential μ must be zero to compensate the divergence of the conductivity, that's

$$\mu \equiv Z + \Phi + \frac{\hbar v_F}{2}\frac{\partial \varphi}{\partial x} = 0. \tag{7.27}$$

This relation provides a good bridge to link the improved GL theory to the previous one. Equation (7.21) with the help of equation (7.27) can be written as

$$\frac{2}{\hbar v_F}(r_0^2 \nabla^2 E_x - \rho_n E_x) = \rho_c \partial_x^2 \varphi. \tag{7.28}$$

The right-hand side of this equation resembles indeed the definition of the effective charge as $n_c = A^2 \partial_x \varphi / \pi$, thus identifying ρ_c and A^2 but with an important correction in our nonlinear regime, when $\rho_n \neq cnst$ (it is a given function of $Z = -\Phi - \frac{\hbar v_F}{2}\partial_x \varphi$). Instead, we have for the charge derivative: $\partial_x n_c = A^2 \partial_x^2 \varphi / \pi$. Also there appears an earlier unaccounted term (which we have placed to the left-hand side). It corresponds simply to the screening of the electric field with a standard local screening length $l_i^2 = r_0^2/\rho_n$ (see equation 7.14). That is, we should assume the low T regime when this screening is negligible in comparison with the one from extrinsic carriers.

The equation (7.20) becomes analogously,

$$-\rho_c E_x + \hbar v_F \left(\frac{1}{2} \left(\rho_c \frac{\partial^2 \varphi}{\partial x^2} + \beta^2 \frac{\partial}{\partial y} \left(A^2 \frac{\partial \varphi}{\partial y} \right) \right) - \gamma_\varphi \frac{\partial \varphi}{\partial t} \right) = 0. \tag{7.29}$$

It looks similar to the equation in GL theory in chapter 6, but with an important corrections - no differentiation of the amplitude: $\rho_c \partial_x \Phi$ instead of $\partial_x (A^2 \Phi)$ and $\rho_c \partial_x^2 \varphi$ instead of $\partial_x (A^2 \partial_x \varphi)$. These changes are of principle importance because the problem becomes non-analytic in terms of the order parameter.

Local electroneutrality

The quite physical limit of local electroneutrality means that there is no local variation of the total charge; formally it is achieved by the limit $r_0 = 0$, but keeping $r_0^2 \sigma \sim D$ to be finite. In this case, the equation (7.21) becomes,

$$\partial_x \varphi + \pi n \equiv 0. \tag{7.30}$$

The equation (7.20) becomes,

$$\frac{\partial \Phi}{\partial x} + \frac{\hbar v_F}{2}\left(\beta^2 \frac{\partial}{\partial y}\left(A^2 \frac{\partial \varphi}{\partial y}\right) - 2\gamma_\varphi \frac{\partial \varphi}{\partial t}\right) = 0. \tag{7.31}$$

Notice that, surprisingly, there is no x rigidity for the phase anymore: the terms containing $\partial_x \varphi$ are canceled. The rigidity comes implicitly via E_x, which couples with $\partial_x \varphi$ in another equation.

The equation (7.25) becomes,

$$\nabla \hat{\sigma}(\nabla \Phi + \rho_c \nabla Z) = \frac{e^2}{s}\partial_t n = \frac{1}{4\pi}\frac{1}{r_0^2}\rho_n \partial_t Z. \tag{7.32}$$

We see that the driving field for the normal current is $-\nabla\Phi - \rho_c \nabla Z$, so that the diffusion is effectively reduced by a factor ρ_c.

7.4.2 Local electroneutrality together with the infinite conductivity

In the double limits of the local electroneutrality and the infinite conductivity, we obtain two simplified equations (7.30, 7.27),

$$\partial_x \varphi + \pi n = 0 \ , \ Z + \Phi + \frac{\hbar v_F}{2}\partial_x \varphi = 0,$$
$$\text{hence } -\Phi = Z - \frac{\pi \hbar v_F}{2} n \ , \ E_x = \rho_c \partial_x Z.$$

The equation (7.20) becomes

$$-\rho_c \partial_x Z + \hbar v_F \left(\frac{1}{2}\beta^2 \partial_y \left(A^2 \partial_y \varphi\right) - \gamma_\varphi \partial_t \varphi\right) = 0. \tag{7.33}$$

The driving force is $-\rho_c \partial_x Z$ and, similar to equation (7.31), there is no x rigidity for the phase. It comes indirectly from the complementary equation $\partial_x \varphi + \pi n = 0$. We can also revert the n dependence to $Z(n)$ to get

$$\hbar v_F \left(\frac{\rho_c}{\rho_n}\partial_x^2 \varphi + \beta^2 \partial_y \left(A^2 \partial_y \varphi\right) - 2\gamma_\varphi \partial_t \varphi\right) = 0. \tag{7.34}$$

Interestingly, this equation does not contain the driving force at all. It will come from the boundary conditions for Z, and from dependencies of ρ in the

actual case of the nonlinear system. The coefficient ρ_c/ρ_n, divergent at $\rho_n \to 0$, is known as the Coulomb hardening effect: with disappearing screening by normal carriers, the charged phase deformations become infinitely costly [65, 66].

7.5 1D example

The following simplest example in 1D will give more insight on how the scheme outlined in the last section does work. Now the equation (7.26) can be integrated to

$$\frac{\partial}{\partial x}\left(Z + \Phi + \frac{\hbar v_F}{2}\frac{\partial \varphi}{\partial x}\right) = -\frac{e^2}{\sigma} j, \tag{7.35}$$

where $j = j(t)$ can be the function of t only. The equation (7.20) then becomes

$$\rho_c \frac{\partial \Phi}{\partial x} + \hbar v_F \left(\frac{\rho_c}{2}\frac{\partial^2}{\partial x^2} - \gamma \frac{\partial}{\partial t}\right)\varphi = \rho_n \frac{e^2}{\sigma} j. \tag{7.36}$$

The equation (7.21) becomes, after differentiation over x,

$$r_0^2 \triangle \frac{\partial \Phi}{\partial x} - \rho_n \frac{\partial \Phi}{\partial x} = -\frac{\hbar v_F}{2}\rho_c \frac{\partial^2 \varphi}{\partial x^2} + \rho_n \frac{e^2}{\sigma} j. \tag{7.37}$$

We recognize here the structure of equations from the GL approach with $\rho_c \sim \Delta^2$ standing for A^2, and $\rho_n \to 1$. But there are important differences which we have already seen under approximations : ρ_c, unlike A^2, stays at the left from the operator ∂_x, that is not being differentiated. Within the basic GL scheme, the equation would look like

$$\frac{\partial}{\partial x}\left(\rho_c \frac{\partial \Phi}{\partial x}\right) + \hbar v_F \left(\frac{\partial}{\partial x}\left(\frac{\rho_c}{2}\frac{\partial}{\partial x}\right) - \gamma \frac{\partial}{\partial t}\right)\varphi = -\frac{e^2}{\sigma} j, \tag{7.38}$$

$$r_0^2 \triangle \frac{\partial \Phi}{\partial x} - 2\frac{\partial}{\partial x}(\rho_n \Phi) = -\frac{\hbar v_F}{2}\frac{\partial}{\partial x}\left(\rho_c \frac{\partial \varphi}{\partial x}\right) + \frac{e^2}{\sigma} j. \tag{7.39}$$

Unlike that form, now the gradient of the amplitude do not affect anymore the phase and the potential, and vice versa.

The total charge density is given as

$$\partial_x n_{tot} = \frac{1}{\pi}\rho_c \frac{\partial^2 \varphi}{\partial x^2} - \frac{2}{\pi \hbar v_F}\rho_n \frac{e^2}{\sigma} j \tag{7.40}$$

$$= \frac{1}{\pi}\rho_c \frac{\partial^2 \varphi}{\partial x^2} - \frac{2}{\pi \hbar v_F}\rho_n \frac{\partial \mu}{\partial x};\ \mu = Z + \Phi + \frac{\hbar v_F}{2}\frac{\partial \varphi}{\partial x} \tag{7.41}$$

which returns us to the additive definition $n_{tot} = n_c + n = \frac{1}{\pi}\frac{\partial\varphi}{\partial x} + n$. We see the difference with respect to the GL approach which would imply $n_c \sim \rho_c \frac{\partial\varphi}{\partial x}$, now ρ_c will appear implicitly only after compensations between $1/\pi\ \partial_x\varphi$ and n. There are no explicit expressions for the current, and it has to be restored from the conservation law or used generically as

$$J_{tot} = J_c + J_n = -\frac{1}{\pi}\frac{\partial\varphi}{\partial t} + J_n. \tag{7.42}$$

The collective current and the density following the phase deformation are given by the total number of electrons independent on the temperature and the magnitude of the gap.

This nonanalytic dependence on the amplitude of the order parameter requires for new more complicated numerical studies.

7.6 Back from the extended to the simplified models

As we have already mentioned in the beginning of this chapter, the Ginsburg-Landau model (see chapter 6) and presented in this section extended Ginsburg-Landau like model should converge for a linear system, and here we shall demonstrate it. The Ginsburg-Landau model takes into account only the extrinsic carriers, while the extended model deals also with the intrinsic carriers. These two models looks a bit different in this view, however, we are going to show that there are inherent relations between them. We shall derive the Ginsburg-Landau model from the extended model by taking some hypotheses.

To simplify notations, we consider the 1D case descried by the energy functional 7.15, then the energy density is

$$w = \frac{\hbar v_F}{4\pi}(\partial_x\varphi)^2 + \frac{1}{\pi}\Phi\partial_x\varphi + \left(\Phi + \frac{\hbar v_F}{2}\partial_x\varphi\right) n_{in} - \frac{\epsilon s}{8\pi}\left(\nabla\Phi\right)^2 + F(n_{in}). \tag{7.43}$$

We consider the linear approximation with respect to charge carriers. It means that electrons respond linearly $n_{in} \sim Z$, and the free energy $F(n_i)$ is proportional to the square of the intrinsic carriers density, $F(n_i) \propto n_i^2/\hbar v_F$.

This hypothesis is valid for the temperature close to the CDW transition temperature T_P. We have

$$w = \frac{\hbar v_F}{4\pi}(\partial_x\varphi)^2 + \frac{1}{\pi}\Phi\partial_x\varphi + \left(\Phi + \frac{\hbar v_F}{2}\partial_x\varphi\right) n_{in} - \frac{\epsilon s}{8\pi}\left(\nabla\Phi\right)^2 + \frac{n_{in}^2}{2\hbar v_F}. \quad (7.44)$$

We minimize the energy density w with respect to n_{in}:

$$\frac{\delta w}{\delta n_{in}} = 0 \Rightarrow n_{in} = -\frac{1}{\hbar v_F}\left(\Phi + \frac{\hbar v_F}{2}\partial_x\varphi\right). \quad (7.45)$$

Substituting n_i into (7.44), we obtain

$$w = \frac{\hbar v_F}{4\pi}\rho_c(\partial_x\varphi)^2 + \frac{1}{\pi}\Phi\rho_c\partial_x\varphi + \frac{1}{\hbar v_F}\Phi^2 - \frac{4r_0^2}{\hbar v_F}\left(\nabla\Phi\right)^2. \quad (7.46)$$

$\rho_c \sim A^2$ when it is small. We then recover the Ginsburg-Landau formalism from this extended model in the limit of linear regime.

7.7 Amplitude and thermodynamic potential

The amplitude $A \sim \Delta$ enters as a variable parameter via ρ_n, ρ_c, β, so we have already recovered, with corrections, the terms present in the GL equation as $A^2\partial_t\varphi$, $A^2\left(\partial_x\varphi\right)^2$, $A^2\left(\partial_y\varphi\right)^2$. We can add also the similar time derivative of A, and the gradient terms corresponding to the energy $\left(\frac{\partial A}{\partial x}\right)^2, \left(\frac{\partial A}{\partial y}\right)^2$ which coefficients now are not bound to the ones for the phase derivative as it was in the GL case.

Unlike the case of extrinsic carriers, now the equilibrium is shifted by perturbations of the intrinsic ones. So the free energy is not any more separable into A and n additive parts like it was: $\sim A^2\ln A + F(n)$. The property of the free energy $F(\Delta, n)$, or equivalently of the Gibbs energy $\Omega(\Delta, Z) = F(\Delta, n) - Zn$, is that its extremum Δ_{min}, given by $\partial\Omega/\partial\Delta = 0$, depends on n or Z in such a way that at $|Z| > Z_{eq} \sim \Delta_{eq} = \Delta(0,T), \Delta_{min} = 0$. So we can generalize the GL scheme by writing

$$\frac{\xi_0}{2\pi}\left(-\frac{\partial^2 A}{\partial x^2} - \beta^2\frac{\partial^2 A}{\partial y^2} + \beta^2\frac{dA^2}{dA}\left(\frac{\partial\varphi}{\partial y}\right)^2\right) + \frac{\partial\Omega}{\partial\Delta} = \frac{\gamma_A}{\Delta_0}\frac{\partial A}{\partial t} \quad (7.47)$$

The term $\sim A(\frac{\partial\varphi}{\partial x})^2$, complementary to the term $\sim A(\frac{\partial\varphi}{\partial y})^2$ in the above equation does not appear explicitly but it should come vie ρ_c being generated by $-\frac{\partial\Omega}{\partial\Delta}$ together with other equations. Physically and technically, the amplitude relaxes very fast, then we can neglect the time derivative in the equation i.e. $\gamma_A \to 0$, and the equation for A becomes instantaneous, like it is for Φ.

7.7.1 Prescription to calculate $\Omega(\Delta, Z, T)$

As an interpolation, we can be guided by a vague relation $\Delta_0^2 \approx \Delta_{min}^2 + Z^2 + T^2 \approx \Delta_{eq}^2 + T^2$, which can be implemented by writing the potential energy as

$$\Omega \sim -\Delta^2 \ln\left(\frac{e\Delta_0^2}{\Delta^2 + Z^2 + T^2}\right). \tag{7.48}$$

It follows that vanishing of Δ in the vortex center is related to the critical concentration; only the transverse phase gradient will contribute in analogy to the critical current in superconductors. This expression does not work well to describe the dependence on Z at a given Δ that is to give $n(Z)$. To precise the vague formula (7.48), we start with holes at $T = 0 : Z \le -\Delta, n = -n_h$, to be anti-symmetrized in the end as $n = n_e - n_h$, where $n_e(Z) = n_h(-Z)$.

We are going to obtain the following formula

$$\Omega(Z,\Delta) = \frac{1}{\pi\hbar v_F}\left(-|Z|\sqrt{Z^2-\Delta^2} + \Delta^2 \ln\left(\frac{\sqrt{Z^2-\Delta^2}+|Z|}{\sqrt{e}\Delta_0}\right)\right) \tag{7.49}$$

which gives us the functions necessary in simulation:

$$n = -\frac{\partial\Omega}{\partial Z} = \frac{sign(Z)}{\pi\hbar v_F}\sqrt{Z^2-\Delta^2} \tag{7.50}$$

$$\frac{\partial\Omega}{\partial\Delta} = \frac{\Delta}{\pi\hbar v_F}\ln\left(\frac{\sqrt{Z^2-\Delta^2}+|Z|}{\Delta_0}\right) \tag{7.51}$$

That is valid at $|Z| > \Delta$, otherwise, there are no normal particles and we are left with the old expression

$$\Omega(\Delta \le |Z|) = \frac{1}{2\pi\hbar v_F}\Delta^2 \ln\left(\frac{\Delta^2}{e\Delta_0^2}\right). \tag{7.52}$$

The equation (7.49) is obtained by integration $\int ndZ$ but can be calculated directly as the ground state energy in the Peierls model

$$\Omega(\Delta, Z) - \Omega(0,0) = \frac{\Delta^2}{g^2} - \sum_{-E_k<Z<-\Delta} E_k(\Delta) + \sum_{-E_k<0} E_k(0), \tag{7.53}$$

$$E_k(\Delta) = \sqrt{(\hbar v_F k)^2 + \Delta^2}; \sum_{E_k} = 2\int \frac{dk}{2\pi}, \tag{7.54}$$

where we have subtracted the most divergent energy of the parent metallic state; g is the electron-phonon coupling constant. The integrals are still logarithmically divergent at large k, so the cutoff at some E_F looks to be necessary, as usual in a BCS type theory. More intelligently, we can absorb this divergence into the definition of $\Delta_0 \sim E_F \exp(\frac{-1}{\lambda}$ (see section 2.4) by writing g^{-2} in (7.53) through the condition that at $Z = 0$ the potential has a minimum over Δ at $\Delta = \Delta_0$:

$$\frac{2}{g^2} = \sum_k \frac{1}{E_k(\Delta 0)}.$$

The resulting expression is convergent, if terms with the same k are kept together, giving rise to (7.49):

$$\Omega(\Delta, Z) - \Omega(0,0) = \sum_k \frac{\Delta^2/2}{E_k(\Delta_0)} - \sum_{-E_k<Z<-\Delta} E_k(\Delta) + \sum_{-E_k<0} E_k(0). \tag{7.55}$$

We definitely need to consider finite temperature, otherwise the normal carrier will appear only at high voltage $V > \Delta$. We can vaguely introduce the effect of both the threshold smearing and the suppression of Δ if we generalize (7.49) by substituting in two occasions $\sqrt{Z^2 - \Delta^2} \Rightarrow ((Z^2 - \Delta^2)^2 + T^4)^{1/4}$. But then we loose effects of the order of thermal activation probability $\sim \exp((|Z| - \Delta)/T)$ which dominates except for a proximity of T to T_c or of $|Z|$ to Δ. Ideally, we need to make numeric work to calculate realistic $\Omega(\Delta, Z, T)$ as function of Z and Δ at a given temperature T. Unfortunately, our programs were not be able to work with numerically designed functions of dependable variables, so we worked with analytic interpolations.

At finite T, we have to take into account both branches $\pm E_k$ whatever is the sign of Z:

$$\Omega(\Delta, Z, T) - \Omega(0,0,T) = \frac{\Delta^2}{g^2} - T\sum_{k,\mp} \ln\left(\frac{1 + \exp(\frac{Z \mp E_k(\Delta)}{T})}{1 + \exp(\frac{\mp E_k(0)}{T})}\right) \tag{7.56}$$

The function $\partial\Omega/\partial\Delta$ is plotted with respect to $\Delta(T)$ (figure 7.1), and its non-zero minimum is suppressed at the transition point. The renormalization procedure can be applied here as well.

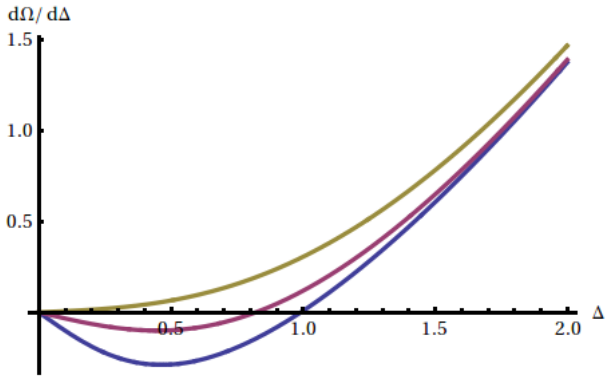

Figure 7.1: Function $\partial\Omega/\partial\Delta$ in $\Delta(T)$.

7.8 Results of modeling

Now we describe preliminary results obtained for the extended theory presented above. We shall give examples for the rectangular, and for the slits' geometries. All potentials and the temperature are measured in the units of Δ_0. Conductivities are measured in the units of the CDW conductivity.

7.8.1 Infinite conductivity, constant electrochemical potential μ

First, we consider results obtained in the approximation of infinite conductivities of normal carriers (with respect to the CDW conductivity). Parameters of the potential energy will be chosen such that the CDW amplitude vanishes when the chemical potential of electrons exceeds $\zeta^* = 0.25$. Extrinsic carriers were not taken into account. The figure below give the 3D plot of the amplitude at $T = 0.1$ with the voltage $V = 0.3$ applied in the interchain direction. Commonly, and in a short time, we observe a strong depression of A along the boundaries, see figure 7.2. The origin is clear: with normal electric field equals zero at the surface, the normal transverse current is driven by the y-

gradient of ζ- purely diffusive regime. With the applied $V > \zeta^*$ the carriers concentration exceeds the critical one at least in a narrow layers where A is suppressed. The interchain coupling still keeps it from vanishing until the following instability gives rise to a vortex nucleation, usually it happens near a corner as we see in the left panel, but a vortex or a pair of vortices can appear as well, as we see in the right panel. For the last case we have taken a strongly overestimated value of $r_0 = 20nm$; that reduces the strength of Coulomb interactions thus allowing for more variable patterns.

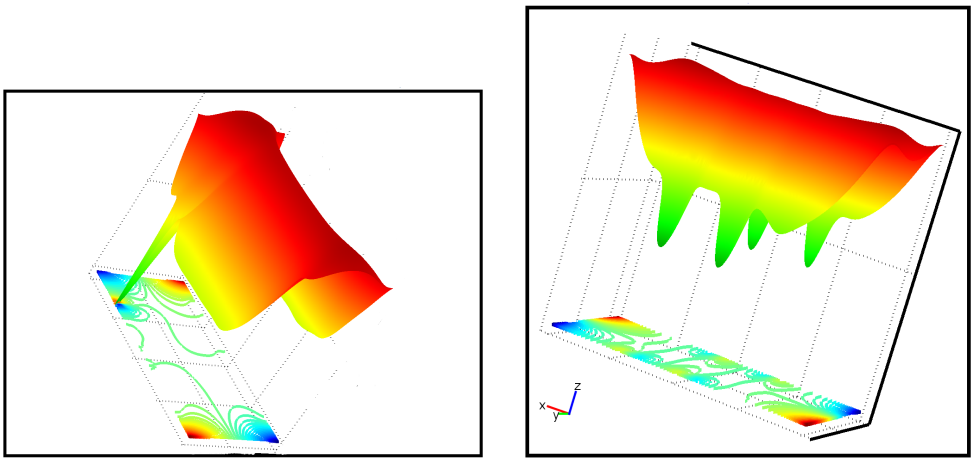

Figure 7.2: Amplitude of the order parameter and contour plot for the phase ($T = 0.1,\ V = 0.3$) for strong (left) and weak (right) Coulomb interactions.

Our modeling confirms that the rigidity of the order parameter amplitude A plays the crucial role. High rigidity does not allow anymore for a sharp drop near the boundary only, the deformation becomes distributed and a pronounced saddle appears in the middle; it splits in two when two pairs of vortices start to be formed. Only one of them becomes fully developed (left panel). We can further play with parameters to obtain the one dip crossing the whole cross section see figure 7.3, finally it gives rise to the vortex at one side of the dip.

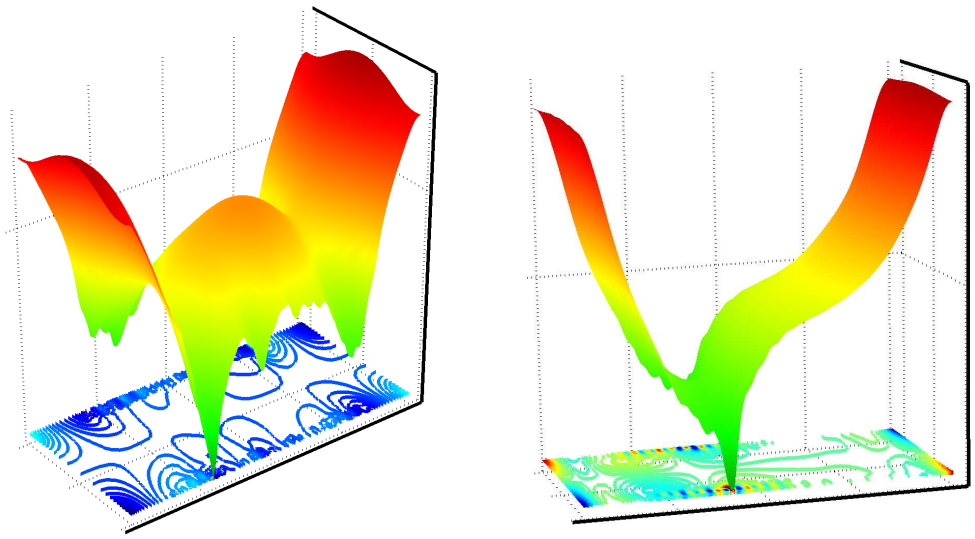

Figure 7.3: Amplitude of the order parameter and contour plot for the phase (T=0.1, V=0.4) for different rigidities of the order parameter amplitude.

7.8.2 General non-linear system of equations, rectangular geometry

When we abandon the approximation of the constant electrochemical potential (the limit of infinite conductivity) we face a strong shape effect. The vortices nucleate, and finally one of them fully develops, in sample's corners. See the figure 7.4 below; it was obtained at moderately enhanced $r_0 = 6$, enhanced relative transverse rigidity $\beta = 10$, and reduced overall rigidity $k = 0.01$.

While that may have a significance and actually take place, here we are interested in more universal features. Since we could not go to very long samples for computational reasons, we have just applied the conditions $A = 1$ at the short-side boundaries preserving there the nominal CDW amplitude. At the left panel, computed for a weaker interchain coupling $\beta = 1$ and smaller on-chain conductivity ($\sigma_x = 10, \sigma_y = 0.01$), and $V = 1.1$ we see the already known (from the approximate approach above) drop at the junctions, followed by nucleation of two vortices at one junction. The right panel of the figure 7.5 and the following figure show results computed for $\sigma_x = 100$, $\sigma_y = 0.01$ and $V = 1$. We see the deep valley across the sample with two vortices

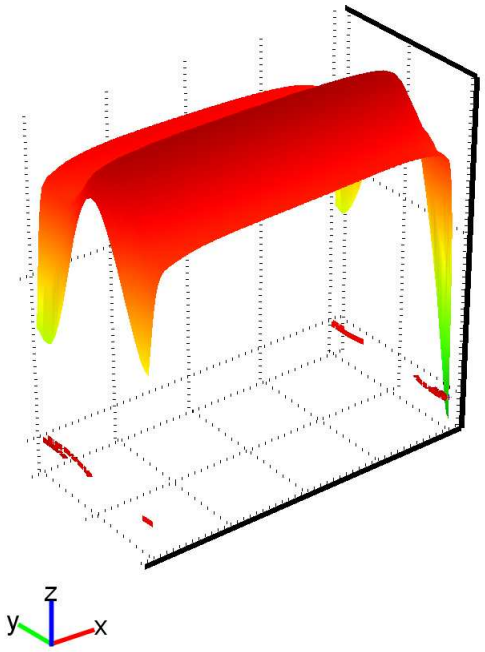

Figure 7.4: Amplitude of the order parameter ($T = 0.1,\ V = 0.5$).

forming at its edges i.e. at both junctions.

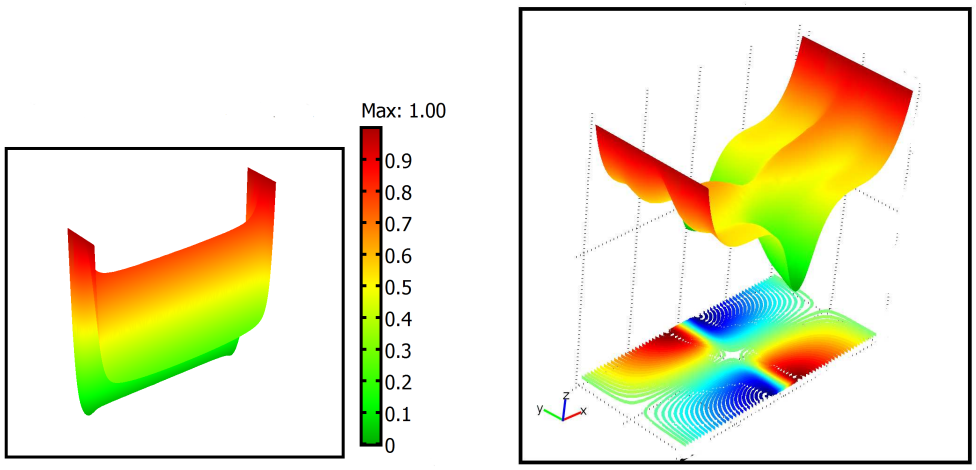

Figure 7.5: Order parameter amplitude (3D) and phase (2D) for the case of fixed nominal CDW amplitude at the short boundaries for two values of interchain coupling β and on-chain conductivity σ_x Left: $\beta = 1,\ \sigma_x = 10,\ \sigma_y = 0.01$. Right: $\beta = 3.3,\ \sigma_x = 100,\ \sigma_y = 0.01$.

The figure below, computed for parameters $\sigma_x = 10$, $\sigma_y = 0.01$, and $V = 1.1$ gives the 3D plot for ζ (left) and the contour plot for the phase (right) corresponding to the regime of the right panel of the Figure 7.5.

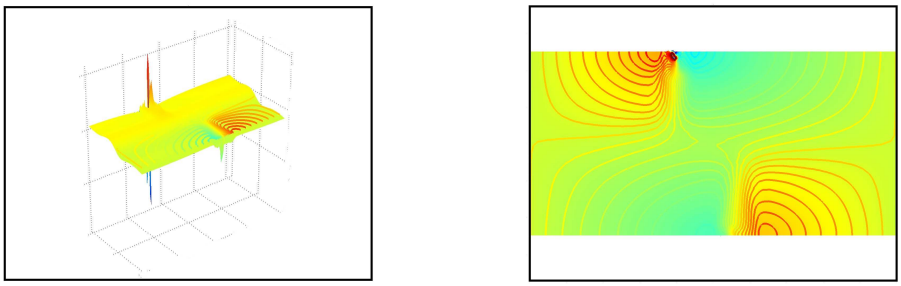

Figure 7.6: Chemical potential (left) and the phase (right). The parameters of modeling are the same as for figure 7.5.

Finally, below we compare the plots for the electric potential Φ and the full electrochemical potential μ. The electric potential shows kinks at the vortices, while μ, as always, is structureless

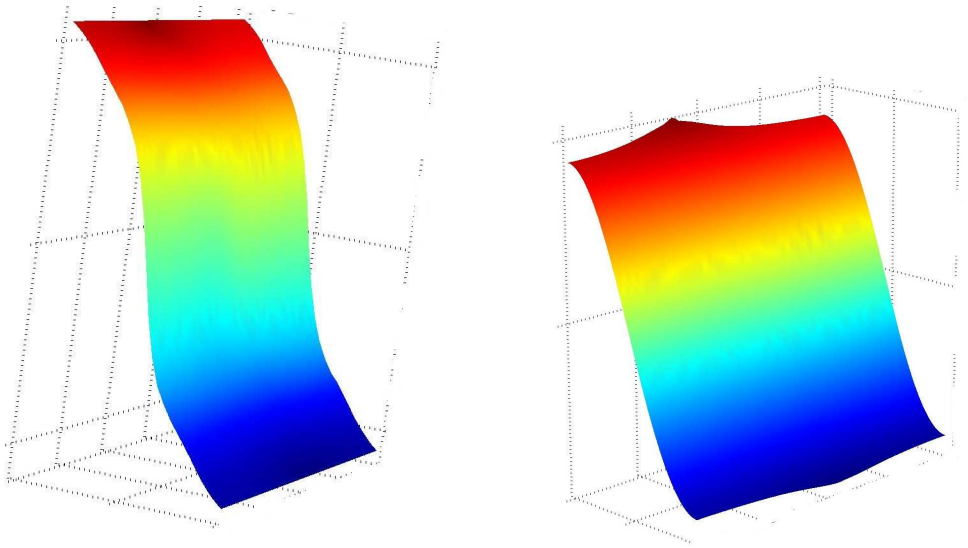

Figure 7.7: Full electrochemical potential μ (left) and electric potential Φ (right). The parameters of modeling are the same as for figure 7.6

7.8.3 General non-linear system of equations, slit geometry

As before, all potentials and temperature are measured in the units of Δ_0. Conductivities are measured in the units of the CDW conductivity. Unlike the plots above and in chapter 6, here the length scale is in microns, rather than in nano-meters.

First, we present results for parameters $T = 0.1$, $r_0 = 0.6mkm$, $\beta = 3.3, \sigma_x = 100$, $\sigma_y = 0.01$, $V = 0.4$. The very high value of r_0 has been chosen to artificially reduce the Coulomb energy. The plot (figure 7.8)below gives distributions of the order parameter amplitude A (left, colors change from read for $A = 1$ to blue for $A = 0$) and for ζ. We see the correlated rises of $|\zeta|$ and consequent drops of A which reason will be guessed and proved later on. First, there is a natural enhancement of carriers' concentration near the left and the right terminals. Second and interesting, there is also the enhancement at the slits in parts where the normal current arrives. Here the rise of all potentials contributes to termination of the normal current meeting the obstacle.

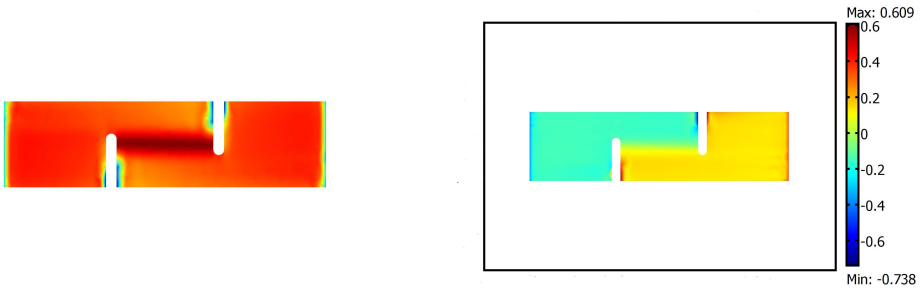

Figure 7.8: Amplitude (left) and electrochemical potential μ (right).

In the slit geometry the only variable which is determined in the whole plane (slits included) is the electric potential Φ. All others fields are valid only inside the sample. On the next figure 7.9 we present electrochemical potential μ and electric potential Φ. Notice that μ is presented only inside the sample, but Φ smoothly changes in the whole region of the sample and inside slits.

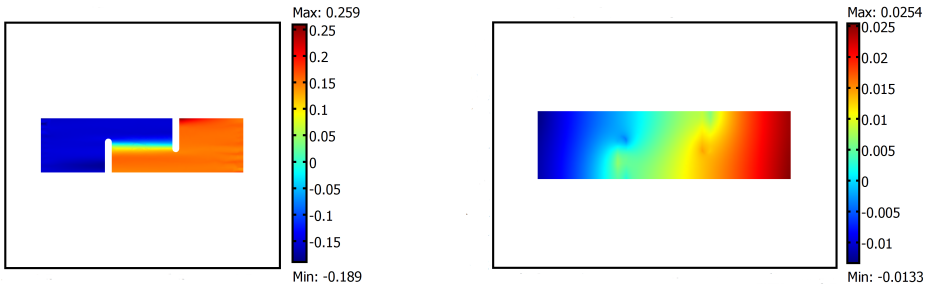

Figure 7.9: Electrochemical potential μ (left) and electric potential Φ (right).

Chapter 8

Current conversion and constraints in charge density waves.

In this chapter we study the conversion between the normal current and the condensate current in CDW, and find a system of equations to describe this process. We also explore the 1D limit and stationary current limit of this equations. We shall add very limited but already interesting results for these very demanding computations.

8.1 Introduction

In the previous chapters, we have studied formation of vortices, which motion might play a role in charge conversion between the CDW current and normal one. We have considered the interactions between various types of carriers: the condensate carriers n_c, intrinsic carriers n_i, extrinsic ones n_{ex}. However, we have not allowed for their mutual conversion, namely, the carriers interact but they are conserved separately. A very important process (see section 3.4) is the charge conversion when the carriers are exchanged among different reservoirs. This conversion is ultimately related to phase slips performed by propagation of topological defects. So these effects must be considered in ensemble. Below we shall outline equations, which may describe such effects.

Still, the complexity is beyond the reach of our facilities for detailed numerical modeling as in previous chapters for Ginsburg-Landay type models.

8.2 Method

In earlier chapters, we have seen the importance to work with the partial derivatives of the complex order parameter $\Psi = A\exp(i\varphi)$, for they make parts of the Hamiltonian and the equations of motion. Notice that their analytical properties are closely related to the topological configurations appearing in the CDW systems, such as dislocations, vortices, and phase slips.

We shall imply that all derivatives $\partial_i\varphi$ of the phase φ are local, they cannot be sensitive to artifacts of 2π jumps. So we should work with the invariant and differentiable form

$$\partial_i\varphi \Rightarrow \mathrm{Im}\,\frac{\partial_i\Psi}{\Psi} = \frac{1}{2i}\left(\frac{\partial_i\Psi}{\Psi} - \frac{\partial_i\Psi^*}{\Psi^*}\right) = \omega_i \ ; \ i = x, y, z, t. \tag{8.1}$$

A similar formula for the amplitude A is

$$2A\partial_i A = \partial(\Psi\Psi^*) = \Psi^*\partial_i\Psi + \Psi\partial_i\Psi^*. \tag{8.2}$$

The statics and dynamics of the CDW vortex system can be described by Vorticity, a measure of the vortex strength and the motion. The vorticity in space $I_{xy} = 2\pi\tau$ is the density of vortices with positions

$$\vec{r}_v(t) \quad \tau = \pm\delta(\vec{r} - \vec{r}_v)$$

.

The vorticity in space-time

$$I_{xt}, I_{yt}) = 2\pi\vec{I} = \hat{z} \times \vec{J} = (J_y, -J_x) = \vec{v} \times \vec{\tau}$$

is the vector orthogonal to the current of vortices $\vec{J}$, i.e. to their velocity $\vec{v}$ (see the section 3.1.2).

Usually vortices in superconductors or in superfluid can move in any direction with no difference. Contrarily, for edge dislocations there are two different types of motion: the glide and the climb, recall the section 3.1.2.

For an edge dislocation, the dislocation and the Burgers vector are perpendicular, so there is only one plane in which the dislocation can glide. The glide is the conservative motion - no inflow of adatoms or vacancies (electrons and holes in the CDW) is necessary. Another type of dislocations' motion, fundamentally different from glide, is known as the climb when the dislocation moves perpendicular to its glide plane. Unlike the glide, the climb is not conservative, because when the dislocation is passing e.g. in CDW across a chain, the phase increment along the chain changes by $\pm 2\pi$ i.e. one period is added/removed, hence two electrons have to be absorbed/emitted from/to the reservoir of normal carriers. The constraint for the climb gives

$$\frac{1}{\pi}\left(-\partial_x\omega_t + \partial_t\omega_x\right) = dn_c/dt = \mathcal{R} = -dn_n/dt \tag{8.3}$$

At this stage, we shall not exploit any form of the conversion function $\mathcal{R}$ (see the section 3.4.2) for that, but just take into account the balance of carriers $dn_c/dt + dn_n/dt = 0$.

At first, we shall consider only the intrinsic carriers (n is now the intrinsic carrier density by omitting the subscript "in"), while the extrinsic ones can be added *a posteriori*.

The full system of equations reads (see chapter 7):

$$\frac{2r_0^2}{\hbar v_F}\Delta\Phi + \omega_x + \pi n(z) = 0 \ , \ n = n_e - n_h, \tag{8.4}$$

where n_e is the density of electrons, and n_h the density of holes.

$$\partial_x\Phi + \frac{\pi}{2}\hbar v_F\partial_x n + \frac{\hbar v_F}{2}\left(\partial_x\omega_x + \beta^2\partial_y(A^2\omega_y)\right) = \gamma_\varphi A^2\omega_t \ , \ \gamma_\varphi = \frac{e^2}{\pi s\sigma_{cdw}} \tag{8.5}$$

$$-\partial\Omega/\partial A + a\partial_x^2 A + b\partial_y^2 A - cA\omega_y^2 = \gamma_A\partial_t A \tag{8.6}$$

where a, b, c are the known constant parameters.

$$0 = \frac{dn_n}{dt} + \frac{dn_c}{dt} = -\frac{s}{e^2}\nabla\hat{\sigma}\nabla(z + \Phi + \frac{\hbar v_F}{2}\omega_x) + \partial_t n + \frac{1}{\pi}\left(-\partial_x\omega_t + \partial_t\omega_x\right) \tag{8.7}$$

i.e.

$$-\nabla\left(\frac{\pi s}{e^2}\hat{\sigma}\nabla(z + \Phi + \frac{\hbar v_F}{2}\omega_x) + \hat{x}\omega_t\right) + \partial_t(\pi n + \omega_x) = 0 \tag{8.8}$$

The derivations of equation(8.4)- the Poisson equation, equation (8.5)- the equation for the phase φ, and equation (8.6)- the equation for the amplitude A, are the same as the equations (7.21, 7.20, 7.47) in chapter 7. The constraint (8.3) is integrated into the charge diffusion equation to obtain its form as equations (8.7, 8.8).

For a first step to study this system of differential equations, we shall consider the simple 1D case, and also some special limits, such as vanishing r_0 and high σ, similar to chapter 7.

8.3 1D case

8.3.1 General equations in 1D

We shall use the following abbreviations

$$q = \omega_x,\ \omega = \omega_t,\ E = E_x = -\partial_x \Phi,\ \gamma_\varphi = \frac{e^2}{\pi s \sigma_{cdw}},\ z = \zeta.$$

The equation (8.6) for amplitude A becomes

$$-\partial\Omega(A, z, T)/\partial A + a\partial_x^2 A = \gamma_A \partial_t A \tag{8.9}$$

Now this equation for A does not contain the phase gradient - no direct suppression of A - unlike in the 2D case. The effect upon A comes only indirectly through the chemical potential z in the expression of $\Omega(A, z, T)$.

The equation (8.5) for the phase, the Poisson equation (8.4), and the diffusion equation (8.8) are reduced as

$$-E + \frac{\hbar v_F}{2}\partial_x(q + \pi n) = \gamma_\varphi A^2 \omega, \tag{8.10}$$

$$q + \pi n = \frac{s}{4e^2}\partial_x E, \tag{8.11}$$

$$\partial_x\left(\frac{s}{e^2}\sigma_n\left(\partial_x(z + \frac{\hbar v_F}{2}q) - E\right) + \omega\right) = \partial_t(n + \frac{1}{\pi}q). \tag{8.12}$$

Using (8.11), we can exclude E from other equations, which is a unique feature of the 1D model. We obtain the following equations

$$(r_0^2\partial_x^2 - 1)(q + \pi n) = \frac{1}{4\pi}\frac{1}{\sigma_{cdw}}\partial_x(A^2\omega), \tag{8.13}$$

$$\partial_x \left(\frac{s}{e^2} \sigma_n \rho_c \partial_x z + \left(\frac{\sigma_n}{\sigma_{cdw}} A^2 + 1 \right) \frac{1}{\pi} \omega \right) = \partial_t (n + \frac{1}{\pi} q). \tag{8.14}$$

The extrinsic carriers can be added to the system as replacing the intrinsic carriers n in the Poisson equation by the sum of the two kinds of carriers $n_{ex}+n_{in}$. The densities of intrinsic $n_{ex}(\zeta)$ and extrinsic carriers $n_{in}(z)$ depend on their own chemical potential ζ and z, which are related by the relation

$$\zeta = z + \hbar v_F \partial_x \varphi / 2$$

assuming their fast mutual equilibration.

8.3.2 Local electroneutrality in 1D

Consider the vanishing r_0 - an approximation of the local electroneutrality $r_0 = 0$ in the Poisson equation while leaving it in the product $r_0^2 \sigma_n$- because always $\sigma \sim r_0^{-2}$ which factor just accommodates the electric charge e to transform the current of particles to the electric current. Then (8.11) gives

$$q + \pi n(z) = 0 \tag{8.15}$$

Then the eq. (8.10) becomes

$$E = \frac{-e^2}{\pi s \sigma_{cdw}} A^2 \omega = \frac{e A^2 I_c}{s \sigma_{cdw}} \tag{8.16}$$

where I_c is the condensate collective current per chain (it may depend on both x and t because of phase slips). The charge conservation equation becomes

$$-\partial_x \left(\frac{s}{e^2} \sigma_n \left(\partial_x (z - \frac{\pi}{2} \hbar v_F n) - E \right) + \frac{1}{\pi} \omega \right) = 0 \tag{8.17}$$

This equation gives us the unexpected expression of the normal current: the diffusion driving force is reduced by the factor ρ_c

$$\sigma_n \left(E - \rho_c \partial_x z \right) = I_n(t)$$

We have already seen these effects in section 7.4 We exclude E from the above two equations or adapt the general equation (8.14):

$$\frac{s}{e^2} \sigma_n \rho_c \partial_x z + \left(\frac{\sigma_n}{\sigma_{cdw}} A^2 + 1 \right) \frac{1}{\pi} \omega = -I(t) \tag{8.18}$$

Here I is the total current - our monitoring parameter, it may be t dependent but cannot depend on x. Equations (8.15, 8.18) supplemented by definitions of q and ω form the full system.

In the linear regime $\rho_c = cnst$, $\sigma_n = cnst$, we can exclude z via q to obtain the total current in terms of the phase alone:

$$I(t) = \frac{s}{e^2}\sigma_n \frac{1}{2}\hbar v_F \partial_x^2 \varphi \frac{\rho_c}{\rho_n} - \left(\frac{\sigma_n}{\sigma_{cdw}}A^2 + 1\right)\frac{1}{\pi}\partial_t \varphi \tag{8.19}$$

The first term describes the normal current driven by the gradient of the Fermi level $\frac{1}{2}\hbar v_F \partial_x \varphi$; it is amplified by the factor ρ_c/ρ_n, similar to the Coulomb hardening (see section 7.4). The second gives the drag $\sim A^2\sigma_n/\sigma_{cdw}$.

8.4 Preliminary results of modeling.

Here we present the preliminary results for the advanced scheme allowing for the current conversion. The conversion function $R(\eta)$ will be chosen linearized in the potentials' mismatch η: $R = const * (n_e^2 + n_h^2)\xi_0\eta$. We shall work with the following parameters: $T = 1$, $r_0 = 0.06mkm$, $\beta = 3.3, \sigma_x = 100$, $\sigma_y = 0.01$. Notice the enhanced T in comparison with previous studies. The choice of parameters was limited by necessity to perform calculations at quite refined mesh of 4000 points (for 6 fields) shown below, figure 8.1 left. Shown at the right panel, is the μ which is more structured now than usually. Particularly it is not monotonous along the paths between the terminals: the jump of μ across the bridge is 4 while only $V = 0.8$ was applied.

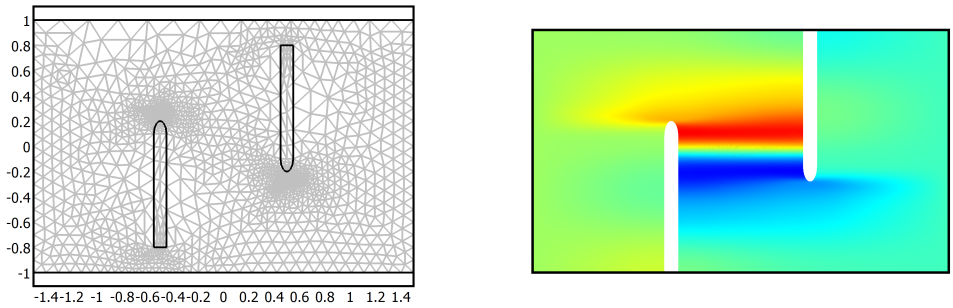

Figure 8.1: Slit geometry (left) and electrochemical potential μ (right).

Then we present the figures 8.2 showing an electric potential distribution

in the sample and the whole space. Still, the pattern of the electric potential are much richer as we see in the figure below.

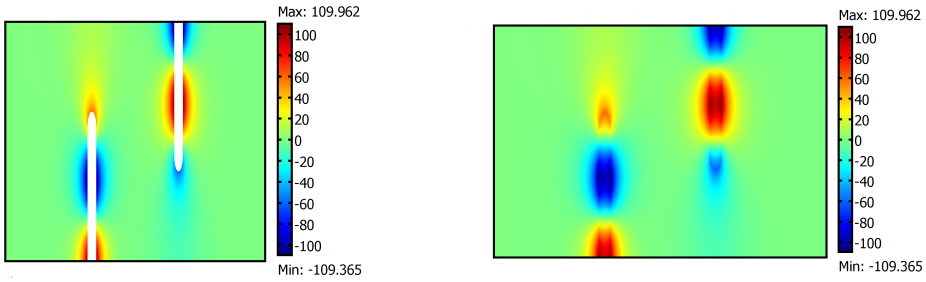

Figure 8.2: The distribution of the electric potential Φ in the sample (left) and in slits (right).

We observe three well separated types of spots with strongly enhanced magnitude of Φ but alternating signs. The one at foots of slits may be a geometric effect met already in the rectangular geometry. The one at the tips of the slits is not surprising even if needs to be understood. So, what is the origin of the ellipses at a middle of a slit, more or less at the level of the tip of another slit? The answer comes from the next figure 8.3 showing the color plot of the amplitude together with lines of the normal currents. We see that, the current leaving the terminal (only the left hand side is shown in full length) is not homogeneous over the cross section. Rather, it forms a high density narrow jet passing straight above the first tip before it hits the next slit. A strong potential has to be built here to terminate the current; one of its counterpart is the chemical potential ζ which directly, together with y-gradient of the phase, affect the amplitude A. We may say that the current jet burns down the CDW where it hits the obstacle. We should underline that the regime is not ballistic in our description (while it can be in very short samples). It is only a consequence of the very high, anisotropy of conductivities $\sigma_x/\sigma_y = 10^4$.

While the elongated spots of the amplitude suppression do not look sharp in the vortex core, actually they are. That is seen in the figure 8.4 below showing the color plot of the phase φ (normalized to π) together with the current lines. While the phase changes are tightly bound the slits boundaries, the phase increments are exactly 2π !

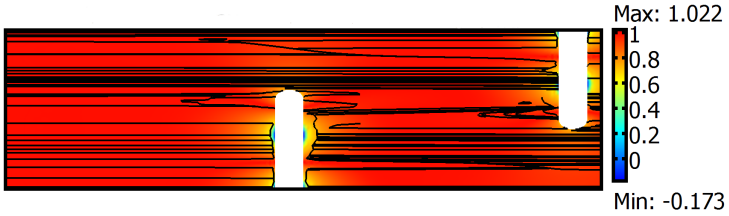

Figure 8.3: Amplitude of the order parameter A and the current lines.

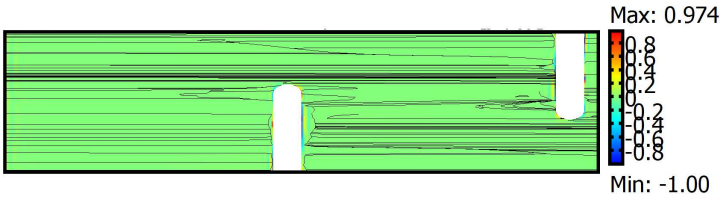

Figure 8.4: Phase φ of the order parameter and the current lines.

8.5 Conclusion

The derived equations can be the basic of a future work. We have presented the preliminary results of modeling taking into account the current conversion processes. But computation difficulties are multiplying, so a mainstream computer and a didacted programming may be required.

Chapter 9

Conclusion

Inhomogeneous and transient states of cooperative electronic systems with a spontaneous symmetry breaking attract a persistent attention: from a well known physics of vortices in superconductors to stripes in doped oxides, to recent local probes in electronic crystals, and to latest studies of transformations under impacts of a high electric field or pulses of light. The most common playground of modern studies are the Charge Density Waves (CDW) which are best accessible experimentally and best treated theoretically.

In this thesis, we have performed a program of modeling inhomogeneous stationary states, and their transient dynamic for the CDWs in restricted geometries under applied voltage and at passing normal currents. The aim was to see the reconstruction of the CDW state by proliferation of dislocation lines - the CDW vortices.

The models takes into account multiple fields in mutual nonlinear interactions: the two components of the CDW complex order parameter, and distributions of the electric potential, of the densities and the currents of two types of normal carriers.

The most detailed studies were based upon the dissipative Ginzburg-Landau type equation for the order parameter; it was augmented by equations for nonlinear diffusion of normal carriers and for the electric potential. The carriers were considered to be extrinsic with respect to the CDW: the two charged systems are coupled only by the common electric potential. This model describes, at low temperature, the class of CDWs preserving pieces of

ungaped Fermi surfaces.

Our studies allowed to compare different numerical techniques - from the earlier direct minimization for the static regime (no currents), to solution of differential equations describing the stationary regime with currents, and finally to the most informative dynamic simulations.

The obtained results elucidate experimental observations. We have confirmed the existence of the threshold voltages, above which the vortices are created inside the junction. We found that the number of vortices increases stepwise with the applied voltage. The simulations recover an important feature that the voltage drop concentrates at the vortex cores, which work as the self-tuned tunneling micro-junctions, and this phenomenon explains the experimentally observed peaks in the I-V plots.

The transient dynamics is very rich showing creation, annihilation and sweeping of multiple vortices. We distinguished the initial fast turbulent regime, followed by a transient regime when the remnant vortices are left and they slowly move to find their equilibrium positions.

Beyond that approach, it was necessary to describe the fully gapped CDWs by taking into account the intrinsic carriers which spectrum is affected by the CDW and which couple directly with the CDW deformations. Here, we have derived the extended model based on the property of the chiral invariance and taking into account the chiral anomaly. A further extension allowed to write equations taking into account the current conversion effect: exchange or electrons among the reservoirs of condensed and excited particles. The resulting equations are more complicated than what was assumed in the GL picture. They rely upon hidden cancellations and they are not analytic in the order parameter. As a consequence, the numerical process was very unstable and results are limited. Even if we were not able to reach the regime of the vortex propagation, we could see their nucleation at junctions or at obstacles. More sophisticated deducted programming and more powerful hardwire is necessary to continue this work which is our planning for the nearest future.

Our studies have shown their usefulness in the explaining of the experimental data, and they can give insights for the future experimental designs.

The results obtained from our modeling agree with experiment observa-

tions; they suggest more experimental verifications and designs. The methods can be extended to other types of charge organization known under the general name of the Electronic Crystal. It takes forms of Wigner crystals at hetero-junctions and in nano-wires, CDWs in chain compounds, spin density waves in organic conductors, and stripes in doped oxides. The studied reconstruction in junctions of the CDW may be relevant also to modern efforts of the field-effect transformations in strongly correlated materials with a spontaneous symmetry breaking.

Most of the described results have been published briefly in [67, 68]. The movies after the modeling are available at the web site [61].

Perspective

Up to now the process of vortex formation in CDW is not completely known. There is still much progress to be made for a better understanding of charge and current conversions between the condensate and the normal parts. Our attempts to solve these problem are good starting points. Still more efforts should be invested in these problems.

Our model can be extended to the studies of other geometrics and maybe a 3D model can be developed with the advance of the computing techniques.

Concerning the studies of Electronic Crystals, there are many topics, and every three years the ECRYS conference gives new discoveries in this field.

Appendix A

COMSOL multiphysics implementation

Here is the COMSOL Multiphysics program for the modeling. The complex order parameter $\Psi = A \exp i\varphi$ is split into its real part and image part $\Psi = u + iv$. The total free energy functional $H_{total} = H_{CDW} + H_{el}$ (equations 6.1,6.2) is written in u and v as,

$$\int \mathbf{d}^3 r \frac{\Delta_0 \xi_0}{4\pi s_\perp} \Bigg\{ \left(|\nabla u|^2 + |\nabla v|^2\right) + \frac{4\pi}{\xi_0^2} \left(\frac{u^2+v^2}{2} \ln \frac{u^2+v^2}{e} \right) + \frac{4}{\xi_0} \frac{\Phi}{\Delta_0} \left(uv' - vu'\right) + \frac{4\pi d_c}{\xi_0} \frac{\Phi}{\Delta_0} \left(n_2(\zeta) - \bar{n}_2\right) - 4 \left(\frac{r_0}{\xi_0}\right)^2 |\nabla \frac{\Phi}{\Delta_0}|^2 \Bigg\} + F(n) \tag{A.1}$$

Where

$$\xi_0 = \frac{\hbar v_F}{\Delta_0} \tag{A.2}$$

$$\frac{1}{r_0^2} = \frac{8e^2}{s_\perp \epsilon \hbar v_F} \tag{A.3}$$

$$n_2 = n_0 \frac{k_B T}{\varepsilon_F} \ln \left(1 + e^{\frac{\varepsilon_F + \zeta}{k_B T}}\right) \tag{A.4}$$

$$\varepsilon_F = \varepsilon(n_F) \tag{A.5}$$

Then from a variational calculation we obtain

$$-\triangle u+\frac{2\pi}{\xi_0^2}u\ln\left(u^2+v^2\right)+\frac{2}{\xi_0}\left(\frac{(\Phi v)'}{\Delta_0}+v'\frac{\Phi}{\Delta_0}\right)=-\frac{\gamma_\varphi v^2}{u^2+v^2}\frac{\partial u}{\partial t}+\frac{\gamma_\varphi uv}{u^2+v^2}\frac{\partial v}{\partial t}, \tag{A.6}$$

$$-\triangle v+\frac{2\pi}{\xi_0^2}v\ln\left(u^2+v^2\right)-\frac{2}{\xi_0}\left(\frac{(\Phi u)'}{\Delta_0}+u'\frac{\Phi}{\Delta_0}\right)=\frac{\gamma_\varphi uv}{u^2+v^2}\frac{\partial u}{\partial t}-\frac{\gamma_\varphi u^2}{u^2+v^2}\frac{\partial v}{\partial t}, \tag{A.7}$$

$$-2\left(\frac{r_0}{\xi_0}\right)^2\triangle\frac{\Phi}{\Delta_0}-\frac{1}{\xi_0}\left(uv'-vu'\right)=\frac{\pi d_c}{\xi_0}\left(n_2(\zeta)-\bar{n}_2\right), \tag{A.8}$$

$$\frac{n_0}{ef}\frac{1}{exp(-\frac{ef+\mu-\Phi}{T})+1}(\frac{\partial\mu}{\partial t}-\frac{\partial\Phi}{\partial t})-\nabla\left(\frac{n(\zeta)}{n_0}\hat{\sigma_0}\nabla\left(\mu\right)\right)=0. \tag{A.9}$$

The boundary conditions on all the sides of the sample are (von Neumann):

$$\left(\nabla u-\frac{2}{\xi_0}v\frac{\Phi}{\Delta_0}\vec{x}\right)\vec{n}=0, \tag{A.10}$$

$$\left(\nabla v+\frac{2}{\xi_0}u\frac{\Phi}{\Delta_0}\vec{x}\right)\vec{n}=0, \tag{A.11}$$

$$\left(\nabla\frac{\Phi}{\Delta_0}\right)\vec{n}=0, \tag{A.12}$$

$$\frac{n(\zeta)}{n_0}\hat{\sigma_0}\nabla\left(\mu\right)\vec{n}=0. \tag{A.13}$$

Except the boundaries where the voltage applied and the Dirichlet boundary condition is used:

$$\left(\nabla u\right)\vec{n}=0, \tag{A.14}$$

$$\left(\nabla v\right)\vec{n}=0, \tag{A.15}$$

$$\left(\nabla\frac{\Phi}{\Delta_0}\right)\vec{n}=0, \tag{A.16}$$

$$\mu=\pm V. \tag{A.17}$$

Initial conditions are

$$u=1,\quad v=0,\quad \mu=\Phi,\quad and\quad \Phi=V\frac{2y}{d}. \tag{A.18}$$

d is the length of the rectangle.

Appendix B

Publications

Works presented in my thesis are published:

- T. Yi, Y. Luo, A. Rojo Bravo and S. Brazovskii. Modelling of nonlinear and non-stationay multi-vortex behavior of CDWs at nonscales in restricted geometries of internal juncitons. *Physica B* 407: 1839-1844, 2012.

- T. Yi, Y. Luo, A. Rojo Bravo, N. Kirova, and S. Brazovskii. Reconstruction of the charge density wave state under applied electric field. *J. Supercond. Nov. Magn.*, 25:1323-1327, 2012.

My work was presented at the conferences

- Collaborative meeting: Charge density waves: small scales and ultrashort times (Vukovar, Croatia 2010)

  Title: Modeling of nonlinear and nonstationary behavior of CDWs at nano and meso scales of restricted geometries of mesa junctions.

- Hong Kong Forum of Physics 2010: Novel Quantum States and Methods (Hong Kong, China 2010)

  Title: Modeling of the ground state reconstruction by vortexes in nanojunctions of charge density waves.

- COMSOL Conference (Stuttgart, Germany 2011)

Title : Modeling of Nonlinear and Non-Stationary Multi-Vortex Behavior of Electronic Crystals in Restricted Geometries of Nano Junction.

- International research school and workshop on electronic crystals, ECRYS-2011 (Cargèse, France 2011)

  Title : Modeling of Nonlinear and Non-Stationary Multi-Vortex Behavior of Electronic Crystals in Restricted Geometries of Nano Junction.

- International Conference on Electronic States and Phases Induced by Electric or Optical Impacts, IMPACT-2012 (Orsay, France 2012)

  Title: Modeling of electronic vortices – the dislocations - in charge density waves under the electric field and near junctions

Bibliography

[1] in *International Research School and Workshop on Electronic Crystals ECRYS 2011*, Vol. 407, edited by S. Brazovskii, N. Kirova, and P. Monceau (Physica B, 2011).

[2] in *Proceedings of the International Workshops on Electronic Crystal-ECRYS 2008*, Vol. 404, edited by S. Brazovskii, N. Kirova, and P. Monceau (Physica B, 2008).

[3] R. E. Peierls, *Quantum theory of solids* (Oxford University Press, 1955).

[4] Electronic Properties of Inorganic Quasi-one-Dimensional Compounds, Physics and Chemistry of Materials with Low Dimensional Structures **1 2**, edited by P. Monceau (1985).

[5] G. Grüner, Rev. Mod. Phys. **60**, 1129 (1988).

[6] C. Schlenker, in *Low-Dimensional Electronic Properties of Molybdenum Bronzes and Oxydes*, edited by C. Schlenker (Kluwer Pub, Dordrecht, 1989).

[7] G. Grüner, Frontiers in Physics **89**, Reading, MA: Addison-Wesley (1994).

[8] C. J. Dumas, M. G. Schlenker, and S. V. Smaalen, Nato ASI Series B, Physics **354**, Plenum, New York (1996).

[9] W. A. Little, Phys. Rev. **134 (A6)**, A1461 (1964).

[10] P. Monçeau, N. P. Ong, A. M. Portis, A. Meerschaut, and J. Rouxel, Phys. Rev. Lett. **37**, 602 (1976).

[11] J. Bardeen, Phys. Rev. Lett. **42**, 1498 (1979).

[12] J. Bardeen, Phys. Rev. Lett. **45**, 1978 (1980).

[13] J. Bardeen, Phys. Rev. Lett. **55**, 1010 (1985).

[14] P. A. Lee, T. M. Rice, and P. W. Anderson, Phys. Rev. Lett. **31**, 462 (1973).

[15] R. E. Thorne, Physics Today **237**, 42 (May 1996).

[16] C. Brun, *Édue de Composés Quasi-unidimensionnels à Onde de Densité de Charge par Microscopie à Effet Tunnel*, Ph.D. thesis, Université PARIS-SUD 11 (2006).

[17] S. Brazovskii, C. Brun, Z.-Z. Wang, and P. Monceau, Phys. Rev. Lett. **108**, 096801 (2012).

[18] Y. I. Latyshev, P. Monceau, S. Brazovskii, A. P. Orlov, and T. Fournier, Phys. Rev. Lett. **96**, 116402 (2006).

[19] J. Solyom, Adv. Phys. **28**, 201 (1979).

[20] J. Voit, Rep. Prog. Phys. **58**, 977 (1995).

[21] S. Aubry and P. Quemerais, in *Low-Dimensional Electronic Properties of Molybdenum Bronzes and Oxydes*, edited by C. Schlenker (Kluwer Pub, Dordrecht, 1989).

[22] J. P. Pouget, S. Kagoshima, and C. J. Schlenker, J. Phys. Lett. (Paris) **44**, L113 (1983).

[23] J. Bardeen, L. N. Cooper, and J. R. Schrieffer, Phys. Rev. **108**, 1175 (1957).

[24] H. Fröhlich, Proc. Roy. Soc. Ser. A **233**, 296 (1954).

[25] P. A. Lee, T. M. Rice, and P. W. Anderson, Solid State Commun. **14**, 703 (1974).

[26] S. A. Brazovskii and I. E. Dzyaloshinskii, Sov, Phys, JETP **44**, 1233 (1976).

[27] H. Fukuyama, J. Phys. Soc. Jpn. **41**, 513 (1976).

[28] H. Fukuyama and P. A. Lee, Phys. Rev. B **17**, 535 (1978).

[29] N. P. Ong, J. W. Brill, J. C. Eckert, J. W. Savage, S. K. Khanna, and R. B. Somoano, Phys. Rev. Lett. **42**, 811 (1979).

[30] P. Monceau, Physica B **109**, 1890 (1982).

[31] F. Y. Nad and P. Monceau, Solid State Commun. **87**, 13 (1993).

[32] M. E. Itkis, F. Y. Nad, and P. Monceau, Journal of Physics: Condensed Matter **2**, 8327 (1900).

[33] A. Larkin, Sov. Phys. JETP **31**, 784 (1970).

[34] Y. Imry and S. keng Ma, Phys. Rev. Lett. **35**, 1399 (1975).

[35] L. J. Sham and B. R. Patton, Phys. Rev. B **13**, 2151 (1976).

[36] K. B. Efetov and A. I. Larkin, Sov, Phys. JETP **45**, 1236 (1977).

[37] T. Nattermann, Phys. Rev. Lett. **64**, 2454 (1990).

[38] S. E. Korshunov, Phys. Rev. B **48**, 3969 (1993).

[39] T. Giamarchi and P. L. Doussal, Phys. Rev. Lett. **72**, 1530 (1994).

[40] S. Brazovskii and T. Nattermann, Advances in Physics **53**, 177 (2004).

[41] P. A. Lee and T. M. Rice, Phys. Rev. B **19**, 3970 (1979).

[42] D. Feinberg and J. Friedel, J. Phys. France **49**, 485 (1988).

[43] J. Friedel, *Dislocations* (Pergamon Press, Oxford, 1964).

[44] L. Landau and E. Lifshitz, *Theory of Elasticity* (Mir, 1960).

[45] D. Feinberg and J. Friedel, *Imperfection of charge density waves in blue bronzes*, Low-dimensional electronic properties of molybdenum bronzes and oxides (Kluwer Academic Publishers, 1989).

[46] N. Kirova and S. Brazovskii, J. Phys. IV France **12**, 173 (November 2002).

[47] S. Brazovskii and S. Matveenko, Sov. Phys. JETP **72**, 492 (1991).

[48] S. Brazovskii and S. I. Matveenko, Sov. Phys. JETP **72**, 860 (May 1991).

[49] S. Brazovskii and S. I. Matveenko, Sov. Phys. JETP **74**, 864 (May 1992).

[50] M. Hayashi and H. Yoshioka, Phys. Rev. Lett. **77**, 3403 (1996).

[51] S. Brazovskii, N. Kirova, H. Requardt, F. Y. Nad, P. Monceau, R. Currat, J. E. Lorenzo, G. Grübel, and C. Vettier, Phys. Rev. B **61**, 10640 (2000).

[52] H. Requardt, F. Y. Nad, P. Monceau, R. Currat, J. E. Lorenzo, S. Brazovskii, N. Kirova, G. Grübel, and C. Vettier, Phys. Rev. Lett. **80**, 5631 (1998).

[53] D. Rideau, P. Monceau, R. Currat, H. Requardt, F. Nad, J. E. Lorenzo, S. Brazovskii, C. Detlefs, and G. Grübel, Europhys Lett. **56**, 289 (2001).

[54] S. Ramakrishna, M. P. Maher, V. Ambegaokar, and U. Eckern, Phys. Rev. Lett. **68**, 2066 (1992).

[55] K. Maki, Phys. Lett. A **202**, 313 (1995).

[56] N. P. Ong and K. Maki, Phys. Rev. B **32**, 6582 (1985).

[57] L. P. Gor'kov, JETP Lett. **38**, 87 (1983).

[58] Y. I. Latyshev, P. Monceau, S. Brazovskii, A. P. Orlov, and T. Fournier, Phys. Rev. Lett. **95**, 266402 (2005).

[59] S. G. Zybtsev, V. Y. Pokrovskii, and S. V. Zaitsev-Zotov, Nature Communications **1**, 85 (2010).

[60] N. Kirova, A. R. Bravo, and S. Brazovskii, Physica B : Condensed Matter **404**, 565 (2009).

[61] http://lptms.u-psud.fr/membres/brazov/Slit1.mpg, and http://lptms.u-psud.fr/membres/brazov/Slit2.mpg.

[62] S. Brazovskii, J. Phys. IV **3**, 267 (1993).

[63] S. Brazovskii, J. Phys. I **3**, 2417 (1993).

[64] I. Krive, A. Rozhavsky, and I. Kulik, Sov. Phys. JETP **12**, 635 (1986).

[65] B. Hennion, J. P. Pouget, and M. Sato, Phys. Rev. Lett. **68**, 2374 (1992).

[66] B. Hennion, J. P. Pouget, and M. Sato, Phys. Rev. Lett. **69**, 3266 (1992).

[67] T. Yi, Y. Luo, A. Rojo-Bravo, and S. Brazovskii, Physica B **407**, 1839 (2012).

[68] T. Yi, Y. Luo, A. Rojo-Bravo, N. Kirova, and S. Brazovskii, J. Supercond. Nov. Magn. **25**, 1323 (2012).